**From the holdings of the Department of Special Collections , Princeton University Library, Princeton, NJ**

These documents are either in the public domain, or can only be used for educational and research purposes (Fair use) as per U.S. Copyright law (text below). By accessing this file, all users agree that their use falls in the public domain or within fair use as defined by the copyrightlaw. We do not charge any permission or usage fees for the publication of images of material inour collections, including those provided by Princeton University Library, via our website, catalog, or directly from staff.For more information regarding copyright, credit, and citation please review the information onthe Copyright, Credit and Citation Guidelines page of our website.
https://library.princeton.edu/special-collections/policies/copyright-credit-and-citation-guidelines. If you have any questions, including how to order higher-quality images from the collection, contact Special Collections Public Services via our Ask Us! Form. https://library.princeton.edu/special-collections/ask-us

---

Doctoral Dissertations, 2011-2026 Astrophysical Sciences

2013

# Radiative and Mechanical AGN Feedback in Galaxy Evolution

Choi, Ena

Princeton, NJ : Princeton University

---

http://arks.princeton.edu/ark:/88435/dsp01h415p9671

*U.S. Copyright law: The copyright law of the United States (Title 17, §108, United States Code) governs the making of photocopies or other reproductions of copyrighted material. Under certain conditions specified in the law, libraries and archives are authorized to furnish a photocopy or other reproduction. One of these specified conditions is that the photocopy or reproduction is not to be used for any purpose other than private study, scholarship, or research. If a user makes a request for, or later uses, a photocopy or reproduction for purposes in excess of fair use that user may be liable for copyright infringement. This institution reserves the right to refuse to accept a copying order if, in its judgment, fulfillment of the order would involve a violation of copyright law. https://www.copyright.gov/title17/title17.pdf*

# Radiative and Mechanical AGN Feedback in Galaxy Evolution

Ena Choi

A Dissertation
Presented to the Faculty
of Princeton University
in Candidacy for the Degree
of Doctor of Philosophy

Recommended for Acceptance
by the Department of
Astrophysical Sciences

Adviser: Jeremiah P. Ostriker

November 2013

© Copyright by Ena Choi, 2013.

All rights reserved.

I certify that I have read this thesis and that in my opinion it is fully adequate, in scope and in quality, as a dissertation for the degree of Doctor of Philosophy.

Jeremiah P. Ostriker
(Adviser)

I certify that I have read this thesis and that in my opinion it is fully adequate, in scope and in quality, as a dissertation for the degree of Doctor of Philosophy.

Michael A. Strauss

I certify that I have read this thesis and that in my opinion it is fully adequate, in scope and in quality, as a dissertation for the degree of Doctor of Philosophy.

Renyue Cen

Approved for the Princeton University Graduate School:

Dean of the Graduate School

*For my family*

# Abstract

Accreting black holes are thought to inject energy into surrounding gas reservoirs via jets, outflows and radiation, inhibiting the build-up of massive galaxies and suppressing star formation. Active Galactic Nuclei (AGN) feedback can potentially starve the black hole, giving rise to a relation between the black hole mass and the stellar mass of galaxies. Many previous AGN feedback models, however, do not include all known and observed feedback processes. Since the importance of AGN-driven mass and momentum outflows in limiting the infall onto the black hole has been emphasized, we develop a numerical algorithm of AGN mechanical feedback via broad absorption line winds in a three-dimensional smoothed particle hydrodynamics code, modified with a pressure-entropy formulation, that better allows for contact discontinuities and implements improved fluid mixing. We also include the detailed treatment of radiative heating, radiation pressure, and the Eddington force and propose a unified model of AGN feedback. We investigate feedback effects in simulations of a single disk galaxy, major and minor mergers of galaxies, and the formation of elliptical galaxies in a cosmological context. We show that massive, non-relativistic outflows and X-ray heating are indeed a viable mechanism to regulate the black hole growth. While the thermal feedback model, where all the feedback energy is distributed as thermal heating, produces a factor of $\sim 10^2 - 10^3$ higher X-ray luminosity than expected for given stellar mass of the galaxy, our model can successfully reproduce both the observed $L_{\rm X} - \sigma_*$ and $M_{\rm BH} - \sigma_*$ relations. In our model, the AGN-induced outbursts result in strong galactic outflows with $v_{\rm w} \sim 2,000$ km/s consistent with observed quasar properties. They also effectively quench star formation making ellipticals red and dead consistent with the observations. Our model shows large fluctuations in both radiant and wind outputs, naturally reproducing the two modes of AGN feedback: 'wind' mode, where black holes grow rapidly near the Eddington limit and expel

gas via high velocity winds and powerful radiation pressure; and a 'maintenance' mode when the electromagnetic luminosity is considerably below the Eddington limit.

# Preface

This thesis consists of four chapters, each of which is based on a paper that has been published in a refereed journal, is in the process of being published, or will be submitted. Below, I list the papers and describe my contributions to each work.

1. *Momentum Driving: Which Physical Processes Dominate Active Galactic Nucleus Feedback?*

   Jeremiah P Ostriker, Ena Choi, Luca Ciotti, Gregory S Novak, and Daniel Proga

   The Astrophysical Journal, 722(1), 642. doi:10.1088/0004-637X/722/1/642

   In this chapter, I performed one-dimensional simulations and found that the growth of the black hole is very sensitive to the inclusion of the mass and momentum driving but is insensitive to the assumed mechanical efficiency. This work was completed under the guidance of my advisor, Jeremiah P. Ostriker. The section on the two-dimensional simulations done by Gregory S Novak published in the Astrophysical Journal is not included in this thesis. I prepared the manuscript for publications and wrote Section 2 and 3. Jeremiah P. Ostriker wrote Section 1 and 4.

2. *Radiative and Momentum-based Mechanical Active Galactic Nucleus Feedback in a Three-Dimensional Galaxy Evolution Code*

   Ena Choi, Jeremiah P Ostriker, Thorsten Naab, and Peter H Johansson

   The Astrophysical Journal, 754(2), 125. doi:10.1088/0004-637X/754/2/125

   Motivated by the work done in Chapter 1, I added new implementations of the momentum mechanical feedback, and restriction of accreted elements to those that are gravitationally bound to the black hole in three-dimensional smoothed particle hydrodynamic (SPH) simulation code. I also included the feedback from the X-ray radiation emitted by the black

hole, and test the new feedback model by analyzing outputs from isolated galaxy simulations. Again, this work was completed under the guidance of my adviser. I prepared the manuscript for publication.

3. *Consequences of Radiative and Mechanical Feedback from Black Holes in Galaxy Mergers*

   Ena Choi, Thorsten Naab, Jeremiah P Ostriker, Peter H Johansson, and Benjamin P Moster

   The Monthly Notices of the Royal Astronomical Society, submitted. (ArXiv identifier arXiv:1308.3719C)

   In this chapter, I used our new model with radiative and mechanical AGN feedback and restriction of accreted gas from Chapter 2 to study the effects of AGN feedback on merging galaxies. I prepared the manuscript for publication.

4. *The Impact of Mechanical AGN feedback on the Formation of Massive Early-type Galaxies*

   Ena Choi, Jeremiah P Ostriker, Thorsten Naab, Ludwig Oser, and Benjamin Moster

   To be submitted to the Astrophysical Journal.

   Here, I analyzed outputs from hydrodynamical simulations of the formation of elliptical galaxies in a cosmological context using a zoom-in approach. I am currently preparing the manuscript for submission to ApJ. While all of the parts of the code related to AGN feedback were my work, the improvements to the code implemented in this latest version of SPH simulation code were added by Benjamin Moster.

# Contents

**Abstract** **iii**

**Abstract** **v**

**Preface** **vi**

**1 The Importance of AGN-driven Mass and Momentum Outflows** **1**

1 Introduction . . . . . 1

2 Models . . . . . 6

3 Exploring one-dimensional models . . . . . 7

3.1 High efficiency models . . . . . 9

3.2 Low efficiency models . . . . . 9

3.3 Wind efficiency dependence of bottom-layer models . . . . . 13

4 Discussion . . . . . 13

Bibliography . . . . . 16

**2 AGN Feedback in isolated disk galaxies** **18**

1 Introduction . . . . . 18

2 Models . . . . . 21

2.1 Numerical code . . . . . 21

2.2 Black hole feedback model . . . . . 21

2.3 New black hole accretion model . . . . . 27

2.4 Initial condition . . . . . 30

3 Results . . . . . 31

3.1 Comparison of the different feedback mechanisms . . . . . 31

3.2 Galaxy merger simulation . . . 39
3.3 Soft bondi criterion . . . 41
3.4 Fiducial model and the effects of other physics . . . 41
4 Summary . . . 41
Bibliography . . . 45

**3 AGN Feedback in Galaxy Mergers** **49**
1 Introduction . . . 49
2 Model . . . 51
2.1 Numerical code . . . 51
2.2 Initial conditions and galaxy parameters . . . 52
2.3 The traditional thermal black hole feedback model . . . 53
2.4 The new mechanical black hole feedback model . . . 53
3 Comparison of Thermal and Mechanical Feedback models . . . 55
3.1 Black hole growth and star formation rate . . . 56
3.2 Properties of the post merger gas outflow . . . 61
4 Properties of merged galaxies . . . 64
4.1 Distribution of gas during the merger . . . 64
4.2 X-ray properties . . . 65
4.3 Galaxy-black hole Scaling relation . . . 65
4.4 Galaxy Size . . . 68
4.5 Central density . . . 72
5 Discussions and Summary . . . 72
Bibliography . . . 75

**4 AGN Feedback in the Formation of Early-type Galaxies** **80**
1 Introduction . . . 80
2 Simulations . . . 82
2.1 Numerical code . . . 82

2.2 Simulation setup . . . . . 82
2.3 Black hole formation and growth . . . . . 83
2.4 Radiative and mechanical black hole feedback . . . . . 84
3 Cosmological simulations of AGN feedback in individual galaxy halos . . . . . 86
3.1 Black hole growth . . . . . 86
3.2 Impact of AGN feedback on X-ray luminosity . . . . . 89
3.3 Baryonic mass budget . . . . . 89
3.4 Star formation . . . . . 94
3.5 Galaxy size . . . . . 94
4 Summary . . . . . 97
Bibliography . . . . . 98

# Chapter 1

# Momentum Driving: Which Physical Processes Dominate Active Galactic Nucleus Feedback?


## ABSTRACT

The deposition of mechanical feedback from a supermassive black hole in an active galactic nucleus (AGN) into the surrounding galaxy occurs via broad-line winds which must carry mass and radial momentum as well as energy. The effect can be summarized by the dimensionless parameter $\eta = \dot{M}_{\rm outf}/\dot{M}_{\rm acc} = 2\epsilon_{\rm w}c^2/v_{\rm w}^2$ where $\epsilon_{\rm w}$ ($\equiv \dot{E}_{\rm w}/(\dot{M}_{\rm acc}c^2)$) is the efficiency by which accreted matter is turned into wind energy in the disc surrounding the central black hole. The outflowing mass and momentum are proportional to $\eta$, and many prior treatments have essentially assumed that $\eta = 0$. We perform one- and two-dimensional simulations and find that the growth of the central black hole is very sensitive to the inclusion of the mass and momentum driving but is insensitive to the assumed mechanical efficiency. For example in representative calculations, the omission of momentum and mass feedback leads to an hundred fold increase in the mass of the black hole to over $10^{10}M_{\odot}$. When allowance is made for momentum driving, the final black hole mass is much lower and the wind efficiencies which lead to the most observationally acceptable results are relatively low with $\epsilon_{\rm w} \lesssim 10^{-4}$.

# 1 Introduction

Feedback from active galactic nuclei (AGNs) at the centers of galaxies is believed to have a significant effect on the evolution of those galaxies. However, the precise physical mechanisms by which this feedback occurs are greatly uncertain—perhaps more so than is commonly acknowledged. While much path-breaking and insightful work has been done, it is also true that some of the most basic requirements, such as the necessity that mass, energy, and momentum be conserved, have not been imposed in several of the popular treatments of this subject. And the inclusion of the presently known and observed feedback processes is often treated selectively. The purpose of this chapter is to attempt to lay out the physical framework for discussing the issues and to provide illustrative examples of the results obtained primarily from one-dimensional computations that include or exclude specific processes. We also include a treatment of the three-dimensional, axisymmetric case, presented in less detail, to show how the qualitative features carry over to this more realistic case. Definitive solutions are beyond present art in this field, so the focus will be on the qualitative features of the physical solutions rather than the detailed comparison with observations.

In outline, there are three phases to the overall phenomenon: 1) the provision of fuel for the central black hole; 2) the generation of the outflowing stream of energy, mass and momentum from the vicinity of the black hole; and 3) the absorption and transmission of this energy, mass and momentum by the ambient gas in the galaxy and the subsequent reactions of the ambient gas to that input.

The provision of fuel for the central black hole The fueling is generally believed to be via infalling gas, and typically, two origins for that gas have been proposed; at high redshift ambient gas in discs liberated by the non-axisymmetric forces released during mergers is certainly important (Barnes & Hernquist, 1991), while at lower redshift mergers fail and probably do not fuel AGNs (Li et al., 2008), but the processed gas released via normal stellar evolution provides an ample source (Mathews, 1983; Shull, 1983; Ciotti et al., 1991; Padovani & Matteucci, 1993; Ciotti & Ostriker, 2007). A primary clue as to which of these sources dominates in a specific case

is provided by details of the metallicity distribution, since the reprocessed gas probably has super-solar metal abundance and will also show signs of stellar evolution such as higher nitrogen or S-process abundances. The clue to fueling by infalling globular clusters might be relatively low abundances of elements made in SN I such as Fe. In almost all treatments a central disc mediates between the inflowing material and the black hole. Other sources, such as small stellar systems dragged in by dynamical friction have been considered from time to time. These stars, or others added to the central regions via loss-cone processes (Begelman et al., 1980) can be shredded during tidal interactions with the central black hole or by collisions with one another or with a central disc—the debris collecting in the disc and feeding the central black hole via conventional mechanisms (Ostriker, 1983; Dai et al., 2010).

The outflows fall into three categories. The signature of AGNs is, of course, the enormous electromagnetic, luminous output, with major contributions from the IR bands to the gamma ray region. The bulk of the flux is typically in the "UV bump" and the flux from this region thus dominates for the "momentum driven winds" (e.g., see Proga et al., 2000; King, 2003; Proga & Kallman, 2004; Debuhr et al., 2010). The region where this driving occurs is fairly close to the quasar ($50R_{\rm BH} \lesssim r \lesssim 500R_{\rm BH}$, where $R_{\rm BH}$ is the black hole Schwarzschild radius). However, the moderately hard X-rays determine the average photon energy: $\langle h\nu \rangle = h \int L_\nu \nu {\rm d}\nu / \int L_\nu {\rm d}\nu$ when integrated over the spectrum. This region of the spectrum dominates the photon heating, causing the heated gas to approach the mean photon energy: $1.5kT_X = \langle h\nu \rangle$ with $T_X \sim 2 \times 10^7$K (Sazonov et al., 2004). The resultant heating occurs over an extended range of radii: 100 pc$< r <$3 kpc (Ciotti et al., 2009b, 2010), and it can be significant for $r \gtrsim 0.1$ pc (Proga, 2007). It can efficiently drive outflows as shown in a series of papers by Ciotti, Ostriker and collaborators (cf. Ciotti & Ostriker (2007) and references therein). For electromagnetic output there is, of course, no rest-mass component. The total energy emitted in this form has been established fairly accurately via the Soltan (1982) argument to be $\Delta E = \epsilon_{\rm rad} \Delta M_{\rm acc} c^2$ with $\epsilon_{\rm rad} \sim 0.1 - 0.15$ (Yu & Tremaine, 2002). The momentum output, of course, is $\Delta p = \Delta E/c$. In optically thick cases ($\tau \gg 1$), the total momentum absorbed by the fluid can approach $\Delta p = \tau \Delta E/c$ (Debuhr et al., 2010). Silk & Nusser (2010) also consider the importance of radiative momentum driven winds on

galactic and cluster scales but limit the input to $L/c$, which can be considerably less than allowed in the optically thick case by Ciotti & Ostriker (2007) or Debuhr et al. (2010).

Next, let us turn to mechanical output. Both broad- and narrow-line regions inject mass, energy and momentum into the surrounding gas, with the broad-line winds probably dominant. Since these are material flows with velocity in the vicinity of the black hole, $v_{\rm w}$, the mass outflow can be considerable. If we let the inflowing and outflowing mass rates be ($\dot{M}_{\rm inf}$, $\dot{M}_{\rm outf}$), then conservation of mass, energy and momentum can be summed up with the following simple equations:

$$\dot{M}_{\rm acc} = \dot{M}_{\rm inf} - \dot{M}_{\rm outf}, \tag{1.1}$$

where $\dot{M}_{\rm acc}$ is the mass rate actually accreted by the black hole, and

$$\dot{E}_{\rm w} = \frac{1}{2}\dot{M}_{\rm outf} v_{\rm w}^2 \tag{1.2a}$$

$$= \epsilon_{\rm w}\dot{M}_{\rm acc} c^2, \tag{1.2b}$$

$$\dot{p}_{\rm w} = \dot{M}_{\rm outf} v_{\rm w}, \tag{1.3}$$

are the wind energy and momentum, respectively. We have oversimplified matters by allowing only one wind velocity, when in fact Equation 4.5b requires $\left\langle v_{\rm w}^2 \right\rangle$ and Equation 4.4 requires $\langle v_{\rm w} \rangle$. Also, it is important to specify exactly where and when the quantities in equations 4.3–4.4 are to be measured. In the conventional treatment of this subject, the black hole is surrounded by a disc or torus to which matter has fallen from larger radius. Then, placing a sphere around this disc or torus (at $r \sim 1$ pc), the instantaneous spherically averaged infall through the sphere is $\dot{M}_{\rm inf}(t)$ and the spherically averaged outflow is $\dot{M}_{\rm outf}(t)$. The difference will be accreted onto the black hole unless driven out in disc originating winds; the latter of course contributes to $\dot{M}_{\rm outf}$ and so the remainder $\dot{M}_{\rm inf} - \dot{M}_{\rm outf}$ will be accreted. Two further complications are allowed for in some detailed treatments: (i) the actual instantaneous value of $\dot{M}_{\rm acc}$ is a time-lagged convolution of the quantity in Equation 4.3 since a finite time elapses as material is transported through the disc to the central black hole and (ii) star formation may (in fact frequently will) occur in the disc,

removing mass that would otherwise have accreted onto the black hole. Both of these complications are allowed for in Ciotti & Ostriker (2007) and other work, neither is of dominant importance.

Now, defining the dimensionless ratio from Equation 4.5b and 4.5a to be,

$$\eta \equiv \frac{\dot{M}_{\rm outf}}{\dot{M}_{\rm acc}} = \frac{2\epsilon_{\rm w} c^2}{v_{\rm w}^2}, \tag{1.4}$$

we can now rewrite Equations 4.3–4.4 as

$$\dot{M}_{\rm acc} = \dot{M}_{\rm inf}\frac{1}{1+\eta}, \tag{1.5a}$$

$$\dot{M}_{\rm outf} = \dot{M}_{\rm inf}\frac{\eta}{1+\eta}, \tag{1.5b}$$

$$\dot{E}_{\rm w} = \frac{1}{2}\dot{M}_{\rm inf} v_{\rm w}^2 \frac{\eta}{1+\eta} = \epsilon_{\rm w}\dot{M}_{\rm inf} c^2 \frac{1}{1+\eta}, \tag{1.5c}$$

$$\dot{p}_{\rm w} = \dot{M}_{\rm inf} v_{\rm w} \frac{\eta}{1+\eta}. \tag{1.5d}$$

These Equations, 2.10a-d, are, in fact, the ones that most authors have adopted who treat AGN feedback as a unified process comprising both infall and outflow. However, they typically adopt $\eta = 0$, implicitly assuming $v_{\rm w} \to \infty$, so that $\dot{M}_{\rm outf}$ and $\dot{p}_{\rm w}$ are neglected and the two terms that are included, $\dot{E}_{\rm w}$ and $\dot{M}_{\rm acc}$, may be overestimated. If it eventuated that $\eta$ really is a very small number, then not much error would be induced and one would be justified in neglecting the out-flowing mass and momentum and in setting $\dot{E}_{\rm w} \sim \epsilon_{\rm w}\dot{M}_{\rm inf}c^2$, as most authors assume. If we adopt for the efficiency of generating mechanical energy the value $\epsilon_{\rm w} = 5 \times 10^{-3}$, as done by Springel et al. (2005); Johansson et al. (2009), hereafter SDMH05 and JNB09 respectively, McCarthy et al. (2010) and other authors, and we take $v_{\rm w} = 10^4$ km/s ($v_{\rm w,10}$) (Moe et al., 2009), then we have from Equation 1.4, $\eta = 9v_{\rm w,10}^{-2}$ and all of the neglected effects may in fact be dominant; the bulk of the inflowing mass may be ejected in a broad-line disc wind, and the mass and momentum input deposited in the ambient gas may dominate over the energy input, which may be largely radiated away. (Ciotti et al., 2009b, 2010) do include these effects, but do not spell out their significance. The principal purpose of the present chapter is to do just that—to

show, in specially simple one- and two-dimensional calculations the effects of including or excluding mass, energy and momentum conservation when $\eta > 0$. In addition to the papers referred to above which attempt to compute both the infall to the central black hole and the outflow from it in a unified fashion, there are many others which postulate a central source and then, after estimating the mass, momentum and energy flowing at of that source (and some angular and temporal distribution thereof) do effectively compute the effects of that injection of energy, mass and momentum onto the surrounding fluid. Space does not permit a comprehensive description of this related subject of research, but important papers include the following: cf. Metzler & Evrard (1994); Sternberg & Soker (2008); Fabian et al. (2009); Reeves et al. (2009); Arieli et al. (2010); Gaspari et al. (2011).

The wind efficiency, $\epsilon_{\rm w}$, is not known very well—neither from observations nor from detailed physical simulations. But the best estimates from either of these sources might be in the range $1 \times 10^{-3} > \epsilon_{\rm w} > 3 \times 10^{-4}$ (Proga et al., 2000; Proga & Kallman, 2004; Krongold et al., 2007; Stoll et al., 2009; Kurosawa et al., 2009), a factor of 5 to 17 smaller than the commonly adopted values and in a range where $\eta \lesssim 1$ if $v_{\rm w,10} \approx 1$. A specific example may be useful. Moe et al. (2009) study the quasar SDSS J0838+2955. They find a mechanical energy output of $4.5 \times 10^{45}$ erg/s, a mass outflow rate 10 times the accretion rate and a mechanical efficiency of $1 \times 10^{-3}$, and they quote other observational studies which indicate similar numbers. From analyses of the ionization parameters in the broad-line winds, estimates of the radial extent of the winds can be made; the above paper, and those quoted within indicate radii measured in kpc—consistent with the one-dimensional numerical work in Ciotti et al. (2010)

As shown in (Ciotti et al., 2009b, 2010), an additional important question asks "what fraction of the sky is covered with the broad-line winds?" Again two approaches are possible. Empirically, on the order of 20-25% of bright quasars show broad-line winds; this translates to $\sim \pi$ steradians or $\pi/2$ steradians in each conical outflow, if we assume that the wind is emitted symmetrically above and below the inner AGN disc. On the theory side, the radiation driven winds found by Proga & Kallman (2004), via detailed hydro radiation-transfer calculations, cover $\sim \pi$ steradians, roughly consistent with the observational estimates.

Finally, let us turn to the narrow jets, the outflow observed from AGN in "radio mode", when the electromagnetic luminosity is considerably below the Eddington limit. M87 is an excellent nearby example of such a system. These are standard FRI radio sources. Here the jets are quite narrow and appear to be comprised primarily of a relativistic fluid. The same type of calculation as presented in the last section would indicate that the out-flowing mass is of negligible importance and the energy output greatly dominates over the momentum output. The total energy output from these phases is considerable, but the accretion rates are thought to be low in these phases so the efficiencies of energy generation may be very high (cf. for a computation McKinney & Gammie, 2004). Since so little mass is accreted in radio mode, the Soltan argument cannot be used to empirically estimate efficiencies, but, from the observational estimates of the energies available in the giant radio lobes, it may be that the AGN emits in radio mode considerably more energy than it does in wind mode. However the deposition from the intense but extremely narrow streams appears to be inefficient, and the jet drills through the gas in the surrounding galaxy, dumping most the energy into the intergalactic medium. Thus, while it may act as the dominant feedback mechanism for the IGM (and we will return to this in a subsequent paper), it is of lesser importance than the radiative or wind components in heating and driving out the ambient gas from within a galaxy.

The interactions between the outflowing energy, mass and momentum with the ambient fluids are complex and are just beginning to be studied with the needed detail. We focus here on the relatively gas poor elliptical systems, since it is in these that the bulk of the mass in black holes is found, The radiative interactions are perhaps easiest to describe. Since the mechanical momentum is conserved and cannot be radiated away, it can be a dominant effect. The minimum level of interaction is provided by electron scattering and, since the most luminous quasars are found to be clustered near the Eddington luminosity limit (at which level the momentum absorbed by electron scattering balances the gravitational force on the fluid from the central black hole), we know that this effect is significant in many cases. Absorption of the out-flowing radiation will not, in general, reduce this effect, since typically the radiation is simply re-emitted in another band and electron scattering opacity is wavelength independent until the Klein-Nishina

limit is reached at very high energies. In fact, in the optically thick limit, the radiation is transformed by dust absorption into the infra-red, but the effects in this case are even greater than in the simple case, since the scattering opacity of the dust to infra-red is, per atom, larger (by roughly a factor of 5) than the electron scattering cross section. For the bright ULIRGs, which may contain both an active AGN and a brighter starburst, there will be a near balance between the inward gravitational forces and the outward radiative momentum transfer on the dust (cf. Thompson et al., 2005; Ciotti & Ostriker, 2007). Under these circumstances, the inner several hundred parsecs of the galaxy are analogous in their equilibrium structure to a very massive star in so far as there is a nearly equilibrium balance between radiative and gravitational forces.

The effects of heating from the AGN are, for quite different reasons, also likely to be independent of absorption (so long as it is not excessive, i.e. not Compton thick). Sazonov et al. (2005) present a simple analytical exploration of the effects and Paper I presents a more detailed one-dimensional treatment. The photons which dominate the heating process are in the moderately hard region (∼50keV), and we know from X-ray absorption studies that AGN are typically optically thin to such radiation. Metal line resonance absorptions dominate the absorption unless the spectrum is extremely hard, and in those cases Compton absorption would be dominant. If we consider the issue on a per atom basis, all that matters is the heating per atom, which scales as $r^{-2}$ (assuming that the fluid is optically thin to hard X-rays), and the cooling rate per atom which scales as the density. Since the latter can also scale as $r^{-2}$ or even falls off at a steeper rate in some circumstances, the heating can balance or exceed cooling over an extended range of radii. If that happens, the gas temperature will rise towards the radiation temperature, $T_X \sim 2 \times 10^7$ K. Then, since this exceeds the virial temperature in almost all galaxies, the heated gas, having thermal energy higher than its gravitational energy, will be accelerated outwards and tend to drive a wind into the surrounding fluid. Of course, since this will shut off the accretion flow and the fuel to the central source, the result will be a burst of energy output followed by much slower cooling of the shocked gas and a repeated burst at a much later time. Thus, episodic accretion is expected.

The mechanical energy input is more localized to the vicinity of the black hole and would be efficient in "protecting" the black hole from very high rates of accretion, except for one important caveat. It necessarily happens that such episodes of high rates of energy deposition will occur when the central gas densities are high, and under such circumstances the gas will tend to radiate away the input energy unless forbidden to do so as has occurred in some calculations (Booth & Schaye, 2009). This, as we shall see, makes the energy input rather inefficient in driving outflows and in protecting the black hole from excessive accreation. But the momentum input cannot be radiated away, and, as we shall see in the remainder of the chapter, it is very efficient in limiting the infall and accretion onto the central black hole. Mechanical input, via either thermal or momentum based mechanisms, will also tend to produces episodic accretion.

The broad-line gas outflow must drive a strong shock into the ambient gas, and that, in turn, given standard physics, should accelerate charged particles efficiently via a variant of the first order Fermi process (cf. Blandford & Ostriker, 1978; Bell, 1978; Blandford & Eichler, 1987). Then this relativistic fluid will further drive the outflow and, since thermal radiation is suppressed for this component, the conversion may somewhat enhance the effects of feedback. But, overall, this process simply transforms internal energy from one form to another and so, whereas it may be observationally quite significant, it will have a relatively small global effect. Two recent papers that have explored these processes are Fujita et al. (2007) and Jiang et al. (2010); see also Sironi & Socrates (2010).

This chapter is organized as follows. In Section 2, we describe how the new galaxy models adopted in the simulations are built, in Section 3, the details of the input physics (focusing in particular on the physics of accretion disk and on the mechanical feedback), and their numerical implementation. Finally, in Section 4 we discuss the main results obtained.

## 2 Models

In this section, we summarize the main properties of the galactic models adopted in this study. A detailed description of the galaxy models and input physics is given in CO07, Papers I and III.

We study galaxy models characterized by the effective radius of the galaxy stellar component $R_{\rm e} = 6.91$ kpc, an initial stellar mass $M_* = 2.87 \times 10^{11} M_\odot$, and central aperture velocity dispersion $\sigma_{\rm a} = 260$ km s$^{-1}$. This represents approximately the typical $L_*$ galaxy which Yu & Tremaine (2002) find contain the bulk of the identified mass in black holes. The stellar mass distribution which is embedded in a dark matter halo is described by the Jaffe (1983) model while the total mass density distribution follows a $r^{-2}$ profile; all the relevant dynamical quantities need in the simulation are given in Ciotti et al. (2009a). The initial black hole mass is $M_{\rm BH} = 2.87 \times 10^8 M_\odot$, following the Magorrian et al. (1998) relations ($M_{\rm BH} \sim 10^{-3} M_*$). The simulations are for an isolated, giant elliptical galaxy without the effect of the intracluster medium, as outflow boundary conditions are set at the galaxy outskirts ($\sim 250$ kpc), so that the interstellar medium (ISM) is provided by the recycled gas produced by stellar evolution. The simulations starts at 2 Gyr, which corresponds to a redshift of $z \sim 3.2$ for the $\Lambda$CDM cosmology with $\Omega_m = 0.3$, $\Omega_\Lambda = 1 - \Omega_m = 0.7$ and $H_0 = 70$ km s$^{-1}$ Mpc$^{-1}$ and ends at 14 Gyr.

The input physics of the model is fully described in Paper I. Here we recall the most important aspects. The instantaneous bolometric accretion luminosity is

$$L_{\rm BH} = \epsilon_{\rm EM} \dot{M}_{\rm acc} c^2, \tag{1.6}$$

and we adopt an advection-dominated accretion flow (ADAF)-like radiative efficiency as

$$\epsilon_{\rm EM} = \epsilon_0 \frac{A\dot{m}}{1 + A\dot{m}}, \qquad \dot{m} \equiv \frac{\dot{M}_{\rm acc}}{\dot{M}_{\rm Edd}}, \tag{1.7}$$

where $\dot{M}_{\rm Edd} = L_{\rm Edd}/\epsilon_0 c^2$, and $A$ is a free parameter so that $\epsilon_{\rm EM} \sim \epsilon_0 A\dot{m}$ for $\dot{m} \ll A^{-1}$. We fix $A = 100$ in our simulations (Narayan & Yi, 1994), and we adopt for the peak EM efficiency $\epsilon_0 = 0.1$ or 0.2 consistent with estimates based on the Soltan (1982) argument. In the treatment of radiation feedback, we consider the radiation pressure as well as heating/cooling feedback, including photoionization, Compton and line heating (Sazonov et al., 2004, 2005). In accordance with both observations and theoretical expectation, the transformation of accreted mass to electromagnetic energy output declines dramatically at low accretion rates.

In the mechanical feedback treatment, the fiducial instantaneous mechanical luminosity of the disk wind is calculated as

$$L_{\rm dw} = \epsilon_{\rm w}\dot{M}_{\rm acc}c^2 + \epsilon_{\rm II}c^2(1-f_{\rm rem,h})\frac{M_{\rm dh*}}{\tau_{*\rm h}} \tag{1.8}$$

where $\epsilon_{\rm w}$ is the mechanical efficiency of the wind, and the second term represents the energy associated with the Type II supernova (SNII) explosions of the high-mass stars in the circumnuclear disk (see Paper I, Equation (20) for details). Here, $M_{\rm dh*}$ is the current mass in the disc in high mass ($M > 8M_{\odot}$) and $\tau_{*\rm h}$ is their typical lifetime. In this work, we restrict attention to the commonly assumed case of a constant value of $\epsilon_{\rm w}$ (e.g. SDMH05), which corresponds to Type A models in Papers I and III. Physically, a fixed mechanical efficiency implies that the mass accreted by the central black hole has a fixed relation to the mechanical energy flowing out of the central regions. We here neglect the jet effects, which are expected to be effective only in the low-luminosity, hot accretion phases at late-time evolution. The reference models (A0 and A1) from Paper III study the evolution of gas and the mechanical feedback from black holes, and solve Eulerian equations of hydrodynamics with mass, energy, and momentum sources (see Paper I). In order to study the effect of each physical process, i.e., mass, energy, and momentum feedback, we build several models which neglect one or two of physical terms. We discuss the details of each model and comparison of them in the following section.

## 3 Exploring one-dimensional models

The model properties and results are given in Table 1. The mechanical efficiencies $\epsilon_{\rm w}$ are given in Column 3 and the corresponding values of $\eta \equiv 2\epsilon_{\rm w}c^2/v_{\rm w}^2$ are given in Column 4. We devote Column 5-9 to present ($z = 0$) model properties. First, for some models indicated with the symbol $\surd$ in Column 5, we distribute the mechanical feedback energy (momentum and mass) only at the lower boundary of the grids to mimic the common treatment of mechanical feedback (e.g. SDMH05, Di Matteo et al., 2005, JNB09). Instead, models indicated with the symbol $\times$ in

Table 1.1: Summary of One-dimensional Model Properties

| | | | | | Feedback | | | | | | | |
|---|---|---|---|---|---|---|---|---|---|---|---|---|
| | Model | $\epsilon_{\rm w}$ | $\eta(v_{\rm w,10}^{-2})^a$ | Bottom Layer$^b$ | Radiation | Energy | Momentum | Mass | log $\Delta M_{\rm BH}$ | log $L_X$ | log $l_{\rm BH}^{\rm eff}{}^c$ | log $\Delta E_{\rm w}{}^d$ |
| (1) | (2) | (3) | (4) | (5) | (6) | (7) | (8) | (9) | (10) | (11) | (12) | |
| 1 | A0 $^e$ | $5\times10^{-3}$ | 9 | × | √ | √ | √ | √ | 6.72 | 37.11 | -7.98 | 58.67 |
| 2 | MA0 $^e$ | $5\times10^{-3}$ | 9 | × | × | √ | √ | √ | 6.72 | 37.11 | -7.98 | 58.67 |
| **3** | **EPM0-R** | $\mathbf{5\times10^{-3}}$ | **9** | √ | √ | √ | √ | √ | **7.07** | **39.75** | **-10.58** | **59.02** |
| 4 | EPM0 | $5\times10^{-3}$ | 9 | √ | × | √ | √ | √ | 7.13 | 37.84 | -10.58 | 59.08 |
| 5 | PM0 | $5\times10^{-3}$ | 9 | √ | × | × | √ | √ | 7.13 | 37.84 | -10.58 | 59.08 |
| **6** | **E0** $^f$ | $\mathbf{5\times10^{-3}}$ | **9** | √ | × | √ | × | × | **10.32** | **41.31** | **-3.61** | **62.27** |
| 7 | A1 $^e$ | $2.5\times10^{-4}$ | 0.45 | × | √ | √ | √ | √ | 7.38 | 36.36 | -6.72 | 58.02 |
| 8 | MA1 $^e$ | $2.5\times10^{-4}$ | 0.45 | × | × | √ | √ | √ | 7.52 | 38.09 | -6.48 | 58.17 |
| **9** | **EPM1-R** | $\mathbf{2.5\times10^{-4}}$ | **0.45** | √ | √ | √ | √ | √ | **8.04** | **39.59** | **-8.23** | **58.69** |
| 10 | EPM1 | $2.5\times10^{-4}$ | 0.45 | √ | × | √ | √ | √ | 7.76 | 38.82 | -8.15 | 58.41 |
| 11 | PM1 | $2.5\times10^{-4}$ | 0.45 | √ | × | × | √ | √ | 7.76 | 38.82 | -8.15 | 58.41 |
| **12** | **E1** $^f$ | $\mathbf{2.5\times10^{-4}}$ | **0.45** | √ | × | √ | × | × | **10.33** | **41.29** | **-3.62** | **60.98** |
| 13 | EPM2-R | $1\times10^{-3}$ | 1.8 | √ | √ | √ | √ | √ | 7.59 | 40.13 | -9.25 | 58.85 |
| 14 | EPM3-R | $1\times10^{-4}$ | 0.18 | √ | √ | √ | √ | √ | 8.24 | 40.39 | -7.79 | 58.50 |
| 15 | EPM4-R | $5\times10^{-5}$ | 0.09 | √ | √ | √ | √ | √ | 8.29 | 40.03 | -7.51 | 58.25 |
| 16 | EPM5-R | $2.5\times10^{-5}$ | 0.045 | √ | √ | √ | √ | √ | 8.78 | 40.33 | -5.77 | 58.43 |
| 17 | EPM6-R | $1\times10^{-5}$ | 0.018 | √ | √ | √ | √ | √ | 9.11 | 40.50 | -5.30 | 58.37 |
| 18 | EPM7-R | $5\times10^{-6}$ | 0.009 | √ | √ | √ | √ | √ | 9.29 | 39.97 | -5.14 | 58.24 |

**Note.** Model names (except for Model 1, 2, 7 and 8) indicate the activated physics (symbol √) in the simulations as detailed in Column 6-9. For example, in E0 and E1 models only mechanical energy feedback is allowed, while in PM0 and PM1 models momentum and mass are considered, but not mechanical energy. We adopt 0.2 for the peak EM efficiency $\epsilon_0$.

$^a\eta = 2\epsilon_{\rm w}c^2/v_{\rm w}^2$ in $v_{\rm w,10}^{-2}$ unit where $v_{\rm w} = 10,000$km/s

$^b$Models with mass, energy and momentum added to the bottom layer.

$^c l_{\rm BH}^{\rm eff} \equiv L_{\rm BH,opt}^{\rm eff}/L_{\rm Edd}$ where $L_{\rm BH}$ is the black hole luminosity in the optical band after absorption, i.e., as it will be seen from infinity.

$^d\Delta E_{\rm w} \equiv \epsilon_{\rm w}\Delta M_{\rm BH}c^2$, in erg, where $\Delta M_{\rm BH}$ is in $M_\odot$ units.

$^e$ These models correspond to the models A0, MA0, A1 and MA1 in Papers I and III, but calculated with some difference in the numerical grid spacing.

$^f$ The model similar to one adopted in SDMH05.

Column 5 have a distributed feedback as in Papers I and III where we attempt to estimate the gradual deposition of mass, energy and momentum taken from the outflowing wind and going into the ambient gas as a function of radius. We then build several models which neglect one or two of physical process, i.e., mass, energy, and momentum feedback in order to study their effects showing the inclusion of each term in Column 6-9. For example, Model 3 (EPM0-R, in bold face) distributes the mechanical feedback only into the bottom layer, and includes the radiation feedback and all physical terms, i.e., mass, energy, and momentum, in the mechanical feedback. On the other hand, Model 6 (E0) adopts a treatment similar to that in SDMH05 as it assumes the same mechanical feedback efficiency, only includes the mechanical energy feedback and distributes it into the bottom layer of the grid, neglecting the mass and momentum added back into the flow.

Models 1-6 adopt the standard (high) efficiency $\epsilon_{\rm w} = 5 \times 10^{-3}$, as SDMH05 and JNB09 and Models 7-12 assume a factor of 20 lower efficiency, perhaps in better accord with observationally based estimates (Moe et al., 2009; Arav et al., 2013) and Models 13-18 adopt other efficiencies to show how final properties depend on the assumed mechanical efficiency.

### 3.1 High efficiency models

To mimic the common treatment (e.g., SDMH05, JNB09), we build the Model 6 (E0) that only includes the Mechanical energy feedback with the standard (high) efficiency $\epsilon_{\rm w} = 5 \times 10^{-3}$. In this model, we estimate the mass inflowing to the black hole, convert it to energy with the given efficiency, and add this energy only into the bottom layers of the surrounding gases. For comparison, Model EPM0-R has identical efficiency but adds also mass and momentum to the bottom layers using Equations (5a-d) with $\eta = 9$, as appropriate for the chosen efficiency and wind velocity of $v_{\rm w,10} = 1$. These two models are shown as blue and green lines in Figure 1.1. We see that allowing for momentum and mass feedback reduces the black hole growth by a factor of 1000. The more consistent model has a much lower final X-ray luminosity and final black hole Eddington ratio. The effect of including or not including radiative heating is relatively minor, as can be seen by comparing Models 3 and 4 or 1 and 2. Also the mechanical energy feedback is

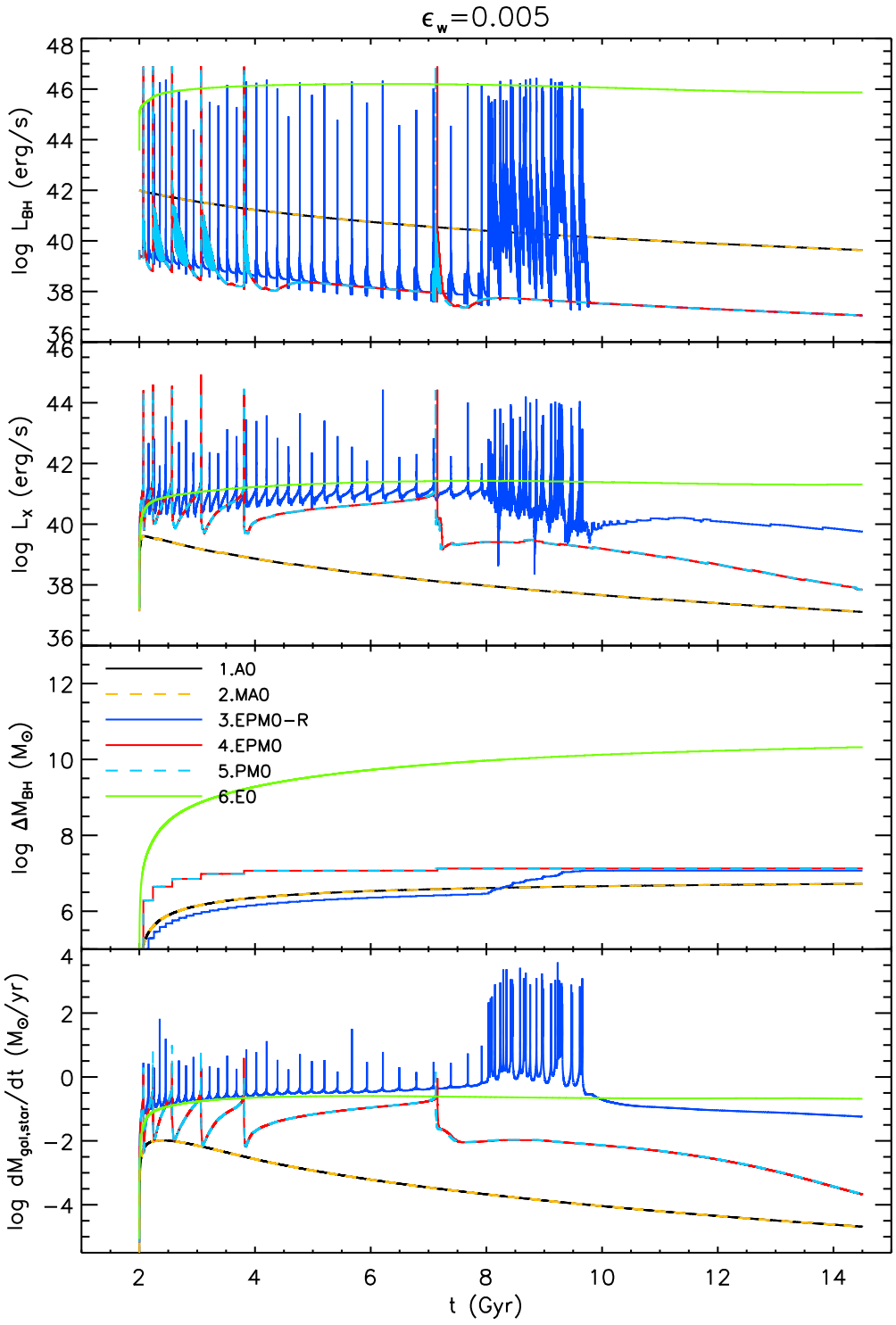



Figure 1.1: Models 1-6 with constant and high mechanical efficiency $\epsilon_{\rm w} = 5 \times 10^{-3}$ ($\eta = 9$). From top to bottom, the black hole luminosity, X-ray luminosity, mass accreted on the central black hole, and star formation rate are shown with different line types and colors as indicated in the third panel. Note how the model that excludes momentum feedback, "E0", has by far the highest growth of the central black hole.

considerably less important (as expected) than the momentum input, as can be seen by comparing Models 4, 5, and 6. Finally it might be thought that some of the effects observed in these comparisons are due to the change from Paper I of adding the feedback to the bottom layers alone in the present simulations, rather than over a distributed range of radii to mimic the effects of due to a broad line wind. But comparison between Models 1 and 3, where there are only small differences (and Model 1 is identical to A0 of Paper III), shows that the differences which may be attributed to distributed feedback are small. In summary, examination of Models 1-6 shows that including momentum drastically increases the effects of feedback.

### 3.2 Low efficiency models

Next, we turn our attention to Models 7-12 which have a much lower mechanical efficiency than typically assumed and it is at a level better in accord with existing (and highly imperfect) observational indications. The value for the dimensionless parameter $\eta$ in these cases is only 0.45 (i.e. of order unity), so that we expect that inclusion or exclusion of the mass and momentum input will make relatively less difference. What do we find? In fact, the differences are reduced by about half an order of magnitude (0.5 dex), but it remains true that the Model 12 (like Model 6), without either momentum feedback or radiation, has an unacceptably large growth of the central black hole and an unacceptably large final black hole luminosity, as shown in Figure 1.2. Models 6 and 12 also show thermal X-ray emission greater than $10^{41}$ erg/s, which is on the upper side of what is typically observed in normal elliptical galaxies.

We summarize the properties of Models 1-12 in Figure 1.3 showing the present-day (14 Gyr) black hole mass in solar mass versus X-ray gas and optical stellar luminosities. We show the high efficiency models (Models 1-6) in blue and the low efficiency models (Models 6-12) in red. The fiducial models, Models EPM0-R and EPM1-R with mass and momentum feedback, and Models E0 and E1 that only include energy feedback, are marked with their model numbers. As discussed above, including the momentum and mass feedback not only significantly reduces the black hole

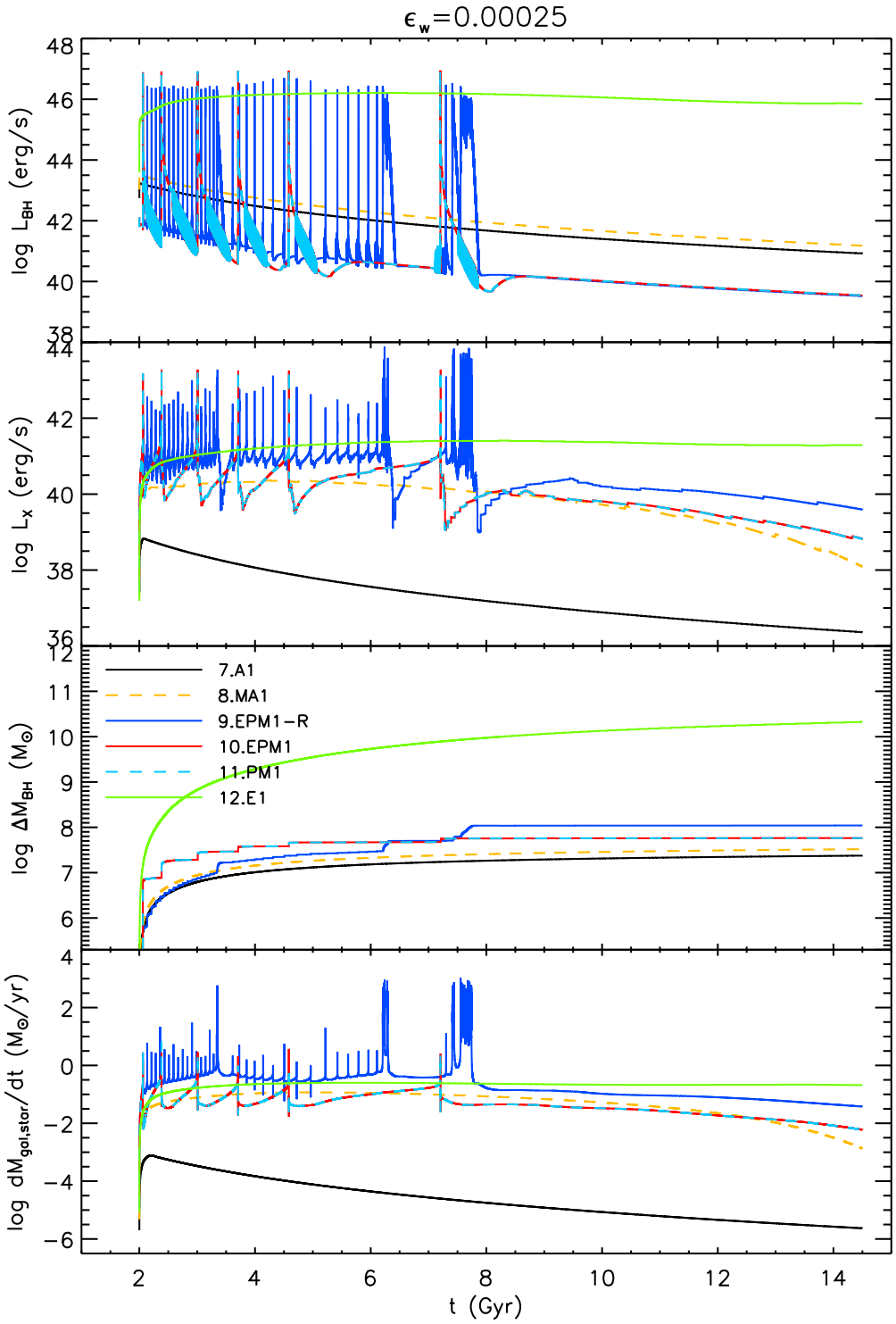



Figure 1.2: Models with constant and low (observation based) mechanical efficiency, $\epsilon_{\rm w} = 2.5 \times 10^{-4}$ ($\eta = 0.45$). From top to bottom, the black hole luminosity, X-ray luminosity, mass accreted on the central black hole, and star formation rate are shown, colors and line types as in Figure 1.1. Again momentum feedback is the most important physical process in protecting the central black hole from excessive growth.

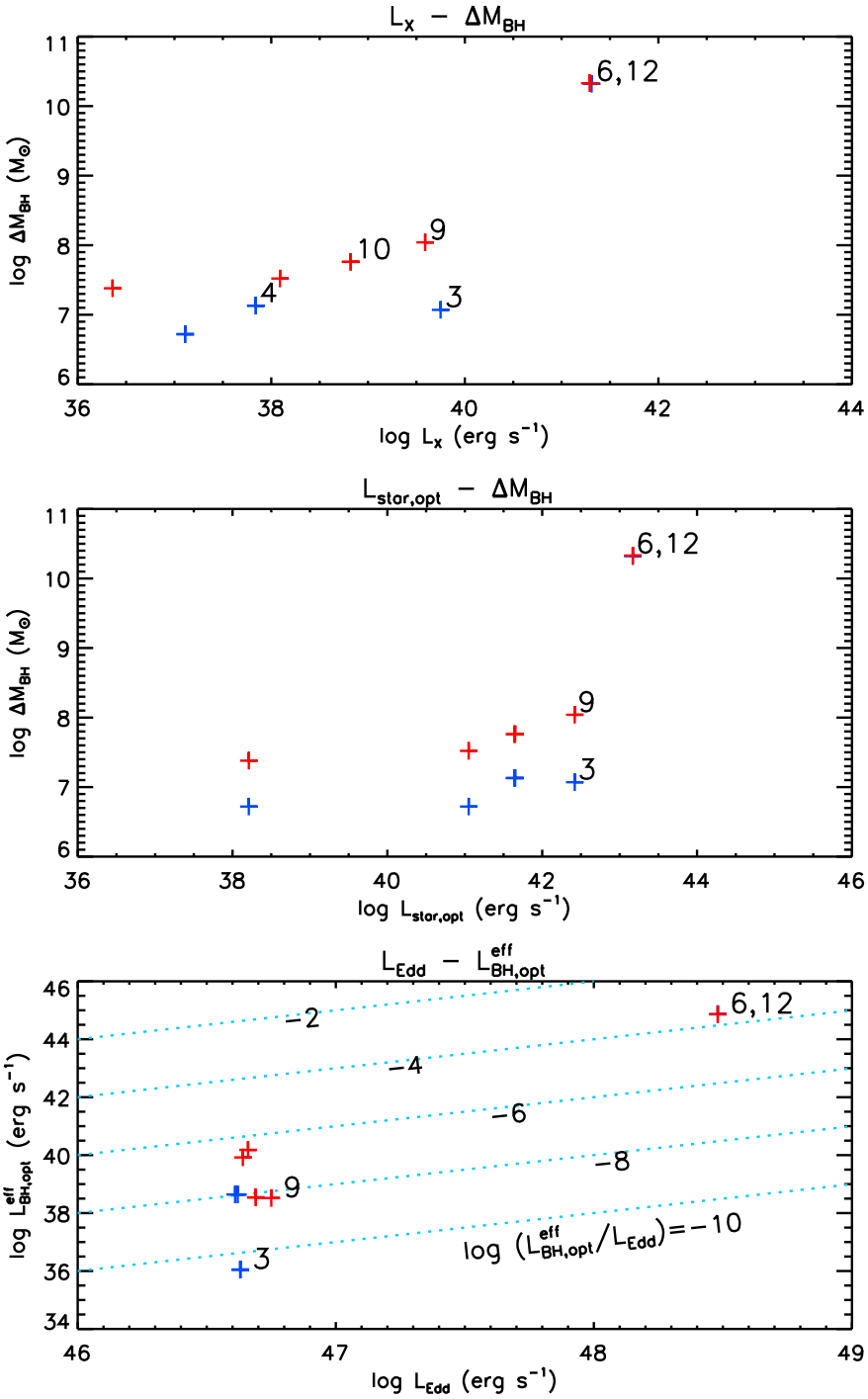



Figure 1.3: Distribution of all models in the mass-luminosity diagram measured at z=0, where different colors show different wind efficiencies and $\eta$ values ($\epsilon_w = 5 \times 10^{-3}$ and $\eta = 9$ for blue, $\epsilon_w = 2.5 \times 10^{-4}$ and $\eta = 0.45$ for red). The distribution of models in the Eddington luminosity - effective black hole luminosity plane is shown in the bottom panel. Five diagonal lines (from top to bottom) show $l^{\rm eff}_{\rm BH} = L^{\rm eff}_{\rm BH,opt}/L_{\rm Edd} = 10^{-2}$, $10^{-4}$, $10^{-6}$, $10^{-8}$, $10^{-10}$ respectively.

growth but also results in a much lower final X-ray luminosity and final black hole Eddington ratio.

### 3.3 Wind efficiency dependence of bottom-layer models

We test eight different values of $\epsilon_{\rm w}$ for models ranging from $5 \times 10^{-6}$ to $5 \times 10^{-3}$ for models with the bottom-layer treatment and all feedback physics activated (i.e. Models EPM#-R). These models correspond to Models 3, 9, and 13-18 in Table 1. We summarize the results at the epoch of 14 Gyr in Figure 1.4, where the least square linear fits of several global quantities of interest are also given. Note here that the growth of black hole mass and the BH luminosity Eddington ratio are decreasing functions of $\epsilon_{\rm w}$. If the feedback efficiency is low, too much mass is accreted to the central black hole, as expected. In the case of the gas mass and the predicted X-ray luminosity of the hot ISM, they are decreasing functions with increasing wind efficiency but with large scatters. We also show the total mechanical feedback energy (i.e. $\Delta E_{\rm w} = \epsilon_{\rm w} \Delta M_{\rm BH} c^2$) in the last panel, which increases as the wind efficiency increases. In this case as in several of the others, while the behavior is approximately monotonic in the direction expected, the approximate power law index is much less than unity, since larger efficiency gives a larger value for our dimensionless parameter, $\eta$, and thus a smaller fraction of the inflowing gas is actually accreted onto the central black hole.

## 4 Discussion

The primary purpose of this chapter is to quantitatively show, based on one- and two-dimensional computations, exactly which processes are most important during AGN feedback episodes; which processes are most useful in protecting the central black hole from excessive mass growth and which have most effect on the ambient galaxy. After a central outburst, the mechanical energy must be communicated to the ambient gaseous fluid by a wind and we, in fact, see these winds in luminous galaxies labeling them "broad-line regions" with outflow velocities observed to be $\sim 10,000$ km/s covering conical regions subtending 20-25 % of the sky. These winds *must* carry mass and radial momentum to the ambient fluid, reducing thereby the mass deposited on the

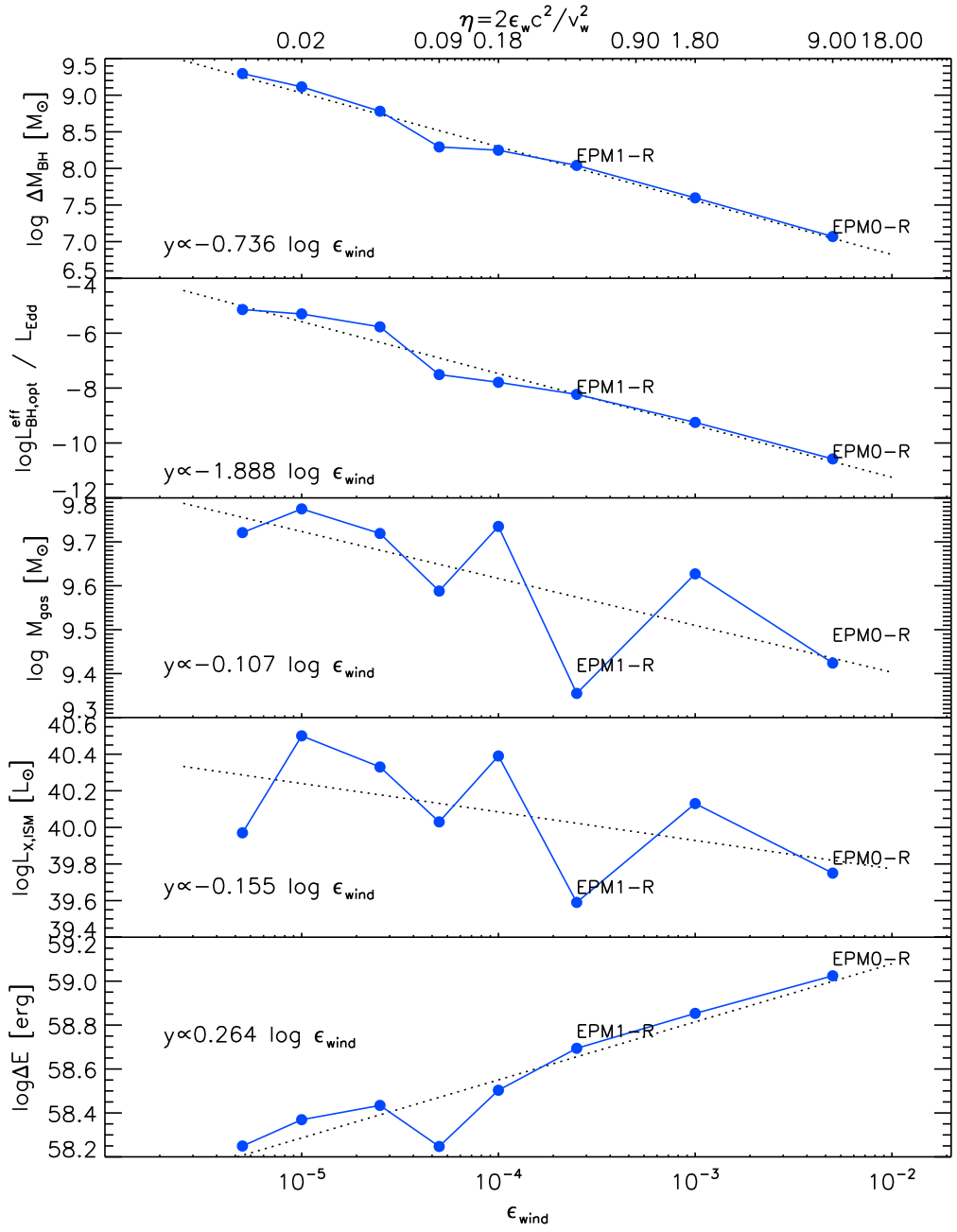



Figure 1.4: Dependencies of present-day, global quantities of EPM#-R models in Table 1, as a function of mechanical efficiency $\epsilon_{\rm w}$. From top to bottom, the black hole mass growth, BH Eddington ratio, galaxy gas mass inside 10 $R_{\rm e}$, X-raygas luminosity, and total wind feedback energy are shown. The linear fits to the data are shown in dotted lines, and the fitting results are shown in each panel. As expected, the assumption of a higher wind energy efficiency does correspond to greater feedback effects, but at a much less than linear rate.

central black hole and adding a driving component which cannot be reradiated away by thermal processes. Equations 5a-d summarize the physics, with the dimensionless parameter $\eta$, indicating the importance of mass and momentum outflows.

In the case of an assumed high mechanical efficiency ($\epsilon_{\rm w} = 0.005$), we find that, if we suppress the mass and momentum input, then the black hole grows by over a factor of 100 more than if momentum and mass flux were properly included in the calculation, and reaches masses $> 10^{10} M_{\odot}$ in both one- and two-dimensional calculations. Turning on or off the energy input has relatively much less effect, altering the black hole growth by roughly a factor of 2. Ignoring the mass and momentum feedback inputs also leaves the galaxy with a central optical luminosity from the AGN which is orders of magnitude brighter than is seen in nearby elliptical systems.

Compared to these dramatic effects, the uncertainty due to not knowing accurately the wind efficiencies has a relatively minor effect. Reducing the efficiency by a factor of 20 from $5 \times 10^{-3}$ to $2.5 \times 10^{-4}$ reduces the wind energy output by only a factor of 2 (to $10^{58.7}$ erg) and reducing the efficiency by another factor of 10 reduces the wind energy output by only another factor of 2.

We also found that redirecting much of the inflowing mass into a BAL wind has, by itself, an important effect on models with only radiative feedback. In those computations, which do not allow for the redirection, the central black hole again grows far too much in both the one- and two-dimensional computations.

In summary, it eventuates that enforcing the conservation of mass, momentum and energy provides extremely useful constraints in estimating the growth of central black holes and the feedback effects on the surrounding galaxies.

# Bibliography

Arav, N., Borguet, B., Chamberlain, C., Edmonds, D., & Danforth, C. 2013, ArXiv e-prints

Arieli, Y., Rephaeli, Y., & Norman, M. L. 2010, ApJ, 716, 918

Barnes, J. E. & Hernquist, L. E. 1991, ApJ, 370, L65

Begelman, M. C., Blandford, R. D., & Rees, M. J. 1980, Nat, 287, 307

Bell, A. R. 1978, MNRAS, 182, 147

Blandford, R. & Eichler, D. 1987, Phys. Rep., 154, 1

Blandford, R. D. & Ostriker, J. P. 1978, ApJ, 221, L29

Booth, C. M. & Schaye, J. 2009, MNRAS, 398, 53

Ciotti, L., D'Ercole, A., Pellegrini, S., & Renzini, A. 1991, ApJ, 376, 380

Ciotti, L., Morganti, L., & de Zeeuw, P. T. 2009a, MNRAS, 393, 491

Ciotti, L. & Ostriker, J. P. 2007, ApJ, 665, 1038

Ciotti, L., Ostriker, J. P., & Proga, D. 2009b, ApJ, 699, 89

—. 2010, ApJ, 717, 708

Dai, L. J., Fuerst, S. V., & Blandford, R. 2010, MNRAS, 402, 1614

Debuhr, J., Quataert, E., Ma, C.-P., & Hopkins, P. 2010, MNRAS, 406, L55

Di Matteo, T., Springel, V., & Hernquist, L. 2005, Nat, 433, 604

Fabian, A. C., Vasudevan, R. V., Mushotzky, R. F., Winter, L. M., & Reynolds, C. S. 2009, MNRAS, 394, L89

Fujita, Y., Kohri, K., Yamazaki, R., & Kino, M. 2007, ApJ, 663, L61

Gaspari, M., Melioli, C., Brighenti, F., & D'Ercole, A. 2011, MNRAS, 411, 349

Jaffe, W. 1983, MNRAS, 202, 995

Jiang, Y.-F., Ciotti, L., Ostriker, J. P., & Spitkovsky, A. 2010, ApJ, 711, 125

Johansson, P. H., Naab, T., & Burkert, A. 2009, ApJ, 690, 802

King, A. 2003, ApJ, 596, L27

Krongold, Y., Nicastro, F., Elvis, M., Brickhouse, N., Binette, L., Mathur, S., & Jiménez-Bailón, E. 2007, ApJ, 659, 1022

Kurosawa, R., Proga, D., & Nagamine, K. 2009, ApJ, 707, 823

Li, C., Kauffmann, G., Heckman, T. M., Jing, Y. P., & White, S. D. M. 2008, MNRAS, 385, 1903

Magorrian, J., et al. 1998, AJ, 115, 2285

Mathews, W. G. 1983, ApJ, 272, 390

McCarthy, I. G., et al. 2010, MNRAS, 406, 822

McKinney, J. C. & Gammie, C. F. 2004, ApJ, 611, 977

Metzler, C. A. & Evrard, A. E. 1994, ApJ, 437, 564

Moe, M., Arav, N., Bautista, M. A., & Korista, K. T. 2009, ApJ, 706, 525

Narayan, R. & Yi, I. 1994, ApJ, 428, L13

Ostriker, J. P. 1983, ApJ, 273, 99

Padovani, P. & Matteucci, F. 1993, ApJ, 416, 26

Proga, D. 2007, ApJ, 661, 693

Proga, D. & Kallman, T. R. 2004, ApJ, 616, 688

Proga, D., Stone, J. M., & Kallman, T. R. 2000, ApJ, 543, 686

Reeves, J. N., et al. 2009, ApJ, 701, 493

Sazonov, S. Y., Ostriker, J. P., Ciotti, L., & Sunyaev, R. A. 2005, MNRAS, 358, 168

Sazonov, S. Y., Ostriker, J. P., & Sunyaev, R. A. 2004, MNRAS, 347, 144

Shull, J. M. 1983, ApJ, 264, 446

Silk, J. & Nusser, A. 2010, ApJ, 725, 556

Sironi, L. & Socrates, A. 2010, ApJ, 710, 891

Soltan, A. 1982, MNRAS, 200, 115

Springel, V., Di Matteo, T., & Hernquist, L. 2005, MNRAS, 361, 776

Sternberg, A. & Soker, N. 2008, MNRAS, 384, 1327

Stoll, R., Mathur, S., Krongold, Y., & Nicastro, F. 2009, ArXiv e-prints

Thompson, T. A., Quataert, E., & Murray, N. 2005, ApJ, 630, 167

Yu, Q. & Tremaine, S. 2002, MNRAS, 335, 965

# Chapter 2

# Consequences of Radiative and Mechanical Feedback from Black Holes in Isolated Disk Galaxies


**ABSTRACT**

We study the growth of black holes in galaxies using three-dimensional smoothed particle hydrodynamic (SPH) simulations with new implementations of the momentum mechanical feedback, and restriction of accreted elements to those that are gravitationally bound to the black hole. We also include the feedback from the X-ray radiation emitted bythe black hole, which heats the surrounding gas in the host galaxies, and adds radial momentum to the fluid. We perform simulations of isolated galaxies and merging galaxies and test various feedback models with the new treatment of the Bondi radius criterion. We find that overall the black hole growth is similar to what has been obtained by earlier workers using the Springel, Di Matteo, & Hernquist algorithms. However, the outflowing wind velocities and mechanical energy emitted by winds are considerably higher ($v_{\rm w} \sim 1000 - 3000$ km/s) compared to the standard thermal feedback model ($v_{\rm w} \sim 50 - 100$ km/s). While the thermal feedback model emits only 0.1% of black hole released energy in winds, the momentum feedback model emits more than 30% of the total energy released by the black hole in winds. In the momentum feedback model, the degree of fluctuation in both radiant and wind output is considerably larger than in the standard

treatments. We check that the new model of the black hole mass accretion agrees with analytic results for the standard Bondi problem.

# 1 Introduction

Accretion of matter onto a supermassive black hole is believed to emit enormous amounts of electromagnetic, luminous radiation and drive powerful jets, winds or outflows of quasar (Lynden-Bell, 1969; Rees, 1984). The energy outputs emitted by accreting black holes at the centers of bulges and elliptical galaxies(Kormendy & Richstone, 1995; Richstone et al., 1998) are believed to play an important role during galaxy formation and evolution, as revealed by many empirical correlations between their masses $M_{\rm BH}$ and host galaxy properties, *e.g.*, the dispersion $\sigma$ of the host galaxy (Gebhardt et al., 2000; Tremaine et al., 2002; Gültekin et al., 2009; Graham et al., 2011), bulge stellar mass (Dressler, 1989; Kormendy, 1993; Magorrian et al., 1998; Marconi & Hunt, 2003; Gültekin et al., 2009), and the bulge binding energy (Aller & Richstone, 2007; Barway & Kembhavi, 2007). These correlations have led to the development of models where the black holes are linked by feedback from the central black holes, *i.e.*, feedback via the mass ejection by winds or jets, or the emitted radiation regulates the mass accretion rate and the final black hole mass. The feedback can be in the forms of radiatively or mechanically driven winds (Fabian, 1999; Proga et al., 2000, 2008), or of radiative effects such as Compton heating and photoionization (Sazonov et al., 2005; Ciotti & Ostriker, 2007), or of radiation pressure Debuhr et al. (2010, 2011). Thermal feedback, heating by an unspecified mechanism has also been employed by many authors, *e.g.*, Springel et al. (2005a); Hopkins et al. (2005); Johansson et al. (2009b,a).

In this rapidly developing field of active galactic nucleus (AGN) feedback, it is natural for large scale numerical simulations to explore first the simplest schemes. Thus physical processes, which cannot all be included in the first three-dimensional hydrodynamic simulations, have been treated in a selective fashion. For example, in Springel et al. (2005a, here after "SdMH05"), among the first who reproduced the AGN feedback in a three-dimensional smoothed-particle hydrodynamics

(SPH) code, the feedback was assumed to be purely thermal. That is, the some fraction of the bolometric luminosity of accreting BHs is deposited as thermal energy to the neighboring gas particles via a mechanism that is not specified. The authors found that this thermal feedback treatment regulates and then terminates the further growth of the BH and expels gas from the central region in the galaxy in a quasar-driven outburst. This pioneering work, however, did not specify how the injected energy reaches the thermally heated gas particles. The conveyance of the energy is likely to be via either radiation or a wind, and in both cases momentum must be added with the thermal energy. If the energy is transferred via a wind with velocity $v_{\rm w}$, then the mass transfer may be significant and, since the ratio of momentum to energy scales as $1/v_{\rm w}$, the momentum transfer is correspondingly larger.

In a first attempt to study the relative importance of the different processes, utilizing one- and two-dimensional computations, it was found that momentum injection is the dominant mode of feedback (Ostriker et al., 2010, here after "OCCNP10"), because the very short cooling time of dense gas makes thermal input relatively inefficient. At the high densities of the central region of the galaxies, the cooling time of gas is sufficiently short in high resolution simulations, so that it cannot retain the injected thermal energy and efficiently convert it to kinetic energy. However, if the input to the surrounding fluid is via winds, then the return of mass and momentum to that fluid can be the dominant drivers which can reduce the accreted black hole mass by up to a factor of 100 (OCCNP10). Other recent work by Debuhr et al. (2010, 2011), emphasizing the momentum input from optically thick radiation fields ($\sim \tau L/c$ with $\tau \sim 10$) has also found the dramatic effects of momentum input.

Observationally, around 15–20% of bright quasars (Hewett & Foltz, 2003; Dai et al., 2008; Gibson et al., 2009) show outflows, where blue-shifted broad absorption lines (BAL) are attributed to subrelativistic ($\sim 10,000$ km/s) mass ejection. According to the fraction of quasars with BAL winds together with the assumption that all quasars have outflows, the BAL outflows are wide, covering at least 20% of the solid angle. The radiation driven winds from the detailed hydro simulation by Proga & Kallman (2004) cover $\sim \pi$ steradians, supporting this observational estimate. These outflows inject mass, momentum and energy into the surrounding gas and are

believed to be more efficient feedback agents of the host galaxies than relativistic jets, which drill through the ambient gas and put most of the energy into the intergalactic medium (IGM).

However, the effects of outflows to the host galaxies and larger cosmological structures are just beginning to be studied, because their mass ejection rates, energetics and sizes were largely undetermined. Adopting the recent measurements of mass ejection rates, and kinetic luminosities of the outflows from the absorption-line observations (Arav et al., 2008; Moe et al., 2009; Dunn et al., 2010), many authors introduced the kinetic AGN feedback in in adaptive mesh refinement (AMR) simulations (Omma et al., 2004; Dubois et al., 2009; Kim et al., 2011) and in SPH simulations (Nayakshin & Power, 2010; Debuhr et al., 2012).

It has been shown that the average spectrum of AGN has a strong secondary peak in the high energy X-rays ($\sim 50 - 100$ keV) which is the main contributor to the Compton and secondary metal line heating (Sazonov et al., 2004). Some recent studies using one- and two-dimensional simulations including Ciotti & Ostriker (2007); Novak et al. (2011) considered the effect of momentum input, heating and radiation pressure from the AGN radiation. The recent SPH work by Hambrick et al. (2011) found that X-ray feedback, the heating and radiation pressure associated with the X-ray radiation field emitted from the BH, is more effective at suppressing star formation and BH mass growth compared to the traditional thermal feedback approach. The X-ray heating was also found to be effective in AMR simulations (Kim et al., 2011), as it heats the surrounding interstellar medium, keeps it hot for an extended duration of time, and effectively self-regulates the growth of the BH.

In many previous numerical studies of galaxy formation and evolution that only can resolve hundreds of pc to kpc scales, the accretion of gas onto BHs at the centers of AGNs occurs on unresolved scales. The Bondi-Hoyle-Lyttleton formalism (Hoyle & Lyttleton, 1939; Bondi & Hoyle, 1944; Bondi, 1952) is commonly adopted, to obtain the BH mass accretion rate from the resolved larger scale properties of the ambient gas. This assumption has been made in studies of isolated galaxy and merging galaxies (*e.g.*, SdMH05, Younger et al., 2008; Johansson et al., 2009b) and as well in cosmological simulations (*e.g.*, Sijacki et al., 2007; Di Matteo et al., 2008; Sijacki et al., 2008; Booth & Schaye, 2009; Teyssier et al., 2011; Dubois et al., 2012).

However, in most of the cases treated to date, the SPH smoothing length or the numerical resolution of the respective code is larger than the Bondi radius, *i.e.*, the inner flow is numerically unresolved. The limitation of numerical and spatial resolution may introduce the unusual and unwanted effect — the neighboring gas particles around a BH at any distance from the BH can be accreted even though they are not gravitationally bound to the BH. This physically awkward treatment of the BH mass accretion may result in the very large growth of the central BH if we used the standard accretion algorithm without feedback. We will introduce a new treatment of gas particle accretion, 'Bondi radius criterion', which statistically limits the accretion of mass to the gas particles which are within the Bondi radius.

The purpose of the current chapter is to introduce (1) a modeling of AGN mechanical feedback via winds as observed in BAL systems that includes mass and momentum feedback, as well as thermal input, (2) the detailed treatment of radiative effects, *i.e.*, X-ray radiative feedback and (3) a modified BH accretion rate prescription using the Bondi radius criterion in the parallel TreeSPH-code GADGET. In this chapter, we restrict our exploration to the simulations of isolated disk galaxies and merging galaxies, in order to better understand the specific properties of the new treatments. We reserve the follow-up chapters for detailed analysis of merger simulations and cosmological simulations, to be compared with the results of observational papers.

This chapter is structured as follows. In Section 2 we describe the simulation code, and discuss the BH feedback and new BH accretion prescription. We present the results and comparisons between our new model and standard prescription in Section 3. We summarize and discuss our findings in Section 4.

# 2 Models

## 2.1 Numerical code

We perform the simulations using the parallel TreeSPH-code GADGET (Springel, 2005). The code employs the Lagrangian Smoothed Particle Hydrodynamics (SPH; see Monaghan, 1992) technique and solves the equations of motion for the collisionless dark matter and star particles

and gas. We include the radiative cooling for a primordial mixture of hydrogen and helium (Katz et al., 1996) and a spatially uniform time-independent local UV background (Haardt & Madau, 1996). The gas of the interstellar medium (ISM) is assumed to be a two-phase medium of hot and cold gas (McKee & Ostriker, 1977; Springel & Hernquist, 2003) and stars form from a cold component embedded in sufficiently dense gas, *i.e.*, $\rho > \rho_{\rm th}$ with the short-lived stars supplying an energy of $10^{51}$ erg to the surrounding gas per supernovae (SNe). This SN feedback heats the hot phase of the ISM and evaporates cold clouds, establishing a self-regulation cycle for star formation. SN-driven galactic winds are not included in this study.

We include all the basic aspects of the model for black hole (BH) accretion and feedback adopted in SdMH05, Springel et al. (2005a); Johansson et al. (2009b), and implement the momentum and mass feedback.

## 2.2 Black hole feedback model

In the widely adopted SdMH05 model, the numerically unresolved accretion onto the BH is related to the large-scale resolved gas distribution using a Bondi-Hoyle-Lyttleton parameterization (Hoyle & Lyttleton, 1939; Bondi & Hoyle, 1944; Bondi, 1952). In very high resolution treatments where the Bondi radius ($R_B \sim 2GM_{\rm BH}/(c_s^2 + v^2)^{1/2}$) is resolved such as Ciotti et al. (2010); Novak et al. (2011); Barai et al. (2011), there is no need to specify the accretion rate as the hydro code with an appropriate inner boundary condition will correctly calculate the accretion rates. The accretion rate onto the BH in unresolved flows is estimated as

$$\dot{M}_{\rm B} = \frac{4\pi\alpha G^2 M_{\rm BH}^2 \rho}{(c_{\rm s}^2 + v^2)^{3/2}}, \tag{2.1}$$

where $\rho$ and $c_{\rm s}$ are the density and sound speed of the surrounding gas, respectively. $v$ is the velocity of the BH relative to the surrounding gas. Here $\alpha$ is a dimensionless parameter setting the efficiency of the accretion and it is conventionally set to be $\alpha = 100$ in SPH simulations on the grounds that the low spatial resolution currently available would otherwise limit the accretion rate to lower than the true value. Adopting $\alpha = 100$ gives reasonable results for the low resolution

simulations discussed in SdMH05, and Johansson et al. (2009b), but in general $\alpha$ is resolution dependent. We adopt different values of $\alpha$ for the different resolutions, and details will be presented later in subsection 2.4. Note that Equation 3.1 describes the accretion onto a point mass surrounded by adiabatic ($\gamma = 5/3$) gas with properties $\rho$, $c$, and $v$ (in Equation 3.1) far away from the BH ($r \to \infty$). Usually it is also assumed that the maximum accretion is limited to the Eddington rate given by

$$\dot{M}_{\rm edd} \equiv \frac{4\pi G M_{\rm BH} m_{\rm p}}{\epsilon_{\rm r} \sigma_{\rm T} c}. \tag{2.2}$$

Here $m_{\rm p}$ is the proton mass, $\sigma_{\rm T}$ is the Thomson cross-section and $\epsilon_{\rm r}$ is the radiative efficiency assumed to be a fixed value of 0.1 adopted from the mean value for radiatively efficient Shakura & Sunyaev (1973) accretion onto a Schwarzschild BH. This value is also supported by the global mass-energy relation pointed out by Soltan (1982) and Yu & Tremaine (2002). The accretion rate is then $\dot{M}_{\rm inf} = \min(\dot{\rm M}_{\rm B}, \dot{\rm M}_{\rm edd})$. The BHs are represented by collisionless 'sink' particles, which feel only gravitational forces. The properties, including density, temperature and the bulk velocity of the local gas around the BH, which then define the accretion rate, are estimated in a similar fashion to normal SPH particles.

Technically, the actual accretion of gas particles onto the BH particle is implemented using a stochastic approach (SdMH05). For each gas particle $j$ around a BH, the probability of being absorbed by the BH is calculated as

$$p_j = \frac{w_j \dot{M}_{\rm inf} \Delta t}{\rho}, \tag{2.3}$$

where $w_j$ is the kernel weight of the gas particle relative to the BH, $\dot{M}_{\rm inf}$ is the BH accretion rate, $\Delta t$ is the time step. The gas density $\rho$ is measured at the position of the BH as,

$$\rho = \sum_{i=1}^{N} m_i w_i, \tag{2.4}$$

where $m_i$ denotes the gas particle mass, and N is the number of neighboring particles to the BH. From Equation 2.3 and 2.4, we see that the probability of the $j$th particle being accreted in time interval $\Delta t$ is close to $p_j = \dot{M}_{\rm inf} \Delta t / m_{\rm gas}$, but influenced by the smoothing kernel of gas particle

near the BH. The gas particle is swallowed by the BH when the probability $p_j$ is larger than the generated random number uniformly distributed in the interval [0,1].

### *Thermal Feedback*

In previous GADGET based studies, the feedback energy from the black hole $E_{\rm feed}$ has typically been assumed to be some fraction $\epsilon_{\rm f}$ of the radiated luminosity $L_{\rm r}$ and couples thermally and isotropically to the surrounding gas as,

$$\dot{E}_{\rm feed} = \epsilon_f L_{\rm r} = \epsilon_f \epsilon_{\rm r} \dot{M}_{\rm inf} c^2. \tag{2.5}$$

Many authors (*e.g.*, SdMH05) adopt a fixed value of $\epsilon_f = 0.05$ so that $\epsilon_{\rm w} = \epsilon_f \epsilon_{\rm r} = 5 \times 10^{-3}$, *i.e.*, 0.5 percent of the accreted rest mass energy in total is available as thermal energy feedback. Utilizing this value for thermal feedback and adopting $\alpha = 100$, the normalization of the $M_{\rm BH} - \sigma$ was recovered by Di Matteo et al. (2005) in disk mergers simulations having a spatial resolution of $\epsilon_{gas} = 0.1h^{-1}$ kpc and a mass resolution of $M_{\rm gas} \sim 6 \times 10^5 M_\odot$.

The corresponding feedback energy is distributed as thermal energy to the surrounding $\sim 64$ gas particles weighted by the SPH kernel. Note that the results may depend on the details of the numerical implementation. If $\sim 128$ particles are used of a given mass rather than $\sim 64$, the sound speed $c_{\rm s}^2$ would have been lower with corresponding increase of the accretion rate $\dot{M}_{\rm B}$ in Equation 3.1. What matters is the mass of the material into which the thermal energy is dumped. Thus, if the mass per particle were halved and the particle number was doubled the results would not change. In this standard approach, neither mass nor momentum is added to the ambient fluid by the black hole and all energy that is added is via thermal energy.

### *Momentum Feedback*

Accreting BHs are observed to emit broad-line winds that convey mass, energy, and momentum into the surrounding gas (de Kool et al., 2001; Moe et al., 2009; Dunn et al., 2010) and our goal is

to include these observed flows in our numerical treatment. To implement mechanical momentum and mass feedback, we define the inflowing and outflowing mass rates to be ($\dot{M}_{\rm inf}$, $\dot{M}_{\rm outf}$), and we use the following simple equations based on the conservation of mass, energy and momentum (*cf.* OCCNP10):

$$\dot{M}_{\rm acc} = \dot{M}_{\rm inf} - \dot{M}_{\rm outf}, \tag{2.6}$$

where $\dot{M}_{\rm acc}$ is the mass rate actually accreted onto the BH. We define the kinetic energy rate of the outflow $\dot{E}_{\rm w}$ as,

$$\begin{aligned} \dot{E}_{\rm w} &\equiv \epsilon_{\rm w}\dot{M}_{\rm acc}c^2, & (2.7a)\\ &= \frac{1}{2}\dot{M}_{\rm outf}v_{\rm w}^2, & (2.7b) \end{aligned}$$

$$\dot{p} = \dot{M}_{\rm outf}v_{\rm w}, \tag{2.8}$$

where we have oversimplified matters by allowing only one wind velocity, $v_{\rm w}$, when in fact Equation 4.5b requires $\langle v_{\rm w}^2\rangle$ and Equation 4.4 requires $\langle v_{\rm w}\rangle$ and $\epsilon_{\rm w}$ denotes the feedback efficiency, *i.e.*, the wind efficiency in the momentum feedback model. Now, defining

$$\psi \equiv 2\epsilon_{\rm w}c^2/v_{\rm w}^2 = \dot{M}_{\rm outf}/\dot{M}_{\rm acc}, \tag{2.9}$$

we have, as solutions to Equations 4.3 - 4.4,

$$\begin{aligned} \dot{M}_{\rm acc} &= \dot{M}_{\rm inf}\frac{1}{1+\psi}, & (2.10a)\\ \dot{M}_{\rm outf} &= \dot{M}_{\rm inf}\frac{\psi}{1+\psi}, & (2.10b)\\ \dot{E}_{\rm w} &= \epsilon_{\rm w}c^2\dot{M}_{\rm inf}\frac{1}{1+\psi}, & (2.10c)\\ \dot{p} &= \dot{M}_{\rm inf}v_{\rm w}\frac{\psi}{1+\psi}. & (2.10d) \end{aligned}$$

As we see from equations (2.10a,b), there is an important dimensionless quantity $\psi \equiv \dot{M}_{\rm outf}/\dot{M}_{\rm acc}$. In typical treatments of AGN feedback, $\psi$ is assumed to be 0 in equations (2.10) implicitly assuming $v_{\rm w} \to \infty$, and so $\dot{M}_{\rm outf}$ and $\dot{p}$ are neglected. Thus, the two terms $\dot{E}_{\rm w}$ and $\dot{M}_{\rm acc}$ may be overestimated, and $\dot{p}$, the momentum input to the surrounding fluid is neglected. For example, if we adopt for the efficiency of generating mechanical energy the value $\epsilon_{\rm w} = \epsilon_f \epsilon_{\rm r} = 5 \times 10^{-3}$, as adopted by Springel (2005) and other authors, and we take $v_{\rm w} = 10,000$ km/s ($v_{\rm w,10}$) (Crenshaw et al., 2003; Moe et al., 2009), then we have $\psi = 9\ v_{\rm w,10}^{-2}$ and all of the neglected effects may in fact be dominant; 90 percent, $(\psi/(1+\psi))$ of the inflowing mass may be ejected in a disc broad absorption line (BAL) wind and the mass and momentum input deposited in the ambient gas may dominate over the energy input.

To implement the actual output of mass, momentum and energy, we modify the stochastic approach applied for the gas particle accretion on the BH shown in Equation 2.3. We first calculate a probability of being attracted into the central zone by the BH for each gas particle nearby using Equation 2.3 and determine its fate by generating a random number $x_j$ in the interval [0,1]. For $x_j < p_j$, the gas particle is taken to be part of the inflow onto the BH. We then draw an independent random number $y_j$ uniformly distributed in the interval [0,1] and compare it with $1/(1+\psi)$, the probability of being actually absorbed by the BH. For $y_j < 1/(1+\psi)$, the gas particle is accreted onto the BH. For $y_j > 1/(1+\psi)$, the gas particle is ejected with its wind velocity $v_{\rm w}$ and momentum.

We fix the wind velocity $v_{\rm w}$ to 10,000 km/s ($v_{\rm w,10}$) (Crenshaw et al., 2003; Moe et al., 2009) corresponding to a typical broad line wind. Together with our choice of $\epsilon_{\rm w} = 5 \times 10^{-4}$ (Note that our energy coupling parameter $\epsilon_{\rm w}$ is 10 times smaller than the value used in other GADGET-2-based simulations), we have $\psi = 0.9$. That is, essentially one of two particles inflowing to the BH is actually accreted by it, the other is driven out as part of the broad absorption line wind.

We emit a particle radially from the BH in the specified direction. We set the direction of wind to be parallel or anti-parallel to the direction of angular momentum ($\vec{r} \times \vec{v}$) of each gas particle, making it to be essentially perpendicular to the disc. The outflow is stronger perpendicular to

disk (Proga & Kallman, 2004) as the feedback is relatively inefficient in the accreting disc of BH which supplies a continuous fuel to the BH via inflow. In addition, the massive and geometrically thick nature of the molecular torus (*e.g.*, Krolik & Begelman, 1988; Tacconi et al., 1994) may restrict the outflow to the direction essentially parallel to the disk angular momentum vector.

AGN outflows can collide with and shock ambient gas, generating a momentum-driven flow. To mimic this phenomenon, we let the emitted wind particle share its momentum with the neighboring gas particles. With this 'momentum share' treatment, the two nearest neighboring gas particles are expelled together with the wind particle. They have the same velocity increment, $\Delta v_{\rm w} \sim 10,000/3$ km/s, conserving the momentum. Sharing momentum with other particles via inelastic collisions, however, decreases the total kinetic energy increment (Equation 4.5b) while preserving momentum. We deposit the residual energy into these three particles in thermal form so that total energy is conserved. Note that the wind particles can reach very high temperatures. The analysis of the number of momentum sharing particles will be discussed in the later sections.

Momentum sharing has two technical advantages. In general, high velocity particles will drive shocks. Similarly to SN remnants, the solution will approach a Sedov-solution. However, with coarse mass and time resolution and having momentum share starts the cascade of transforming the $\sim 100\%$ kinetic energy flux of the wind outflow to the $\sim 25\%$ kinetic energy flux of the Sedov solution with twice the number of particles, a lower initial fraction of kinetic energy; and it makes the approach to the Sedov solution faster. Thus it makes us less sensitive to the problem of not having enough particles to correctly represent a hydrodynamic outflow. It also has computational advantages with regard to the time stepping. The standard Courant time step calculation implemented in the public release of GADGET might not guarantee fine enough time-stepping for strong explosion problems (Springel, 2010), and requires additional time-step limiter implementation (Saitoh & Makino, 2009; Durier & Dalla Vecchia, 2012). In momentum sharing, reducing the velocity of the wind by a factor of 3, while maintaining the same momentum flux, reduces the need for short and expensive time steps by the same factor, and our experiments have shown that if we perform solutions with high enough time and mass resolutions there is almost no

difference between the two models. However, there is a great saving computationally in doing a momentum sharing when we are at low resolution.

In this approach mass, energy, and momentum are transferred to the ambient gas during AGN feedback and in addition to the usual efficiency parameter $\epsilon_{\rm w}$, we must introduce a parameter $\psi$, (Equation 4.6), the ratio of the outflow mass flux to the accreted mass flux, which is fixed by $\epsilon_{\rm w}$ and the wind velocity $v_{\rm w}$.

### *X-ray Feedback*

We also consider the radiative feedback from the electromagnetic-energy component of X-ray radiation from the BH. We first calculate the total radiation emitted from the location of the BH particle as,

$$L_r = \epsilon_r \dot{M}_{\rm BH} c^2 \tag{2.11}$$

where the radiative efficiency $\epsilon_r = 0.1$ is adopted in all simulations (Ciotti & Ostriker, 2007; Ciotti et al., 2009; Novak et al., 2011). This luminosity is converted to a luminosity flux at the position of each particle by $F_r = L_r/4\pi r^2$, where $r$ denotes the distance of the particle from the BH particle. We convert the flux to the net volume heating rate $\dot{E}$ by using the Sazonov et al. (2005) formulae, which describe the net heating rate per unit volume of a cosmic plasma in photoionization equilibrium with a radiation field characterized by the average quasar spectral energy distribution, as in Ciotti et al. (2010); Novak et al. (2011). We take into account Compton heating and photoionization heating as summarized below. The volume heating rate $\dot{E}$ in cgs units is given as:

$$\dot{E} = n^2(S_1 + S_2), \tag{2.12}$$

where $n$ is the proton density (in number). The Compton heating term $S_1$ is

$$S_1 = 4.1 \times 10^{-35}(1.9 \times 10^7 - T)\,\xi, \tag{2.13}$$

where the ionization parameter $\xi$ is defined as

$$\xi \equiv \frac{L_r}{n(r)r^2}. \tag{2.14}$$

The sum of photoionization heating is given as

$$S_2 = 10^{-23} \frac{a\,(\xi/\xi_0)^b}{1 + (\xi/\xi_0)^b}, \tag{2.15}$$

where

$$a = \frac{1.7 \times 10^4}{T^{0.7}}, \tag{2.16}$$

$$b = 1.1 - \frac{1.1}{e^{T/1.8\,10^5}} + \frac{4 \times 10^{15}}{T^4}, \tag{2.17}$$

and finally

$$\begin{aligned} \xi_0 \;=\; & \frac{1}{1.5/\sqrt{T} + 1.5 \times 10^{12}/\sqrt{T^5}} + \\ & \frac{4 \times 10^{10}}{T^2}\left[1 + \frac{80}{e^{(T-10^4)/1.5\,10^3}}\right]. \end{aligned} \tag{2.18}$$

A speed-of-light delay in propagation from the BH is not included, since the effects of the delay should be small because of the small simulation scale ($\lesssim 50$ kpc). We neither include radiative transfer nor optical depth effects for the hard X-ray radiation considered here.

However, we do include the electromagnetic-momentum – the radiation pressure from the X-ray flux from the BH as in Debuhr et al. (2010, 2011). We model the radiation pressure by applying a total momentum per unit time of

$$\dot{p} = \dot{E}/c, \tag{2.19}$$

away from the BH particle to each gas particle where $\dot{E}$ is the energy absorbed by the particle given the Sazonov et al. (2005) prescriptions. Here we neglect the effect of dust since the ISM generally has a low optical depth to hard X-rays. Hambrick et al. (2011) and Kim et al. (2011)

recently studied the effects of X-ray radiation on the properties of massive elliptical galaxies. They found that X-ray feedback is more effective at suppressing star formation and BH mass growth compared to the traditional thermal feedback model.

*Eddington Force*

In the previous studies, the maximum accretion has been limited to the Eddington rate (Equation 3.2) as shown in Section 2.2. Instead of manually limiting the mass accretion, we actually compute the Eddington force (EF) acting on the surrounding gas particles, directed radially away from the black hole. We first calculate the luminosity as in Equation 2.11, and the flux at the position of the each particle by $F_r = L_r/4\pi r^2$ where the $r$ denotes the distance of the particle from the BH particle. Then, the total momentum change per unit time by the Eddington force acting on the gas particles radially away from the black hole particle is given as,

$$\dot{p} = \frac{F_r N_e \sigma_T}{c}, \tag{2.20}$$

where $N_e$ denotes the number of electrons associated with each gas particle and $\sigma_T$ is the Thomson cross-section for the electron. When the black hole has vigorous mass accretion bursts, *i.e.*, above the Eddington mass accretion limit, the strong radiation pressure by the black hole pushes the gas particles away, resulting in a lower density near the black hole particle, which leads to the lower mass accretion rate. Since the Thompson cross-section is independent of frequency ($h\nu \ll m_e c^2$), no radiative transfer treatment is required; we assume that absorbed UV radiation is re-radiated as IR radiation.

## 2.3 New black hole accretion model

*Bondi Radius Criterion*

The key to understanding the accretion process lies in correctly modeling the behavior of the accreting gas once it falls within the gravitational influence of the black hole, the Bondi radius,

$r_{\rm Bondi}$, defined as

$$r_{\rm Bondi} \equiv \frac{2GM_{\rm BH}}{{v_i}^2}, \tag{2.21}$$

where ${v_i}^2 = c^2 + {v_{\rm rel}}^2$, $c$ and $v_{\rm rel}$ denote the sound speed and the relative velocity to the black hole of the gas respectively. The Bondi radius divides the flow into two distinct regions. Far outside of $r_{\rm Bondi}$, gas is hardly aware of the existence of the black hole, and the flow is subsonic. On the other hand, inside the Bondi radius, gas has negative total energy and essentially plunges at free-fall. The Bondi radius in the spherical case being the place where the Mach number of the flow is unity. We note that heating that occurs within the Bondi radius cannot, by definition, affect the accretion rate since information cannot propagate upstream in a supersonic flow.

Applying the Bondi-Hoyle-Lyttleton formalism (Equation 3.1) to the black hole mass accretion rate assumes that the accretion onto the black hole is commensurate with the accretion rate through the Bondi radius. In cases where the SPH smoothing length is greater than the Bondi radius, *i.e.*, the inner flow is numerically unresolved, unusual effects can occur. To see what would happen if we used the standard accretion algorithm without feedback, we have made some artificial tests without any feedback mechanisms. We obtain a very large growth of the black hole with $M_{\rm BH} \sim 10^{10} M_\odot$. The neighboring gas particles around a BH at any distance from the BH are accreted, even for particles which are not gravitationally bound to the BH.

To avoid any unphysical accretion from outside of the Bondi radius, we limit the accretion of mass to the gas particles statistically within the Bondi radius. With this Bondi radius criterion, gas particles can only be accreted when $r_i < r_{\rm Bondi}$, where $r_i$ is the distance of the gas particle from the black hole particle. When the mass of the BH is small, we cannot resolve the Bondi radius, *i.e.*, the smallest resolvable length scale of our simulations, the gravitational softening length, is of a few tens of pc, whereas the Bondi radius is just a few pc when the BH mass is around $10^{5-6} M_\odot$ ($r_{\rm Bondi}/{\rm pc} = 3.4\ M_{\rm BH,6}/v_{i,50}^2$ where $M_{\rm BH,6} = 10^6 M_\odot$ and $v_{i,50}$=50 km/s). In this case, we set the Bondi radius to be the smallest resolved scale, *i.e.*, the gravitational softening length of the gas particles.

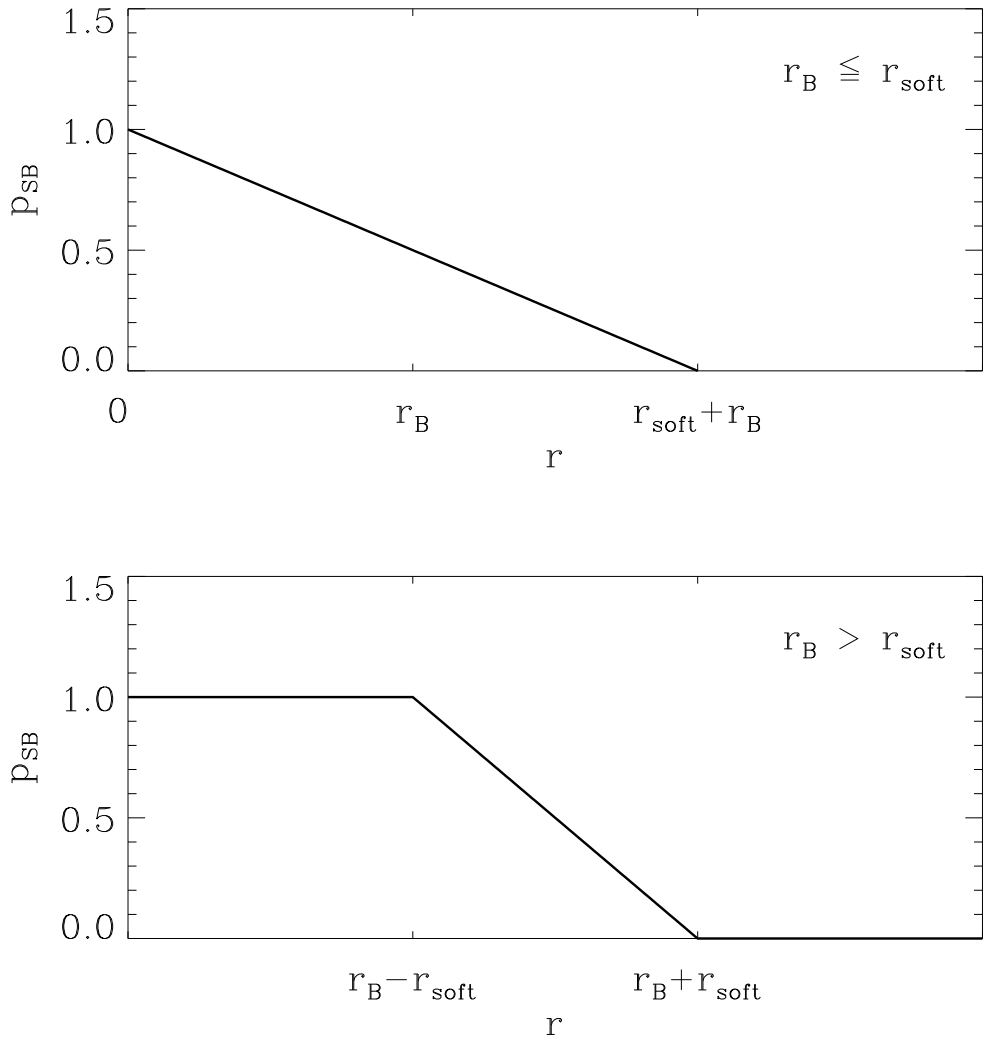



Figure 2.1: The soft Bondi probability of being absorbed by BH as a function of the particle distance $r$. The probability for the case when the Bondi radius $r_{\rm Bondi}$ is equal to the softening length $r_{\rm soft}$ shown in the upper panel, and one for the case when $r_{\rm Bondi}$ is larger than $r_{\rm soft}$ is shown below.

Since the gas mass distribution is smoothed with a kernel size $h_i$, we apply what we term "a soft cut of Bondi radius criterion". We allow the full accretion rate, only when the distance of the gas particle from the black hole particles $r_i$ is smaller than $r_{\rm Bondi} + r_{\rm soft}$. The gravitational softening length $r_{\rm soft}$, which avoids numerical singularities in the integral representation of the potential, is the smallest resolvable length scale and serves as the minimum bound to the smoothing length $h_i$. The soft Bondi probability $p_{\rm SB}$ as a function of the particle distance from the BH, for two cases of $r_B \leq r_{\rm soft}$ and $r_B > r_{\rm soft}$, is shown in Figure 2.1. When the soft Bondi limit (SB) is included, we reduce the probability of being absorbed by the BH for each gas particle (given as Equation 2.3) used in the original code by the soft Bondi probability $p_{\rm SB}$, *i.e.*, the final probability will be given as $p_{\rm final} = p_j \times p_{\rm SB}$. This treatment essentially limits the mass accretion only to the gas particles statistically within the Bondi radius.

*Free-fall modification of accretion rate*

In the standard version of the code the actual accretion of the gas particles is determined by the probability, which is only a function of the SPH smoothing kernel. We have altered this to include a dependence on the time that it would take for the particle to be accreted allowing an extra factor of

$$p_{j,\rm ff} = \frac{\frac{1}{\tau_j}}{\frac{1}{N_{\rm sph}} \sum_{j=1}^{N_{\rm sph}} \frac{1}{\tau_j}}, \tag{2.22}$$

where $\tau_j = r_j/(c_{\rm s}^2 + v^2)^{1/2}$ is the free fall time and $N_{\rm sph}$ denotes the typical number of smoothing neighboring gas particles of the BH. We modify the probabilities (Equation 2.3) to make them proportional to $p_{j,\rm ff}$, *i.e.*, we make it more likely that nearby particles will be accreted in a given time step than more distant ones. When the free-fall (FF) modification is included, the final probabilities of the particles to be accreted by BH is given as $p_{\rm final} = p_j \times p_{j,\rm ff}$. where $p_j$ denotes a probability of being absorbed by BH used in the original code (Equation 2.3).

*Alternative averaging in the mass accretion calculation*

In the original implementation of Springel (2005), the BH mass accretion is calculated based on the physical quantities such as density, sound speed, and relative velocity of the surrounding gas of the BH as shown in Eq. 3.1. These physical quantities for the BH particle are calculated from the $\sim 64$ neighboring gas particles using the SPH kernel. We can rewrite the Eq. 3.1 as,

$$\dot{M}_{\rm B} = \frac{4\pi\alpha G^2 M_{\rm BH}^2 \langle\rho\rangle}{(\langle c_{\rm s}\rangle^2 + \langle v\rangle^2)^{3/2}}, \tag{2.23}$$

where angle brackets denote the averaging over the neighboring particles using SPH kernel. This method can be unstable to the number of SPH neighboring particles chosen and it separately averages quantities in the numerator and the denominator of Eq. 2.23. Suppose we made a run which used the 128 nearest particles instead of 64 nearest particles. It would have a different evolution, the soundspeed would be lower and so would the density. As noted earlier it is not the number of particles, per se that matters. If we halved the mass resolution and then moved to 32 particles we would keep the total mass into which the feedback energy was deposited a constant. We have performed this experiment and find that results are essentially unchanged. However, of course putting the energy into increasingly more mass would lower the feedback induced increase in $c_{\rm s}^2$ and change the Bondi rate after the use of Equation 3.1.

Our new averaging method for the calculation of the BH mass accretion "Alternative Averaging (AA)" does the calculation in both time and space on an individual particle basis and then averages the results over the nearest 64 particles in order to reduce the dependency on the number of SPH particles. With AA, we can rewrite the Eq. 3.1 as,

$$\dot{M}_{\rm B,AA} = \left\langle \frac{4\pi\alpha G^2 M_{\rm BH}^2 \rho}{(c_{\rm s}^2 + v^2)^{3/2}} \right\rangle, \tag{2.24}$$

where angle brackets denote the averaging over the SPH kernel. This method of performing the averaging is convergent because the added outer particles add progressively less and less.

*Fiducial BH mass accretion model*

In the fiducial model, we include all of modifications we described for the BH mass accretion model, *i.e.*, Soft Bondi radius criterion (SB), Free-fall modification (FF), and Alternative Averaging (AA). We first calculate the BH mass accretion rate using Eq. 4.1 as shown above, and for the actual accretion of the gas particles onto the BH particle, we calculate a probability of being absorbed for each gas particle $j$ as

$$p_{j,\mathrm{final}} = p_j \times p_{j,\mathrm{SB}} \times p_{j,\mathrm{ff}}. \tag{2.25}$$

We test our modified BH accretion model against the analytic Bondi solution in an idealized homogenous environment. As demonstrated in the Appendix we recover the Bondi solution.

## 2.4 Initial condition

The disk galaxies used in this study are set up in dynamical equilibrium and consist of a dark matter halo, a rotationally supported exponential disc of gas and stars, and a central bulge. The details of the model construction are summarized in SdMH05. We test and study the stability of the constructed galaxy feedback models with a representative sample of our disk galaxy models in isolation with $v_{\mathrm{vir}} = 160$ km s$^{-1}$, and $r_{\mathrm{vir}} = 160\ h^{-1}$ kpc corresponding to a virial mass of $M_{\mathrm{vir}} = 9.53 \times 10^{11}\ h^{-1} M_{\odot}$. The dimensionless Hubble parameter is $h = 0.71$ such that the present-day Hubble parameter is $H_0 = 71$ km s$^{-1}$ Mpc$^{-1}$. The Hernquist (1990) profile dark matter halos is constructed with the concentration parameter $c = 9$ of the corresponding Navarro-Frenk-White (NRW) halo (Navarro et al., 1997). The dark matter halo is then populated with exponential disks with a baryonic mass fraction of $m_d = 0.041$, so that a total disk mass $M_d = m_d M_{vir}$ with a fractional gas content of $f_{gas} = 0.2$ with the rest being stars.

To study the effects of numerical resolution, we use 4 models with different mass and spatial resolutions but with the same initial set-up. The resolution details, including the number of particles, particle mass and corresponding gravitational softening lengths are given in Table 1.

The dimensionless accretion parameter in Equation 3.1 was set to $\alpha = 100$ in the previous studies (SdMH05, Johansson et al., 2009b), which correspond to our low resolution model. This value is quite a bit higher than the theoretical value of $\alpha \sim 1$. This discrepancy is due to the numerical resolution limits, that is, the gas density and sound speed at the location of the black hole are estimated over the large-scale, resulting in artificially low densities and high sound speed. The higher value of $\alpha$ has been adopted empirically to correct for this resolution effect. For the model with the higher numerical resolution, we adopt the smaller value of the dimensionless accretion parameter that can result in the similar scale of early accretion history of low resolution model with $\alpha = 100$. We run a series of simulations without any feedback prescription with the different values of $\alpha$, and adopt the $\alpha$ value that best reproduces the early accretion history of the low resolution run with $\alpha = 100$. We turn off all the BH feedback to remove the resolution dependency of the feedback prescription. The adopted values of $\alpha$ for each resolution are shown in Table 1.

We summarize the properties of the models in Table 2. For reference, we first list the thermal feedback model "T", with the standard BH mass accretion and feedback model described in SdMH05. Note that model properties of standard model "T" in this chapter are different from those of SdMH05, as we adopt "Very High" resolution as a standard resolution in this chapter, and the energy coupling efficiency $\epsilon_{\rm w} = 5 \times 10^{-4}$ which is 10 times smaller than the value adopted in SdMH05. We name our best proposed model with all the modifications that we have described "Fiducial". To isolate and compare the effects of each feedback model or modification, we include some simulations with one modification missing. We also include the "No Feedback" model: with no BH feedback in any form. Details of each model are shown in Table 2.

# 3 Results

## 3.1 Comparison of the different feedback mechanisms

We first examine the effects of various feedback mechanisms on the evolution of the black holes and galaxies. Figure 2.2 shows the global star formation rate, the accretion rate onto the black hole, and the evolution of the black hole mass for the two different feedback models, the classical,

Table 2.1: Summary of the numerical resolution

| Model | DM particles | disk particles | $m_{\rm DM}$ $(h^{-1}M_\odot)$ | $m_{\rm bar}$ $(h^{-1}M_\odot)$ | ${\epsilon_{\rm bar}}^a$ | ${\epsilon_{\rm DM}}^a$ | $\alpha^b$ |
|---|---|---|---|---|---|---|---|
| Low$^c$ | 30,000 | 40,000 | $2.96 \times 10^7$ | $3.91 \times 10^5$ | 0.1 | 0.8 | 100 |
| High | 400,000 | 300,000 | $2.25 \times 10^6$ | $1.30 \times 10^5$ | 0.02 | 0.083 | 35 |
| Very High | 800,000 | 600,000 | $1.13 \times 10^6$ | $6.50 \times 10^4$ | 0.016 | 0.066 | 32.5 |
| Ultra High | 1,600,000 | 1,200,000 | $5.62 \times 10^5$ | $3.25 \times 10^4$ | 0.013 | 0.052 | 30 |

[a] Gravitational softening lengths in $h^{-1}$ kpc.
[b] Dimensionless accretion parameter in Equation 3.1.
[c] Numerical resolution used in Springel et al. (2005b) corresponds to our low resolution model.

Table 2.2: Summary of Model Properties

| | | Feedback | | | | | | | | log | log | log | log | |
|---|---|---|---|---|---|---|---|---|---|---|---|---|---|---|
| | Model | T/M | X-ray | X-ray RP | FF | AA | SB | EF | NEL | $\Delta M_{\rm BH}$ | $\Delta M_{\rm wind}$ | ${l_{\rm BH}^{\rm eff}}^a$ | ${L_{\rm wind}}^b$ | ${v_{\rm wind}}^c$ |
| (1) | (2) | (3) | (4) | (5) | (6) | (7) | (8) | (9) | (10) | (11) | (12) | (13) | (14) | (15) |
| 1 | Thermal[d] | Thermal | | | | | | | | 7.47 | 8.92 | -2.80 | 36.99 | 53.17 |
| 2 | Fiducial[e] | Momentum | √ | √ | √ | √ | √ | √ | √ | 7.38 | 8.24 | -2.66 | 40.72 | 1828.1 |
| 3 | Fiducial w/o XRP | Momentum | | | √ | √ | √ | √ | √ | 7.96 | 9.22 | -2.22 | 41.37 | 1287.9 |
| 4 | Fiducial w/o EF | Momentum | √ | √ | √ | √ | √ | | √ | 7.41 | 8.56 | -2.51 | 41.07 | 1727.2 |
| 5 | Fiducial w/o SB | Momentum | √ | √ | √ | √ | | √ | √ | 7.54 | 8.71 | -2.37 | 41.08 | 1743.9 |
| 6 | N | No Feedback | | | | | | | | 9.81 | - | -3.86 | - | - |
| 7 | N-SB | No Feedback | | | | | √ | | | 8.89 | - | -2.38 | - | - |

**Note.** Model names indicate the activated physics (symbol √) in the simulations as detailed in Column 3-10. For example, in Model 'Thermal' only thermal energy feedback is allowed, while in Model 'N-SB', no feedback is included, with the soft bondi (SB) treatment.[ADD:$M_*$]

[a] $l_{\rm BH}^{\rm eff} \equiv L_{\rm BH,opt}^{\rm eff}/L_{\rm Edd}$ where $L_{\rm BH,opt}^{\rm eff}$ is the BH luminosity in the optical band after absorption, *i.e.*, as it will be seen from infinity. The mean Eddington rates for last 1 Gyr are listed.
[b] The mechanical luminosity of the wind based on the wind mass rate and wind velocity measured at 5 kpc from BH for last $\sim 1$ Gyr. $L_{\rm wind} \equiv \dot{M}_{\rm wind} v_{\rm wind}^2/2$.
[c] Gas wind velocity at 5 pc from BH in km/sec.
[d] This model corresponds to the purely thermal feedback model discussed in SdMH05 (Springel et al., 2005b).
[e] Our best proposed "Fiducial" model.

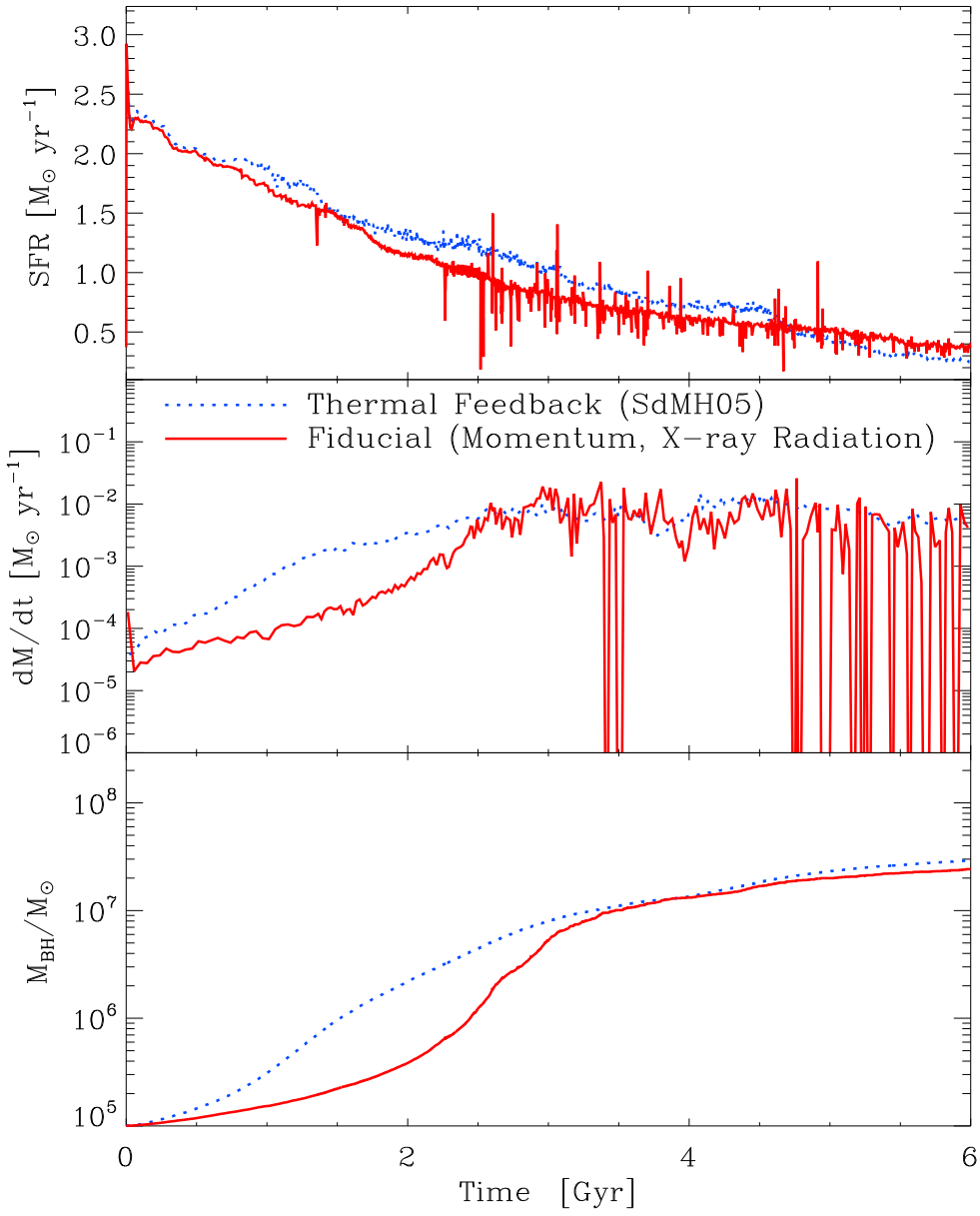



Figure 2.2: Comparison of the feedback models: classical thermal feedback (blue), and our best proposed "Fiducial" model which has momentum mechanical feedback with the X-ray heating and radiation pressure (red). Evolution of the global star formation rate (*top*), the accretion rate onto the black hole (*middle*) and the evolution of the black hole mass (*bottom*) for an isolated gas-rich disk galaxy. Note that both the star formation rate and the black hole growth are essentially similar in the new momentum driven treatment and the previous thermal feedback model. However, the degree of fluctuation in the mass accretion rate is greater in the momentum feedback model.

thermal feedback (*e.g.*, SdMH05), and our best proposed "Fiducial" model which has mechanical feedback with the X-ray heating and radiation pressure. Note that both models adopt the same feedback energy coupling efficiency $\epsilon_{\rm w} = 5 \times 10^{-4}$, which is 10 times smaller than the value adopted in SdMH05. A seed black hole starts at rest in the center with mass of $M_{\rm BH} = 10^5 M_{\odot}$ in all models, and grows due to gas accretion during the simulation. Note that the growth of black hole is essentially the same in the two models. Thus the primary results of SdMH05 and Di Matteo et al. (2005) with respect to the growth of central black holes during galaxy mergers are not substantially altered by the changes that we have introduced. Also, overall star formation rates of the two models are similar. However, the new model with mechanical feedback has more episodic star formation as in the mass accretion rate. Accretion rates and radiation output are much more variable in the new treatment with episodes of high accretion now reaching $L_{\rm BH}/L_{\rm Edd} \geq 0.1$. The mechanical feedback model spends a large fraction of time at relatively low Eddington accretion rate, coinciding with the observed broad-line active galaxies in the local universe (Greene & Ho, 2007; Ho, 2009; Kauffmann & Heckman, 2009).

Moreover, the two models have quite different wind properties. In the mechanical feedback model, wind particles are ejected with the instantaneous disk wind velocity of $v_{\rm w} \sim 3000$ km/s (OCCNP10), while the heating from AGN feedback energy drives slow and hot outflows from galaxies in the thermal feedback model. The existence of a weak wind perpendicular to the plane of the disk in the vicinity of the BH was shown in SdMH05.

In order to compare the wind properties, we first measure the total outflow wind mass throughout the simulation by summing up the mass of the gas particles which pass through the plane $|z| = 5$ kpc, above and below the disc midplane. Then, we measure the velocity of the particle at each time step and calculate the corresponding mechanical luminosity as $L_{\rm wind} \equiv \dot{M}_{\rm wind} v_{\rm wind}^2/2$, *i.e.*, the kinetic energy carried away by the outflowing winds. Temporal evolution of the wind properties (*i.e.*, outflow rate, wind velocity and mechanical luminosity) of two representative models of thermal feedback (SdMH05) and the fiducial model are shown in Figure 2.3. Once the black holes reach similar masses, after about 3 Gyrs, the thermal feedback model develops a wind with about a factor of 10 higher outflow rate, but the velocity of the wind

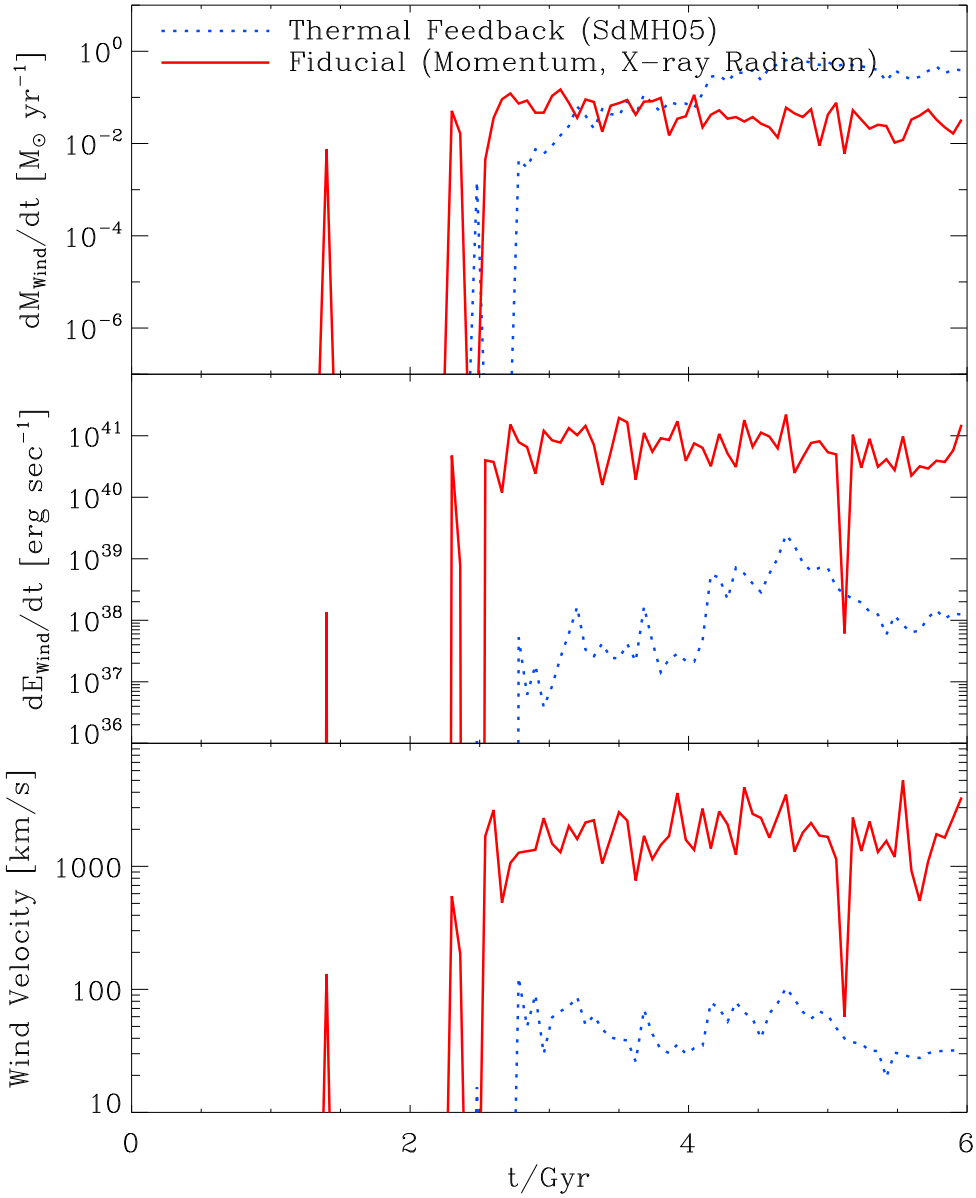



Figure 2.3: (*Top*) The evolution of wind mass loss rate, (*middle*) corresponding mechanical luminosities, and (*bottom*) gas wind velocities. All quantities are measured at 5 kpc from the black hole, above and below the disc midplane. Note that the thermal feedback model has much smaller wind velocity, a factor of 20 smaller compared to the mechanical feedback model.

$v_{\rm w} \sim 100$ km/s, is a factor of 20 smaller compared to the mechanical feedback model. The high wind velocity ($v_{\rm w} \sim 2000$ km/s) in our fiducial model is consistent with the recent velocity measurement of mass outflows in local Seyferts (Fischer et al., 2011; Müller-Sánchez et al., 2011; Pounds & Vaughan, 2011) which ranges from 700 km/s up to 3000 km/s.

The mechanical luminosities of the winds for two models are shown in the middle panel of Figure 2.3, and the averaged mechanical luminosities for last 1 Gyr are listed in Table 2. The thermal feedback model has considerably smaller mechanical luminosity $L_{\rm wind} \sim 10^{37}$ erg/s, because of its slow wind velocity. On the other hand, our fiducial model with mechanical feedback has strong outflow with $L_{\rm wind} \sim 10^{41}$ erg/s, which is consistent with the fact that large outflows with a kinetic power corresponding to a significant fraction of the AGN bolometric luminosity are commonly observed in X-ray observations of a number of quasars (mostly broad absorption line systems) that reveal significant absorption (*e.g.*, Chartas et al., 2003; Crenshaw et al., 2003; Pounds et al., 2003; Holt et al., 2008). The total kinetic energy carried away by the winds, *i.e.*, the mechanical luminosities integtated over the entire simulation time for the thermal model is $\Delta E_{\rm wind} \sim 2.8 \times 10^{55}$ ergs, while the momentum feedback model deposits $\Delta E_{\rm wind} \sim 8.3 \times 10^{57}$ ergs into the ISM within 6 Gyrs.

From a feedback energy coupling efficiency $\epsilon_{\rm w}$ which is an input parameter, and a total mass change for the BH, we calculate the energy released by the BH for the two cases using $\Delta E_{\rm mech} = \epsilon_{\rm w} \Delta M_{\rm BH} c^2$, and compare the ratios of the energy released in winds to the energy released by the BH, $\Delta E_{\rm wind}/\Delta E_{\rm mech}$. While the thermal feedback model emits only 0.1 % of the BH mechanical energy release in winds ($\Delta E_{\rm wind}/\Delta E_{\rm mech} = 0.0011$), the value rises to 38 % for the momentum feedback model, $\Delta E_{\rm wind}/\Delta E_{\rm mech} = 0.38$. That is, the mechanical energy put into momentum drives winds more efficiently than the energy put into heat.

Now we investigate the behavior of the two models for disk galaxy simulations at higher numerical resolution. However, such a study is complicated because of numerical resolution issues. In the previous studies using one-dimensional simulations, it was found that including the mass and momentum component has the largest effect on the final mass of the black hole, reducing the final black hole mass by a factor of up to 100 (OCCNP10). Turning on or off the energy input has

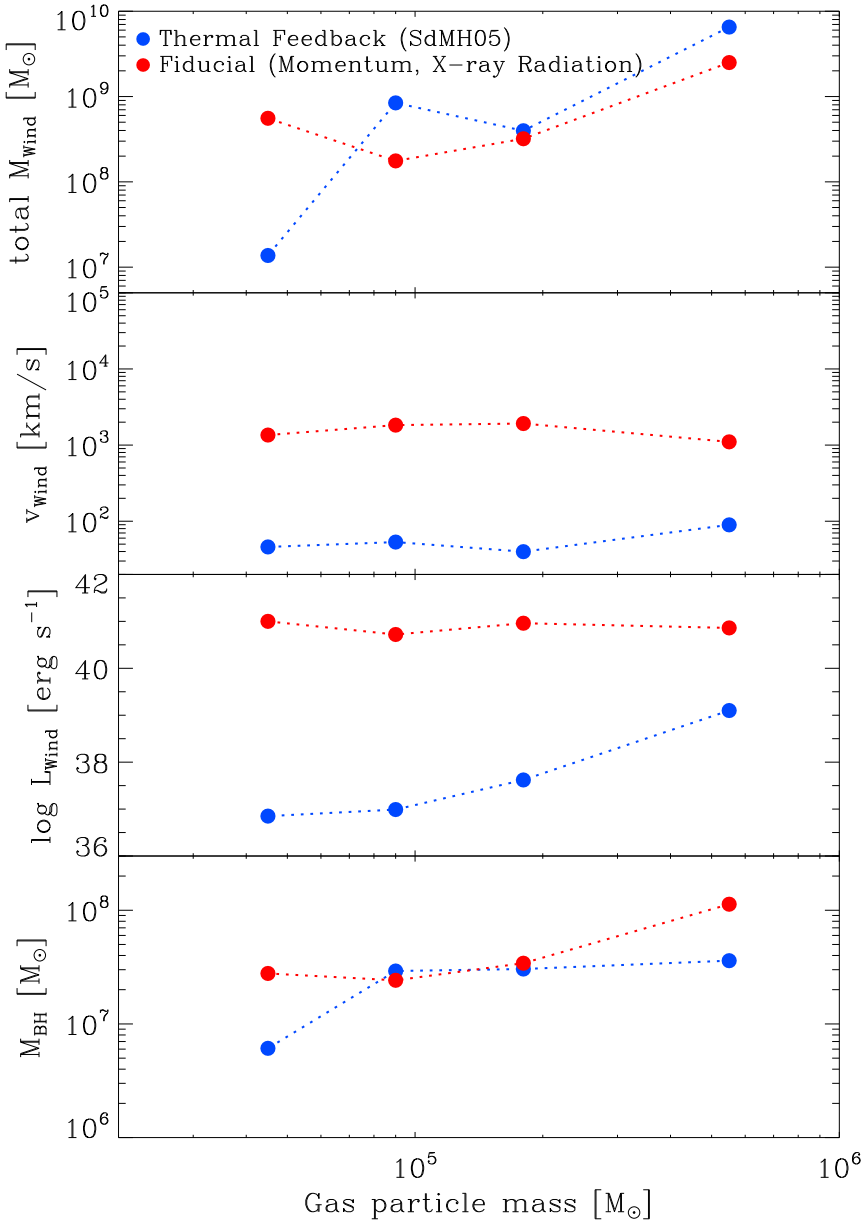



Figure 2.4: The outflow wind properties and the final black hole mass for the thermal feedback (blue) and the momentum feedback (red) are shown as a function of resolution (gas particle mass). The total outflow wind mass throughout the simulations, the averaged outward wind velocity, the averaged mechanical luminosity for last 1 Gyr, and the final black hole mass (*from top to bottom*) are shown. In the thermal feedback model, much weaken winds are generated in the highest resolution, since the injected feedback energy is quickly radiated away due to the very short cooling time of the gas.

relatively small effect, altering the black hole mass only by a factor of two. But, in this three-dimensional study we have found that the momentum feedback is not more efficient than thermal feedback in protecting the black hole from growth. However, the three-dimensional classic treatment has resolution effects that are difficult to correct because (1) the feedback energy is deposited outside of the Bondi radius whereas it is distributed within the Bondi radius in the much higher resolution one- and two- dimensional studies, and (2) the accretion is determined with the estimated gas density and sound speed averaged over the smoothing kernel, which is perhaps not the optimal procedure.

The results of the resolution dependency and the comparison of the wind properties of two feedback models are shown in Figure 2.4. Note that we adopt the smaller value of dimensionless accretion parameter $\alpha$ for the higher resolution runs as listed in Table 1. As described above, we measure the outflow wind properties throughout the simulations at $|z| = 5$ kpc from BH, above and below the disc midplane. The measured wind masses, the time averaged wind velocities, and the averaged mechanical luminosities over the last 1 Gyr are shown for each feedback model as a function of the gas particle mass in Figure 2.4. The total amount of mass in the outflowing wind is resolution dependent in both models, but the effects of resolution appear to be larger in the thermal feedback model. While the momentum feedback model in the highest resolution simulation has less wind mass (by a factor of 10) compared to the lowest resolution one, the wind mass difference between thermal feedback models at different resolutions reaches $10^3$. The wind velocity is resolution-independent for both feedback models, however thermal feedback models have much slower winds ($\sim 50 - 100$ km/s) compared to momentum feedback in all resolutions. The AGN-driven wind in the thermal feedback is also much slower than the velocity of the observed broad absorption line winds $\sim 10,000$ km/s (Crenshaw et al., 2003; Moe et al., 2009). In the case of the thermal feedback model at higher resolution, the shorter cooling time of dense gas makes thermal input increasingly inefficient at higher and higher numerical resolution.

In the case of the final mass of the black hole (bottom panel of Figure 2.4), the effect of the resolution in the momentum feedback model is moderate, whereas the thermal feedback model has a factor of 10 smaller final mass in the highest resolution compared to one in the lowest

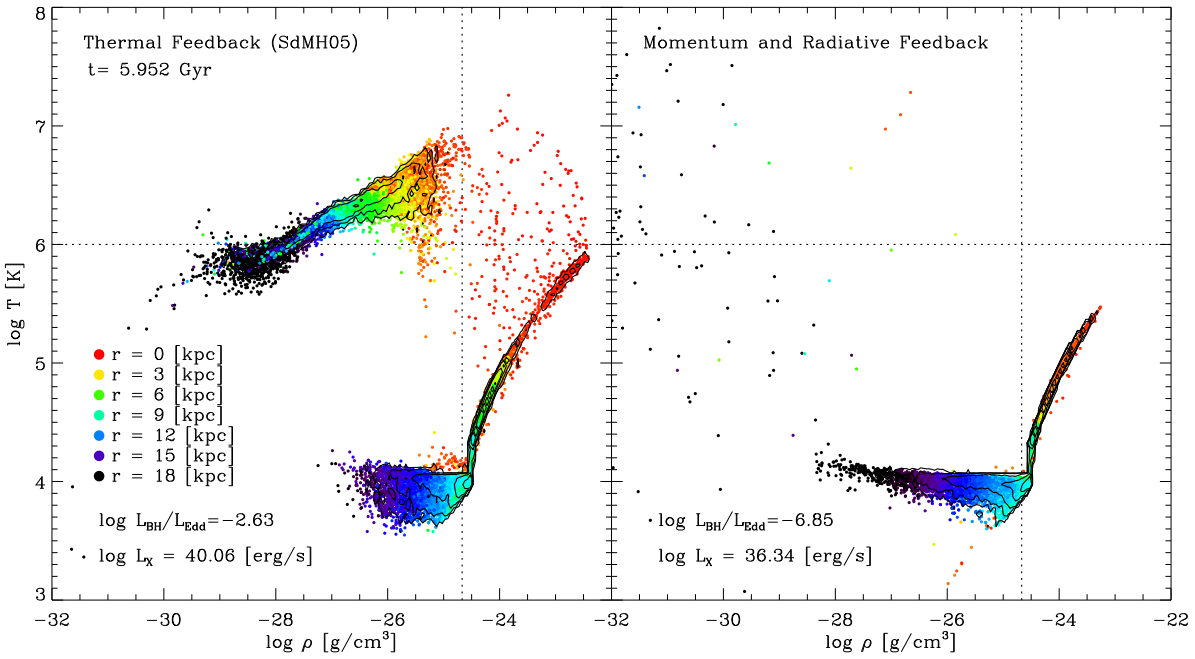



Figure 2.5: Distribution of gas in the density-temperature plane at $t = 5.95$ Gyr for the two feedback models. The radial distance from the BH is color coded, and the number density of SPH particles on the plot is shown with contours. The horizontal and vertical dotted lines respectively represent the temperature and density cuts we adopted for the X-ray luminosity estimate. Note that compared to the momentum feedback model, the thermal feedback model has much higher X-ray luminosity $L_{\rm X} \sim 3 \times 10^{40}$ erg/s, which is emitted from the diffuse hot gas, even during the low BH accretion phase ($L_{\rm BH}/L_{\rm Edd} \sim 0.002$).

resolution. For pure thermal feedback, we deposit the thermal feedback energy into the neighboring gas particles of the BH. The number of the affected neighboring gas particles is set to be the same for the different resolutions, therefore, in the higher resolution studies, we add energy into a smaller mass of the gas. In the higher resolution cases, gas particles in the central region have higher sound speed and lower density resulting in the lower BH accretion rate. However, the thermal feedback depends on the mass into which the energy is deposited, not on the number of particles. If the feedback energy were spread over constant mass by increasing the number of particles into which the thermal energy were added in the higher resolution study, the results would be essentially the same.

We compare the evolution of hot gas and X-ray emission of the two feedback models. Following Navarro et al. (1995), we assume that X-rays are produced by the cooling of hot and diffuse gas, and estimate the X-ray luminosity for each SPH gas particle as,

$$L_{\mathrm{X},i} = 1.2 \times 10^{-24} \frac{\rho_i m_{\mathrm{gas},i}}{(\mu m_p)^2} \left( \frac{kT_i}{1\mathrm{keV}} \right)^{1/2} \ \mathrm{ergs\ s^{-1}}, \tag{2.26}$$

where $\rho_i$, $m_{\mathrm{gas},i}$ and $T_i$ are the density, mass, and temperature of the $i$ th gas particle in cgs units, respectively, $m_p$ is the proton mass, and $\mu$ is the mean molecular weight. The X-ray emission computed via Equation 2.26 for each SPH particle is a lower limit as it assumes that the primary mechanism for X-ray emission is thermal bremsstrahlung. We do not include the X-ray emission via metal-line cooling although it is the more efficient cooling mechanism for metal-enriched gas with a temperature of $\sim 10^6$ K and would produce more X-ray emission. We also assume that the central region of the galaxy remains obscured because of the large column density of intervening gas and dust, and calculate the total X-ray luminosity as

$$L_{\mathrm{X,tot}} = \sum_{j=1}^{N_{\mathrm{hot\ gas}}} L_{\mathrm{X},i}, \tag{2.27}$$

where the sum is over all hot and diffuse gas particles. Following Cox et al. (2006), we define the 'hot and diffuse gas' with a temperature of $T \geq 10^6$ K, and a density $\rho \leq 3.16 \times 10^{-3} M_{\odot} \mathrm{pc}^{-3}$, which corresponds to the critical density for star formation.

In Figure 2.5, we show where the SPH particles lie in the density-temperature plane with the calculated X-ray luminosities for both feedback models. In the thermal feedback model, the energy input by the accreting black holes generates collimated, hot and slow winds perpendicular to the disk plane. These wind particles leave from the high density and hot temperature tip of the distribution of gas in the density-temperature plane, and cool down slowly as they move outward. Due to their low velocity and high density, the cooling time is relatively long, and these hot and diffuse winds emit X-rays with the luminosity far greater ( $\sim 10^{40}$ erg/s) than the momentum driven winds ($\sim 10^{36}$ erg/s). The momentum feedback model has much lower X-ray luminosity as

the momentum-driven winds quickly expel the X-ray emitting hot gas. Even during the low BH accretion phase with $L_{\rm BH}/L_{\rm Edd} \sim 0.002$, the X-ray luminosity of the thermal feedback model is much higher than what is typically seen from normal massive spiral galaxies at the present epoch ($10^{38} - 10^{39}$ erg/s in the $0.5 - 2.0$ keV band (Almy et al., 2000; Owen & Warwick, 2009; Boroson et al., 2011)). The X-ray luminosity of the thermal feedback model is a lower bound, since the inclusion of cosmologically infalling gas in the simulations would lead to an increase in the computed thermal X-ray emission.

We now discuss the effect of the amount of the momentum-driven flow, *i.e.*, number of momentum sharing neighbors in momentum feedback model. As described in Section 2.2, we let the wind particle share its momentum with the neighboring gas particles, to mimic the shocked swept-up ambient medium. Because of the resolution limit, we keep the number of momentum sharing neighbors constant, despite of the fact that a total swept-mass by momentum-driven wind depends on the mass of the BH (King, 2003). In order to study the effect of the number of neighbors to share the momentum feedback, we ran a series of simulations adopting different numbers of neighbors. *We find that the effects of sharing momentum with more gas particles is small.* Adding more particles is equivalent to assuming an early and brief transition to Sedov phase.

### 3.2 Galaxy merger simulation

In addition to isolated galaxies, we also performed an equal-mass galaxy merger simulation using our progenitor disk galaxy models. The merger simulation was ran at High numerical resolution (see Table 1) with the initial seed BH masses set at $10^5 M_\odot$. Following Johansson et al. (2009a) we adopt orbital geometry G13 (Naab & Burkert, 2003) for our merger simulation. This geometry corresponds to the inclinations $i_p = -109, i_s = 180$ and the arguments of the pericenter $\omega_p = 60, \omega_s = 0$ for the primary and secondary galaxies, respectively. The galaxies approach each other on a parabolic orbit where the initial separation of the progenitors is $R_{\rm init} = r_{\rm vir}$ and the pericentric distance is $r_{\rm peri} = 2r_{\rm d}$, where $r_{\rm vir} = 160h^{-1}$ kpc is the virial radius and

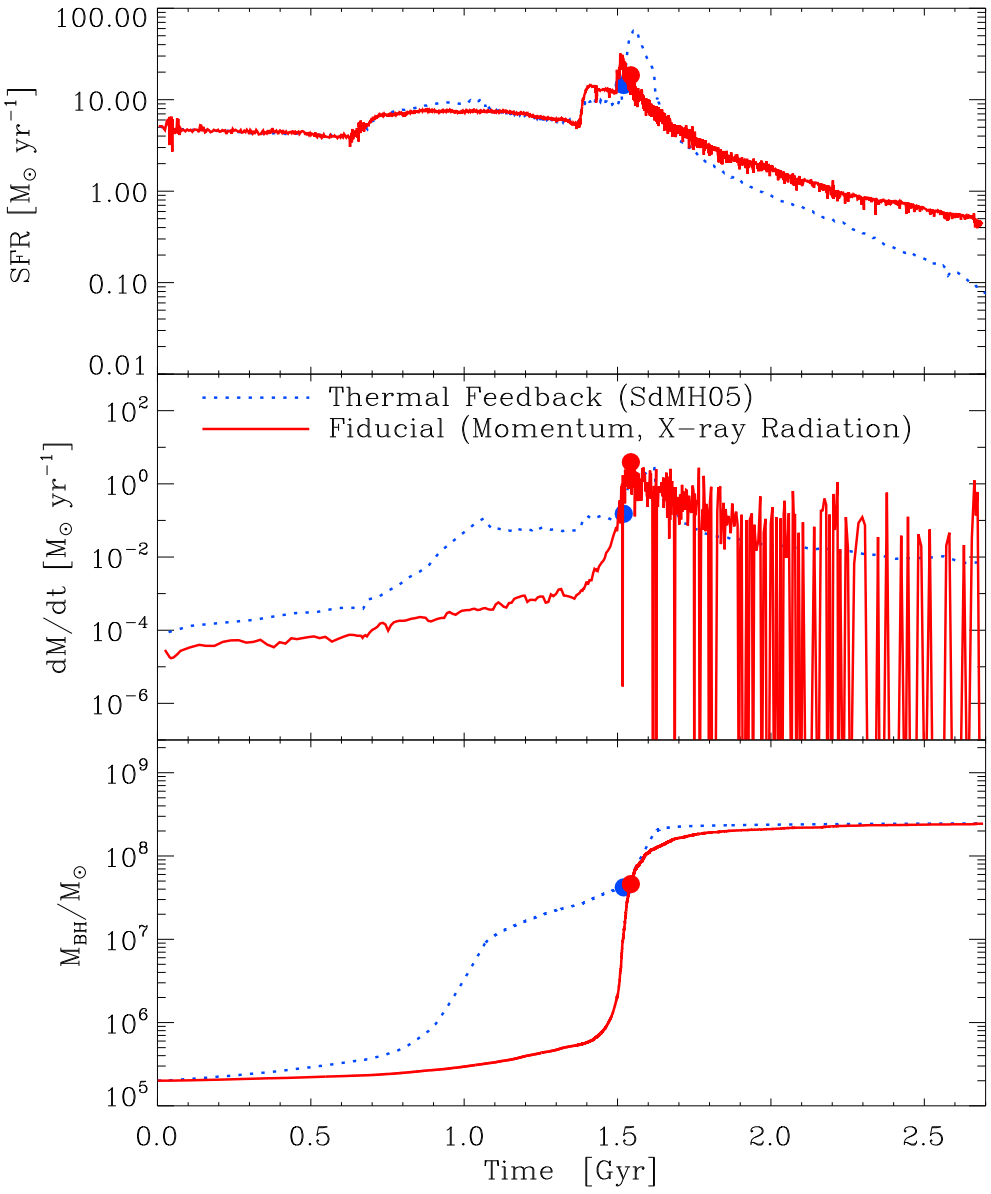



Figure 2.6: Comparison of the feedback models with a major merger of two galaxies: classical thermal feedback (blue), and our best proposed "Fiducial" model which has momentum mechanical feedback with the X-ray heating and radiation pressure (red). Evolution of the total star formation rate (*top*), the total accretion rate onto the black hole (*middle*) and the evolution of the black hole mass (*bottom*) are shown as a function of time for the 1:1 merger. The filled circles indicate the time of black hole merger. Note that both the star formation rate and the black hole growth are essentially similar in the previous thermal feedback model and the new momentum driven treatment. However, the degree of fluctuation in the mass accretion rate is greater in the momentum feedback model as shown in the isolated galaxy case.

$r_{\rm d} = 2.5h^{-1}$ kpc is the disk scale radius. The simulation was evolved for a total of $t = 3$ Gyr with the merger taking place at $t \sim 1.5$ Gyr. The equal-mass merger initial conditions are simulated using both the standard thermal feedback and the new momentum mechanical feedback with the X-ray heating and radiation pressure.

In Figure 2.6, we show the evolution of the resulting total star formation (top), black hole accretion (middle), and black hole mass (bottom) for the two feedback models as a function of time. A similar evolution is seen in the star formation rate for both models, however the new feedback fiducial model has episodic outbursts of mass accretion as shown in the isolated galaxy model. Even though the two feedback models have different black hole accretion history, the final mass of black hole is essentially the same. Other aspects of the two simulations, such as the X-ray thermal luminosity, are significantly different, and this will be discussed in later chapters.

### 3.3 Soft bondi criterion

Next, we turn our attention to the Bondi radius criterion. In order to test the new soft Bondi mechanisms for limiting accretion when numerical resolution is less than optimal, we ran two artificial test runs without any feedback, *i.e.*, "No Feedback" models, with and without soft Bondi criterion. As discussed earlier in the subsection 2.3, since any closest neighboring gas particles from the black hole at any distance are considered as potentially accreting particles, gas particles keep accreting onto the black hole and finally BH ends up swallowing all the gas in the host galaxy in the "No Feedback" model without soft Bondi criterion.

With the Bondi radius criterion added, we limit the accretion only to the gas particles statistically within the Bondi radius and we can prohibit the gas particles which are not within the gravitational influence of the black hole from accreting onto the black hole. In more realistic simulations which included feedback, the effects of our Bondi limitation are far less significant.

In Figure 2.7, we show the resulting SFRs, BH accretion rates, and BH mass growth for these two models with and without the Bondi radius criterion. Utilizing the Bondi radius criterion effectively regulates the mass accretion, reducing the final mass by a factor of 10.

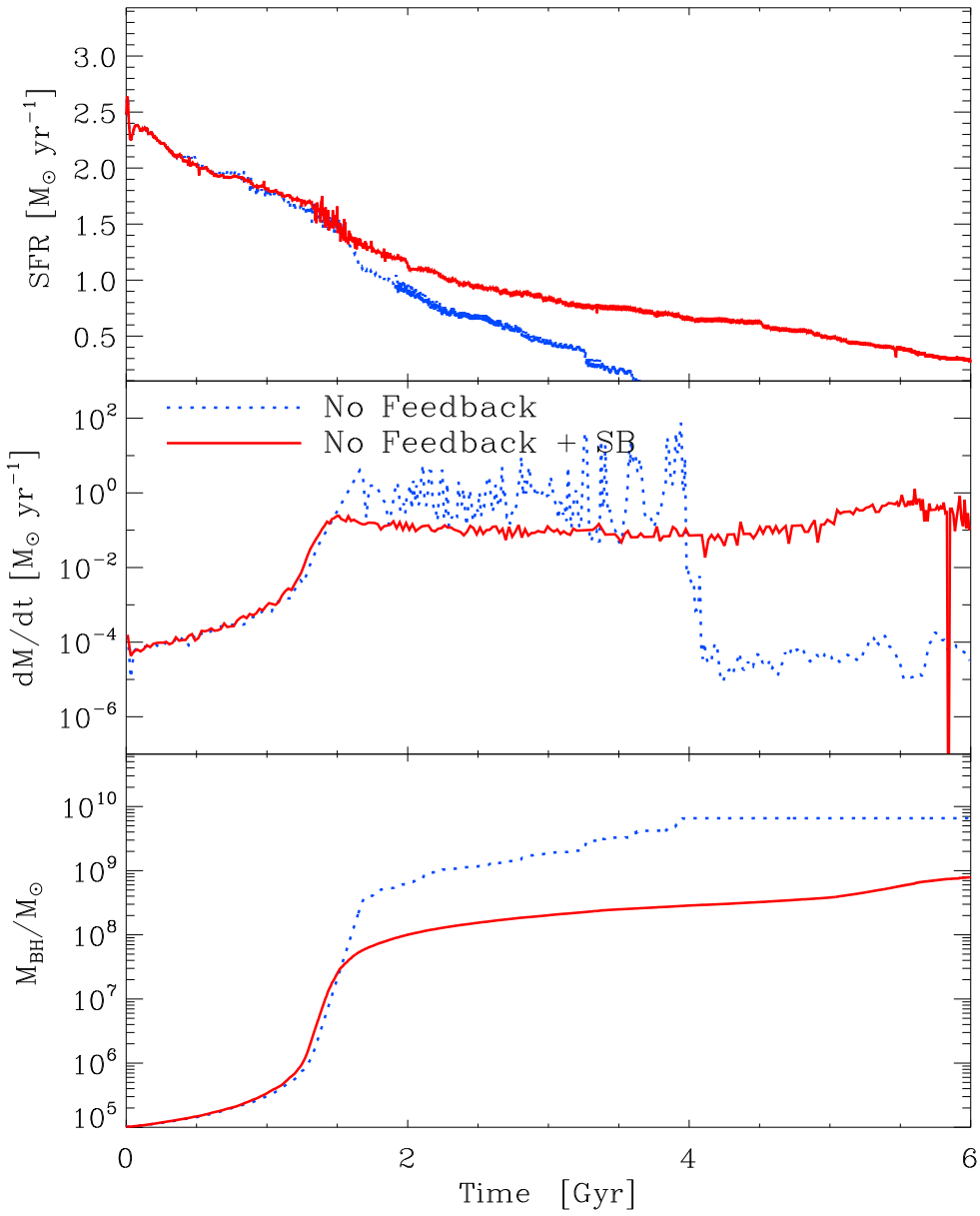



Figure 2.7: Comparison of the models with and without the Bondi radius criterion. Evolution of the global star formation rate (*top*), the accretion rate onto the black hole (*middle*) and the evolution of the black hole mass (*bottom*) are shown for each model. Note the order of magnitude reduction in the total accreted mass occasioned by including the Bondi limiter.

### 3.4 Fiducial model and the effects of other physics

In order to isolate and compare the effects of each feedback mechanism or modification made in the accretion, we perform the test simulations with one modification missing. In Figure 2.8, we show the temporal evolution of SFR, mass accretion rate onto BH and BH mass of three distinctive models, the one without radiative heating and radiation pressure (Fiducial w/o XRP), the one without the Eddington force (Fiducial w/o EF), and the one without the Soft Bondi radius criterion (Fiducial w/o SB), along with the fiducial model with all modifications as a reference. The radiative heating and radiation pressure is most effective among them, limiting the final mass of BH a factor of 4. Compared to radiative feedback, both Eddington force and Bondi criterion have minor effects on the final BH mass.

## 4 Summary

Absent a specific mechanism for transferring energy to particles surrounding an accreting BH, the AGN feedback via mass, and momentum output have not been included in classic thermal feedback works in three-dimensional hydrodynamic simulations. In this chapter, we have included the momentum mechanical feedback in the smoothed particle hydrodynamic simulation code, GADGET-2. We also include a treatment of the feedback by the X-ray radiation which emanates from the black hole and heats the surrounding gas in the host galaxies as well as radial momentum added to the fluid. We statistically limit accretion to gas particles which are gravitationally bound to the central black hole (Bondi radius criterion).

A series of test simulations of isolated systems with new implementations of the momentum feedback and radiative feedback with new criteria on mass accretion are performed. Relevant quantitative properties of the models are presented in Table 2, while the general results can be summarized as the following:

1. Overall, the black hole growth is quite similar in the two approaches, so the successful prediction of the $M_{\rm BH} - \sigma$ relation by Di Matteo et al. (2005, 2008) would be expected to be maintained in the new approach.

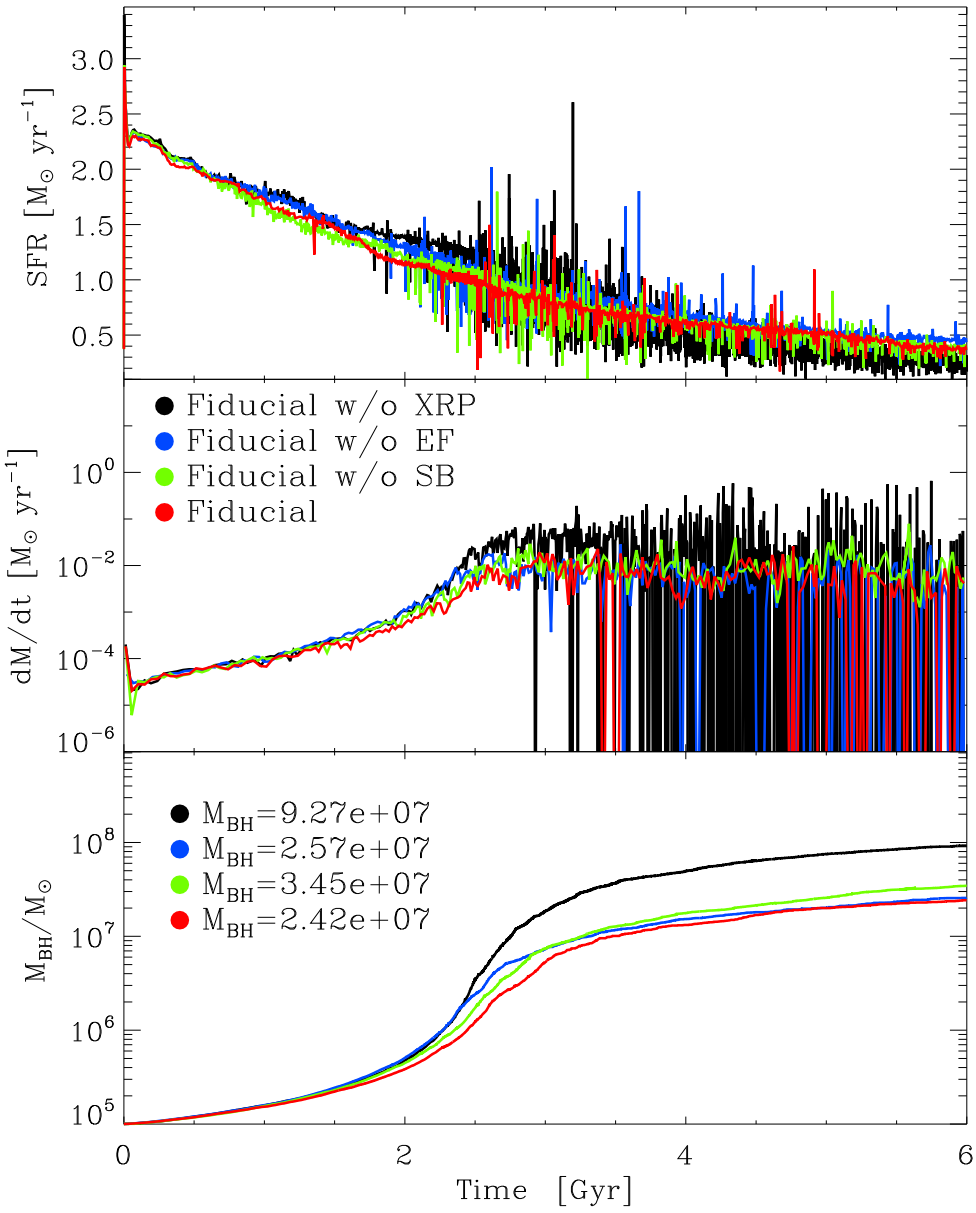



Figure 2.8: Various model comparison. Evolution of the global star formation rate (*top*), the accretion rate onto the black hole (*middle*) and the evolution of the black hole mass (*bottom*) in simulation of an isolated gas-rich galaxy. The largest of the newly included effects is clearly due to the X-ray heating and radiation pressure (XRP).

2. Our best proposed fiducial model with mechanical and radiative feedback by hard X-rays has much higher velocity outflows compared to the thermal feedback model, with $v_{\rm w} \sim 2000$ km/s and $L_{\rm wind} \sim 10^{42}$ erg/s. The total emitted kinetic energy of mechanical feedback model is $\sim 100$ times higher than that of thermal feedback model, even when the same feedback energy coupling efficiency is assumed and the black hole growth is similar. The outflows found in our fiducial model have properties broadly similar to those observed in some local Seyfert galaxies (Alatalo et al., 2011; Fischer et al., 2011; Müller-Sánchez et al., 2011).

3. The hot gas produced by slow, dense, thermally driven winds emits an X-ray luminosity significantly greater ($\sim 10^{40}$ erg/s) than the momentum driven winds ($\sim 10^{36}$ erg/s). This X-ray luminosity of the thermal feedback model is also far greater than what is typically seen from normal spiral galaxies ($\sim 10^{38}$ erg/s) (Almy et al., 2000; Owen & Warwick, 2009).

4. In the mechanical feedback model, the fluctuation level in both radiant and wind outputs is considerably greater than in the standard thermal feedback model. While the thermal feedback model has a steady mass accretion with the Eddington ratio $L_{\rm BH}/L_{\rm Edd} = 0.001 - 0.01$ throughout the simulations, the momentum feedback model has stochastic bursts in the mass accretion with the Eddington ratio, which spans from $L_{\rm BH}/L_{\rm Edd} = 10^{-6}$ to 1.

5. In an artificial model computed without any feedback mechanisms (No Feedback Model), the black hole grows to $\sim 10^{10} M_{\odot}$ accreting all the gas particles in the host galaxy. As noted, the standard prescription for accretion does not require the accreted particles be gravitationally bound to the central BH. However, the statistical implementation of the Bondi radius criterion can effectively limit the accretion of the gas particles to gravitationally bound particles, reducing the final mass of BH by a factor of 10. In more realistic models with feedback the differences are small.

6. Radiative heating and radiation pressure on the ISM by photons emitted by the central BH moderately reduces the final mass of BH, by a factor of 4.

7. The growth of the black hole is confirmed to be essentially the same in the thermal and momentum feedback models in an equal-mass galaxy merger simulations.

# Bibliography

Alatalo, K., et al. 2011, ApJ, 735, 88

Aller, M. C. & Richstone, D. O. 2007, ApJ, 665, 120

Almy, R. C., McCammon, D., Digel, S. W., Bronfman, L., & May, J. 2000, ApJ, 545, 290

Arav, N., Moe, M., Costantini, E., Korista, K. T., Benn, C., & Ellison, S. 2008, ApJ, 681, 954

Barai, P., Proga, D., & Nagamine, K. 2011, MNRAS, 418, 591

Barway, S. & Kembhavi, A. 2007, ApJ, 662, L67

Bondi, H. 1952, MNRAS, 112, 195

Bondi, H. & Hoyle, F. 1944, MNRAS, 104, 273

Booth, C. M. & Schaye, J. 2009, MNRAS, 398, 53

Boroson, B., Kim, D.-W., & Fabbiano, G. 2011, ApJ, 729, 12

Chartas, G., Brandt, W. N., & Gallagher, S. C. 2003, ApJ, 595, 85

Ciotti, L. & Ostriker, J. P. 2007, ApJ, 665, 1038

Ciotti, L., Ostriker, J. P., & Proga, D. 2009, ApJ, 699, 89

—. 2010, ApJ, 717, 708

Cox, T. J., Di Matteo, T., Hernquist, L., Hopkins, P. F., Robertson, B., & Springel, V. 2006, ApJ, 643, 692

Crenshaw, D. M., Kraemer, S. B., & George, I. M. 2003, ARA&A, 41, 117

Dai, X., Shankar, F., & Sivakoff, G. R. 2008, ApJ, 672, 108

de Kool, M., Arav, N., Becker, R. H., Gregg, M. D., White, R. L., Laurent-Muehleisen, S. A., Price, T., & Korista, K. T. 2001, ApJ, 548, 609

Debuhr, J., Quataert, E., & Ma, C.-P. 2011, MNRAS, 412, 1341

—. 2012, MNRAS, 420, 2221

Debuhr, J., Quataert, E., Ma, C.-P., & Hopkins, P. 2010, MNRAS, 406, L55

Di Matteo, T., Colberg, J., Springel, V., Hernquist, L., & Sijacki, D. 2008, ApJ, 676, 33

Di Matteo, T., Springel, V., & Hernquist, L. 2005, Nat, 433, 604

Dressler, A. 1989, in IAU Symposium, Vol. 134, Active Galactic Nuclei, ed. D. E. Osterbrock & J. S. Miller, 217

Dubois, Y., Devriendt, J., Slyz, A., & Silk, J. 2009, MNRAS, 399, L49

Dubois, Y., Devriendt, J., Slyz, A., & Teyssier, R. 2012, MNRAS, 420, 2662

Dunn, J. P., Bautista, M., Arav, N., Moe, M., Korista, K., Costantini, E., Benn, C., Ellison, S., & Edmonds, D. 2010, ApJ, 709, 611

Durier, F. & Dalla Vecchia, C. 2012, MNRAS, 419, 465

Fabian, A. C. 1999, MNRAS, 308, L39

Fischer, T. C., Crenshaw, D. M., Kraemer, S. B., Schmitt, H. R., Mushotsky, R. F., & Dunn, J. P. 2011, ApJ, 727, 71

Gebhardt, K., et al. 2000, ApJ, 539, L13

Gibson, R. R., et al. 2009, ApJ, 692, 758

Graham, A. W., Onken, C. A., Athanassoula, E., & Combes, F. 2011, MNRAS, 412, 2211

Greene, J. E. & Ho, L. C. 2007, ApJ, 667, 131

Gültekin, K., et al. 2009, ApJ, 698, 198

Haardt, F. & Madau, P. 1996, ApJ, 461, 20

Hambrick, D. C., Ostriker, J. P., Naab, T., & Johansson, P. H. 2011, ApJ, 738, 16

Hernquist, L. 1990, ApJ, 356, 359

Hewett, P. C. & Foltz, C. B. 2003, AJ, 125, 1784

Ho, L. C. 2009, ApJ, 699, 626

Holt, J., Tadhunter, C. N., & Morganti, R. 2008, MNRAS, 387, 639

Hopkins, P. F., Hernquist, L., Cox, T. J., Di Matteo, T., Martini, P., Robertson, B., & Springel, V. 2005, ApJ, 630, 705

Hoyle, F. & Lyttleton, R. A. 1939, Proceedings of the Cambridge Philosophical Society, 34, 405

Johansson, P. H., Burkert, A., & Naab, T. 2009a, ApJ, 707, L184

Johansson, P. H., Naab, T., & Burkert, A. 2009b, ApJ, 690, 802

Katz, N., Weinberg, D. H., & Hernquist, L. 1996, ApJS, 105, 19

Kauffmann, G. & Heckman, T. M. 2009, MNRAS, 397, 135

Kim, J.-h., Wise, J. H., Alvarez, M. A., & Abel, T. 2011, ApJ, 738, 54

King, A. 2003, ApJ, 596, L27

Kormendy, J. 1993, in The Nearest Active Galaxies, ed. J. Beckman, L. Colina, & H. Netzer, 197–218

Kormendy, J. & Richstone, D. 1995, ARA&A, 33, 581

Krolik, J. H. & Begelman, M. C. 1988, ApJ, 329, 702

Lynden-Bell, D. 1969, Nat, 223, 690

Magorrian, J., et al. 1998, AJ, 115, 2285

Marconi, A. & Hunt, L. K. 2003, ApJ, 589, L21

McKee, C. F. & Ostriker, J. P. 1977, ApJ, 218, 148

Moe, M., Arav, N., Bautista, M. A., & Korista, K. T. 2009, ApJ, 706, 525

Monaghan, J. J. 1992, ARA&A, 30, 543

Müller-Sánchez, F., Prieto, M. A., Hicks, E. K. S., Vives-Arias, H., Davies, R. I., Malkan, M., Tacconi, L. J., & Genzel, R. 2011, ApJ, 739, 69

Naab, T. & Burkert, A. 2003, ApJ, 597, 893

Navarro, J. F., Frenk, C. S., & White, S. D. M. 1995, MNRAS, 275, 720

—. 1997, ApJ, 490, 493

Nayakshin, S. & Power, C. 2010, MNRAS, 402, 789

Novak, G. S., Ostriker, J. P., & Ciotti, L. 2011, ApJ, 737, 26

Omma, H., Binney, J., Bryan, G., & Slyz, A. 2004, MNRAS, 348, 1105

Ostriker, J. P., Choi, E., Ciotti, L., Novak, G. S., & Proga, D. 2010, ApJ, 722, 642

Owen, R. A. & Warwick, R. S. 2009, MNRAS, 394, 1741

Pounds, K. A., Reeves, J. N., King, A. R., Page, K. L., O'Brien, P. T., & Turner, M. J. L. 2003, MNRAS, 345, 705

Pounds, K. A. & Vaughan, S. 2011, MNRAS, 413, 1251

Proga, D. & Kallman, T. R. 2004, ApJ, 616, 688

Proga, D., Ostriker, J. P., & Kurosawa, R. 2008, ApJ, 676, 101

Proga, D., Stone, J. M., & Kallman, T. R. 2000, ApJ, 543, 686

Rees, M. J. 1984, ARA&A, 22, 471

Richstone, D., et al. 1998, Nat, 395, A14

Saitoh, T. R. & Makino, J. 2009, ApJ, 697, L99

Sazonov, S. Y., Ostriker, J. P., Ciotti, L., & Sunyaev, R. A. 2005, MNRAS, 358, 168

Sazonov, S. Y., Ostriker, J. P., & Sunyaev, R. A. 2004, MNRAS, 347, 144

Shakura, N. I. & Sunyaev, R. A. 1973, A&A, 24, 337

Sijacki, D., Pfrommer, C., Springel, V., & Enßlin, T. A. 2008, MNRAS, 387, 1403

Sijacki, D., Springel, V., Di Matteo, T., & Hernquist, L. 2007, MNRAS, 380, 877

Soltan, A. 1982, MNRAS, 200, 115

Springel, V. 2005, MNRAS, 364, 1105

—. 2010, ARA&A, 48, 391

Springel, V., Di Matteo, T., & Hernquist, L. 2005a, ApJ, 620, L79

—. 2005b, MNRAS, 361, 776

Springel, V. & Hernquist, L. 2003, MNRAS, 339, 289

Tacconi, L. J., Genzel, R., Blietz, M., Cameron, M., Harris, A. I., & Madden, S. 1994, ApJ, 426, L77

Teyssier, R., Moore, B., Martizzi, D., Dubois, Y., & Mayer, L. 2011, MNRAS, 414, 195

Tremaine, S., et al. 2002, ApJ, 574, 740

Younger, J. D., Hopkins, P. F., Cox, T. J., & Hernquist, L. 2008, ApJ, 686, 815

Yu, Q. & Tremaine, S. 2002, MNRAS, 335, 965

# Chapter 3

# Consequences of Radiative and Mechanical Feedback from Black Holes in Galaxy Mergers


**ABSTRACT**

We employ hydrodynamical simulations to study the effect of AGN mechanical and radiation feedback on the formation of bulge dominated galaxies via mergers of disk galaxies. The merging galaxies have mass-ratios of 1:1 to 6:1 and include pre-existing hot gaseous halos to properly account for the global impact of AGN feedback. We compare three models: (1) no black hole and no AGN feedback; (2) thermal AGN feedback; and (3) mechanical and radiative AGN feedback. The last model is motivated by observations of broad absorption line quasars which show winds with initial velocities of $v_{\rm w} \geq 10{,}000$ km s$^{-1}$ and also heating associated with the central AGN X-ray radiation. The primary changes in gas properties due to mechanical AGN feedback are lower thermal X-ray luminosity from the final galaxy - in better agreement with observations - and galactic outflows with higher velocity $\sim 1000$ km s$^{-1}$ similar to recent direct observations of nearby merger remnants. The kinetic energy of the outflowing gas is a factor of $\sim 20$ higher than in the thermal feedback case. All merger remnants with momentum-based AGN feedback, independent of their progenitor mass-ratios, follow the observed relations between stellar velocity dispersion and black hole mass ($M_{\rm BH} - \sigma$) as well as X-ray luminosity ($L_X - \sigma$) with $10^{37.5} \lesssim L_X(0.3-8\ {\rm keV}) \lesssim 10^{39.2}$ for velocity dispersions in the range of

120 km s$^{-1}$ $\lesssim \sigma \lesssim$ 190 km s$^{-1}$. In addition, the mechanical feedback produces a much greater AGN variability. We also show that gas is more rapidly and impulsively stripped from the galactic centres driving a moderate increase in galaxy size and decrease in central density with the mechanical AGN feedback model. However, the black hole mass growth required to produce the observed galaxy size and central density evolution is inconsistent with the observed $M_{\rm BH} - \sigma$ relation.

# 1 Introduction

Accretion onto central massive black holes in galactic nuclei emits energy in the form of electromagnetic radiation, relativistic jets, and wider angle non-relativistic outflows (Lynden-Bell, 1969; Rees, 1984). The coupling of the energy output to the gas in galaxies, i.e. active galactic nucleus (AGN) feedback, is believed to play an important role in galaxy formation by regulating central star formation and produce approximately the linear relationship between the central massive black hole and the stellar component of the elliptical galaxy (Dressler, 1989; Kormendy, 1993; Magorrian et al., 1998; Gebhardt et al., 2000; Tremaine et al., 2002; Marconi & Hunt, 2003; Aller & Richstone, 2007; Gültekin et al., 2009). However, understanding the precise physical mechanisms by which this feedback occurs poses a major challenge for our understanding of the connection between AGN physics and galaxy evolution. Several mechanisms have been proposed and numerically investigated, including radiative heating (Sazonov et al., 2005; Ciotti & Ostriker, 2007; Ciotti et al., 2009), radiation pressure (Debuhr et al., 2010), cavities generated by the injection of thermal energy or cosmic rays (Dalla Vecchia et al., 2004; Sijacki et al., 2007, 2008; Guo & Mathews, 2010; Broderick et al., 2012; Pfrommer et al., 2012; Puchwein & Springel, 2013), thermal energy input (Di Matteo et al., 2005; Springel, 2005) or bipolar mechanical outflows and jets (Omma et al., 2004; Debuhr et al., 2012; Choi et al., 2012; Gaspari et al., 2012).

Based on one- and two- dimensional computations, Ostriker et al. (2010) quantitatively studied the relative importance of the different processes in protecting the central black hole from excessive mass growth and found mechanical feedback with proper mass and momentum injection

to be the dominant mode of feedback. Energy deposition from a central AGN feedback takes place when the accretion rates onto the central black hole are high, e.g. when the density of the surrounding gas is high. If the cooling time of the gas is resolved and is sufficiently short, the gas tends to quickly radiate away any thermal energy input. Therefore, thermal energy input is a rather inefficient regulator for black hole growth while the momentum input, which cannot be radiated away easily, was found to be very efficient in limiting the infall and accretion onto the central black hole in one- and two- dimensional simulations (Ostriker et al., 2010). It also tends to impart considerably more kinetic energy to the outflowing gas at a given accretion rate and efficiency of energy release.

In this context, Choi et al. (2012) hereafter CONJ12, introduced and tested the modeling of mechanical feedback from AGN communicating to the ambient gas via a bipolar wind in three-dimensional smoothed particle hydrodynamical (SPH) simulations to verify whether this form of feedback is able to regulate black hole growth. This treatment also includes a modified algorithm for the black hole accretion rate with a Bondi radius criterion and the effect of radiation from the accreting black hole. We used simulations of isolated disks and of one equal-mass disk merger to demonstrate that massive, non-relativistic outflows can indeed regulate the black hole growth. Also, the new treatment of the AGN feedback results in stronger outflows at higher velocity (up to $v_{\rm w} \sim 2,000$ km s$^{-1}$), a greater fluctuation level in both the radiant and wind outflow rates, and lower X-ray luminosities of hot gas compared to the thermal feedback treatment that is commonly adopted in many three-dimensional hydrodynamic calculations (e.g., Springel et al., 2005a,b; Di Matteo et al., 2005; Hopkins et al., 2005; Sijacki et al., 2007, 2009; Booth & Schaye, 2009; Johansson et al., 2009b; Teyssier et al., 2011; Dubois et al., 2012; Newton & Kay, 2013).

In this chapter we extend our previous work and study the effect of radiation and strong winds from AGN on the gas as well as the stellar component of the host galaxies during mergers of equal- and unequal-mass disk galaxies. These merging disk galaxies now include an extended hot gaseous halo (Moster et al., 2011) as predicted by cosmological hydrodynamical simulations of galaxy formation (Toft et al., 2002; Crain et al., 2010, 2013), and as inferred from X-ray

observations of normal massive disk galaxies (e.g. Anderson & Bregman, 2011; Anderson et al., 2013; Li & Wang, 2013). Such a component was neglected in previous AGN feedback studies using idealized simulations. It is, however, most relevant for a proper treatment of the hydrodynamic interaction of the AGN wind with the ambient medium and for a more accurate determination of the X-ray properties.

We further study the effect of mechanical AGN feedback on the evolution of the stellar component of the host galaxy. During active phases of the black hole large amounts of gas can be removed from the central regions of the galaxies on short timescales. It has been argued that this process can trigger a significant dynamical expansion of the stellar component (Fan et al., 2008, 2010; Hopkins et al., 2010; Martizzi et al., 2012; Dubois et al., 2013). This process might be relevant in the context of recent observational studies indicating that many massive, passively evolving galaxies at high redshift ($z > 1$) are more compact than local galaxies with the same stellar mass (Ferguson et al., 2004; Trujillo et al., 2004; Longhetti et al., 2007; Toft et al., 2007; Trujillo et al., 2007; Cimatti et al., 2008; van Dokkum et al., 2008; Damjanov et al., 2009). While much of the mass growth and corresponding size growth in the outer parts of giant ellipticals is potentially driven by accretion of stars in minor mergers (Oser et al., 2012; Johansson et al., 2012; Hilz et al., 2012; Oogi & Habe, 2013; Hilz et al., 2013; Bédorf & Portegies Zwart, 2013, but see Newman et al., 2012; Nipoti et al., 2012). Observations by van Dokkum et al. (2008); Szomoru et al. (2010); Saracco et al. (2012); van de Sande et al. (2013) and others also indicate a decrease in central densities which does not easily occur in the minor merger picture (cf. Hilz et al., 2013). These observations suggest that in addition to merging an additional mechanism is needed. We test the contribution of the quasar activity to the galaxy size growth and the central density decrease.

The chapter is organized as follows. In Section 2, we provide a brief summary of the simulation code and the initial conditions. We also summarize the algorithmic implementation of the black hole accretion and feedback model. We present our result for the equal- and unequal-mass merger simulations in Section 3 with a detailed analysis of the effect of the assumed feedback model ('mechanical' vs. 'thermal') and the progenitor mass-ratio on star formation, black hole growth

growth and the properties of the AGN driven wind. In Section 4 we discuss the impact of mechanical and thermal feedback on the properties of the merger remnant and highlight the effect on the X-ray luminosities as well as the size and central density of the stellar component. We also discuss the black hole and X-ray scaling relations. Finally, in Section 5 we summarize and discuss our main results.

# 2 Model

## 2.1 Numerical code

We perform the simulations using the parallel TreeSPH-code GADGET (Springel, 2005). The code employs the Lagrangian SPH (see Monaghan, 1992) technique for gas particles and solves the equations of motion for the collisionless dark matter and star particles. The sub-resolution modeling for star formation assumes a two-phase medium of hot and cold gas (McKee & Ostriker, 1977; Springel & Hernquist, 2003), and the stars form from a cold component embedded in sufficiently dense gas, i.e., $n > n_{\rm th} = 0.128$ cm$^{-3}$ with the short-lived stars supplying an energy of $10^{51}$ erg to the surrounding gas per supernovae (SNe). SN-driven galactic winds are not included in this study. We include the radiative cooling for a primordial composition of hydrogen and helium (Katz et al., 1996) and a spatially uniform time-independent UV background radiation field with a modified Haardt & Madau (1996) spectrum. The dimensionless Hubble parameter is $h = 0.71$ such that the present-day Hubble parameter is $H_0 = 71$ km s$^{-1}$ Mpc$^{-1}$.

## 2.2 Initial conditions and galaxy parameters

We simulate binary mergers of equal and unequal mass and the initial galaxy disk galaxy models are constructed following Springel et al. (2005b). We additionally include a diffuse, rotating hot gaseous halo as described in Moster et al. (2011, 2012). The progenitor galaxies are composed of a rotationally supported disk of gas and stars, a stellar bulge and a central black hole embedded in a halo consisting of hot gas and dark matter. Each galaxy has a virial velocity and radius

$v_{\rm vir} = 160$ km s$^{-1}$, and $r_{\rm vir} = 160\ h^{-1}$ kpc corresponding to a virial mass of $M_{\rm vir} = 9.53 \times 10^{11}$ $h^{-1} M_{\odot}$. The Hernquist (1990) profile dark matter halos are constructed with a concentration parameter $c = 9$ of the corresponding Navarro–Frenk–White (NRW) halo (Navarro et al., 1995). The dark matter halo is then populated with exponential disks with a baryonic mass fraction of $m_d = 0.041$, with a gas fraction of $f_{\rm gas} = 0.2$ and with the rest being stars. We set the disk scale length $r_d$ using the Mo et al. (1998) formalism, assuming that the fractional disk angular momentum equals the disk mass fraction $m_d$ for a constant halo spin of $\lambda = 0.033$ for all models. The vertical scale height $z_0$ of the stellar disk is radially constant and set to $0.2 r_d$. The black hole at the centre of each galaxy is modeled as a collisionless sink particle which can accrete gas and the initial seed black hole masses is $10^6 M_{\odot}$.

We model the hot gaseous component as a slowly rotating halo with a spherical density profile. The density distribution follows the observationallymotivated beta-profile (Cavaliere & Fusco-Femiano, 1976; Jones & Forman, 1984; Eke et al., 1998). It has three free parameters: the central density $\rho_0$, the core radius $r_c$ and the outer slope parameter beta. We adopt $\beta = 2/3$ (Jones & Forman, 1984), $r_c = 0.22 r_s$ (Makino et al., 1998) and fix $\rho_0$ such that the hot gas mass within the virialradius is $M_{hg}$.

We set the orbital geometry to be G13 (Naab & Burkert, 2003) for our merger simulation following Johansson et al. (2009b). This geometry corresponds to the inclinations $i_p = -109, i_s = 180$ and the arguments of pericenter $\omega_p = 60, \omega_s = 0$ for the primary and secondary galaxies, respectively. The galaxies approach each other on parabolic orbits. The initial separation of the progenitors of the 1:1 mergers is $R_{\rm init} = r_{\rm vir}$ with a pericentric distance of $r_{\rm peri} = 2 r_{\rm d}$, where $r_{\rm vir} = 160 h^{-1}$ kpc is the virial radius and $r_{\rm d} = 2.5 h^{-1}$ kpc is the disk scale length. For the unequal-mass mergers the initial separation is the mean of the virial radii of the two galaxies, $R_{\rm init} = 143.5 h^{-1}$ kpc for the 2:1, $135 h^{-1}$ kpc for the 3:1, $130.4 h^{-1}$ kpc for the 4:1 and $124 h^{-1}$ kpc for the 6:1 merger. The pericentric distance is $r_{\rm peri} = 2 r_{\rm d,mean}$, the mean disk scale radius of the two progenitors, meaning that it is $4.45 h^{-1}$ kpc for 2:1, $4.2 h^{-1}$ kpc for 3:1, $4.0 h^{-1}$ kpc for 4:1 and $3.8 h^{-1}$ kpc for 6:1. Every simulation was evolved for a total of $t = 3$ Gyr with the merger taking place at around $t \sim 1.5 - 2.0$ Gyr.

For all simulations, the primary galaxy is realized with $1.7 \times 10^6$ particles: the halo has $8.0 \times 10^5$ dark matter particles and $1.3 \times 10^5$ gas particles, the disk has $4.8 \times 10^5$ stellar particles and $1.2 \times 10^5$ gas particles, and the bulge has $2.0 \times 10^5$ stellar particles. For the secondary galaxies in minor mergers, we scale down the galaxy masses and particle resolution accordingly in order to maintain equal mass resolution. The smaller galaxy in a 2:1 merger, for example, has half the number of particles than the more massive galaxy, resulting in $4.0 \times 10^5$ dark matter particles, $1.3 \times 10^5$ gas particles, and $3.4 \times 10^5$ stellar particles. All gas and star particles have the same mass of $m_{*,\rm gas} = 6.5 \times 10^4\ M_\odot h^{-1}$ (we spawn one star particle per gas particle), whereas the dark matter particles have a mass of $m_{\rm DM} = 1.1 \times 10^6\ M_\odot h^{-1}$. The gravitational force softening length is $\epsilon = 66$ pc for the dark matter particles and $\epsilon = 16$ pc for the gas and star particles respectively, following the choice of the softening parameter in Dehnen (2001).

### 2.3 The traditional thermal black hole feedback model

In the widely adopted thermal black hole feedback models (e.g. Springel et al., 2005b), the sub-grid accretion rate on scales smaller than the resolution is estimated with a Bondi-Hoyle-Lyttleton parameterization (Hoyle & Lyttleton, 1939; Bondi & Hoyle, 1944; Bondi, 1952). For gas with density $\rho$, sound speed $c_{\rm s}$ and velocity relative to the black hole $v$, the mass accretion rate onto the central region is given as:

$$\dot{M}_{\rm B} = \frac{4\pi\alpha G^2 M_{\rm BH}^2 \rho}{(c_{\rm s}^2 + v^2)^{3/2}}, \tag{3.1}$$

where $\alpha$ is a dimensionless parameter setting the efficiency of the accretion. It is assumed that the accretion is limited to the Eddington rate given by

$$\dot{M}_{\rm edd} \equiv \frac{4\pi G M_{\rm BH} m_{\rm p}}{\epsilon_{\rm r}\sigma_{\rm T} c}. \tag{3.2}$$

Here $m_{\rm p}$ is the proton mass, $\sigma_{\rm T}$ is the Thomson cross-section and $\epsilon_{\rm r}$ is the radiative efficiency assumed to be a fixed value of 0.1, adopted from the mean value for radiatively efficient Shakura

& Sunyaev (1973) accretion onto a Schwarzschild black hole. The accretion rate in the standard models is then $\dot{M}_{\rm acc} = \min(\dot{\rm M}_{\rm B}, \dot{\rm M}_{\rm edd})$ with no additional requirement that accreted particles be gravitationally bound to the central black hole.

In the thermal feedback model (e.g. Springel et al., 2005b; Di Matteo et al., 2005; Sijacki et al., 2007; Johansson et al., 2009a), the feedback energy from the black hole $E_{\rm feed}$ has typically been assumed to be some fraction $\epsilon_{\rm f}$ of the rest mass energy of the accreted matter and couples thermally and isotropically to the surrounding gas as,

$$\dot{E}_{\rm feed} = \epsilon_{\rm w} \dot{M}_{\rm inf} c^2. \tag{3.3}$$

A fixed value of $\epsilon_{\rm w} = 0.005$ is adopted in many previous studies (Springel et al., 2005b; Sijacki et al., 2007), so that 0.5 percent of the total accreted rest mass energy is available as thermal energy which is distributed to the neighboring $\sim 64$ gas particles weighted by the SPH kernel. In this approach, neither mass nor momentum is added to the ambient fluid by the black hole and all accretion energy is added via thermal energy.

### 2.4 The new mechanical black hole feedback model

For the simulations with mechanical feedback from the AGN we use the model presented in CONJ12 which is briefly reviewed in this section. We first calculate the rate of the mass infall onto the black hole with an "alternative averaging (AA)" method using:

$$\dot{M}_{\rm inf,AA} = \left\langle \frac{4\pi\alpha G^2 M_{\rm BH}^2 \rho}{(c_{\rm s}^2 + v^2)^{3/2}} \right\rangle, \tag{3.4}$$

where angle brackets denote the averaging over the SPH kernel. This method for the calculation of the black hole mass does the calculation in both time and space on an individual particle basis and then averages the results over the neighboring 64 particles in order to reduce the dependency on the number of SPH particles.

To avoid the unphysical accretion of unbound gas from outside the Bondi radius we statistically limit the accretion of mass to the gas within the Bondi radius. Since the mass distribution of each gas particle is smoothed with the kernel size, we allow for the full accretion rate only if the total volume of a gas particle resides within the Bondi radius. Otherwise, we reduce the probability of being absorbed by the black hole (soft Bondi radius criterion (SB), see CONJ12). To account for the time that it takes a particle at radius $r_j$ to be accreted, we include the free-fall modification (FF) to the accretion probability with an extra factor of

$$p_{j,\mathrm{ff}} = \frac{\frac{1}{\tau_j}}{\frac{1}{N_{\mathrm{sph}}} \sum_{j=1}^{N_{\mathrm{sph}}} \frac{1}{\tau_j}}, \tag{3.5}$$

where $\tau_j = r_j/(c_{\mathrm{s},j}^2 + v_j^2)^{1/2}$ is the free fall time and $N_{\mathrm{sph}}$ denotes the typical number of smoothing neighboring gas particles of the black hole. For a full description of the soft Bondi radius criterion and the free-fall modification, see Figure 1 and section 2.4 of CONJ12.

Motivated by observations of broad absorption line winds, which convey energy, mass and momentum into the surrounding gas with velocity $\sim 10,000$ km s$^{-1}$ outflows corresponding to a typical broad line wind velocity (Crenshaw et al., 2003; Moe et al., 2009; Dunn et al., 2010), we included these observed AGN winds in our numerical treatment following Ostriker et al. (2010). In our model, the AGN winds carry a mass given by:

$$\dot{M}_{\mathrm{outf}} = \dot{M}_{\mathrm{inf}} - \dot{M}_{\mathrm{acc}}, \tag{3.6}$$

where $\dot{M}_{\mathrm{outf}}$, $\dot{M}_{\mathrm{inf}}$ and $\dot{M}_{\mathrm{acc}}$ respectively denote the outflowing/inflowing mass rate and the mass rate actually accreted onto the black hole. For simplicity we assume that the wind is launched at a fixed speed $v_{\mathrm{w}} = 10,000$ km s$^{-1}$. Then a momentum flux carried by the wind is given as,

$$\dot{p} = \dot{M}_{\mathrm{outf}} v_{\mathrm{w}}, \tag{3.7}$$

and the kinetic energy rate of the outflow is given as,

$$\dot{E}_{\rm w} \equiv \epsilon_{\rm w}\dot{M}_{\rm acc}c^2, \tag{3.8a}$$

$$= \frac{1}{2}\dot{M}_{\rm outf}v_{\rm w}^2, \tag{3.8b}$$

where $\epsilon_{\rm w}$ denotes the feedback efficiency. We can define the dimensionless quantity $\psi$, the ratio of the mass outflow rate to the accreted rate as,

$$\psi \equiv 2\epsilon_{\rm w}c^2/v_{\rm w}^2 = \dot{M}_{\rm outf}/\dot{M}_{\rm acc}, \tag{3.9}$$

and we can rewrite the equation for the black hole accretion rate as,

$$\dot{M}_{\rm acc} = \dot{M}_{\rm inf}\frac{1}{1+\psi}. \tag{3.10}$$

As discussed in Ostriker et al. (2010) and CONJ12, in the presence of significant AGN winds, not all of the mass entering the central region $\dot{M}_{\rm inf}$ actually reaches the black hole. For example, with the feedback efficiency typically adopted in the literature, $\epsilon_{\rm w} = 0.005$, and with the fixed wind velocity $v_{\rm w} = 10,000$ km s$^{-1}$, only 10 percent of the inflowing mass is actually accreted onto the black hole while 90 percent is ejected in a wind.

We calculate the dimensionless quantity $\psi$ for the given feedback efficiency $\epsilon_{\rm w}$ and wind velocity $v_{\rm w}$, and stochastically select the wind particles from all gas particle attracted into the central zone by the black hole keeping the fraction of wind particles to the total inflowing particles as $\psi/(1+\psi)$. To deposit the wind mass and momentum, we give kicks to the gas particles selected following the stochastic approach. We set the direction of the wind to be parallel or anti-parallel to the direction of angular momentum of each gas particle, if the central black holes are surrounded by a gas disk this procedure results in a wind perpendicular to the disk plane (Proga & Kallman, 2004). The emitted wind particles share their momentum with two other nearby gas particles to reproduce the shock heated momentum-driven flows. We deposit the residual energy into these three particles in thermal form so that the total energy is conserved.

In addition to the mechanical feedback described above, X-ray radiation from the accreting black hole can be coupled to the surrounding gas according to an approximation described in Sazonov et al. (2005), as in Ciotti et al. (2010); Novak et al. (2011); CONJ12. The luminosity flux from the two black holes is calculated at the position of each gas particle, and the flux is converted to the net volume heating rate $\dot{E}$ by adopting the Sazonov et al. (2005) formulae that include Compton heating and photoionization heating. Note that Equation 4.7, not Equation 4.1, determines the AGN luminosity flux and thus the magnitude of the radiation feedback. We also include the electromagnetic momentum, the radiation pressure from the X-ray flux from the black hole by adding a momentum per unit time of $\dot{p} = \dot{E}/c$. The added force is directed radially away from the black holes.

Finally, instead of limiting the maximum accretion rate to the Eddington rate (Equation 3.2), we compute the Eddington force acting on the surrounding gas particles, directed radially away from the black hole as described in CONJ12 and allow this force to act on the gas flow through the hydrodynamic equations. Naturally it reduces the inflow and increases the outflow but accretion exceeding the Eddington rates can occasionally occur.

## 3 Comparison of Thermal and Mechanical Feedback models

We explore the effects of AGN feedback with three types of simulations: no black hole and AGN feedback (No-AGN); thermal AGN feedback (Th-AGN); and momentum-based mechanical and radiation AGN feedback with X-ray heating and radiation pressure (MR-AGN). All equal and unequal-mass mergers are run with identical merger orbits and initial disk orientations. The simulated final black hole properties and galaxy remnant properties are given in Table **??** and 3.2, respectively. Note that we use the model for modified black hole mass accretion (Section 2.4) only for the MR-AGN models, the momentum-based mechanical AGN feedback. The number following the model acronyms indicates the assumed feedback efficiency in units of $10^{-4}$, i.e. Th-AGN-50 is the thermal feedback model with a feedback efficiency of $\epsilon_{\rm f} = 5 \times 10^{-3}$; MR-AGN-05 is the mechanical feedback model with a feedback efficiency of $\epsilon_{\rm f} = 5 \times 10^{-4}$ (see Table **??**). The model

Table 3.1: The simulated merger sample: black hole properties

| Model | Mass Ratio | $\epsilon_{\rm w}{}^a$ | log $M_{\rm BH,f}$ $M_\odot$ | $l_{\rm max}^{\rm BH,eff\,b}$ | $l_{\rm min}^{\rm BH,eff}$ | $\sigma_{\rm fluc}{}^c$ | log $E_{\rm BH}{}^d$ erg |
|---|---|---|---|---|---|---|---|
| (1) | (2) | (3) | (4) | (5) | (6) | (7) | (8) |
| No-AGN | 1:1 | - | - | - | - | - | - |
| Th-AGN-50[e] | 1:1 | $5\times10^{-3}$ | 7.89 | -0.70 | -5.98 | 0.27 | 59.84 |
| Th-AGN-20 | 1:1 | $1\times10^{-3}$ | 8.45 | -0.70 | -4.66 | 0.25 | 59.70 |
| Th-AGN-05 | 1:1 | $5\times10^{-4}$ | 8.63 | -0.70 | -5.44 | 0.18 | 59.58 |
| MR-AGN-50 | 1:1 | $5\times10^{-3}$ | 7.83 | 0.70 | -4.30 | 6.00 | 59.79 |
| MR-AGN-20[f] | 1:1 | $2\times10^{-3}$ | 7.95 | 1.34 | -6.19 | 4.77 | 59.51 |
| MR-AGN-05 | 1:1 | $5\times10^{-4}$ | 8.95 | 1.63 | -4.58 | 4.90 | 59.91 |
| Th-AGN-50-2:1 | 2:1 | $5\times10^{-3}$ | 6.94 | -0.70 | -3.98 | 5.88 | 59.20 |
| Th-AGN-50-3:1 | 3:1 | $5\times10^{-3}$ | 6.80 | -0.70 | -4.54 | 5.30 | 59.01 |
| Th-AGN-50-6:1 | 6:1 | $5\times10^{-3}$ | 6.63 | -0.70 | -4.04 | 4.21 | 58.77 |
| MR-AGN-20-2:1 | 2:1 | $2\times10^{-3}$ | 7.65 | -0.21 | -7.91 | 5.88 | 59.20 |
| MR-AGN-20-3:1 | 3:1 | $2\times10^{-3}$ | 7.46 | -0.28 | -9.31 | 5.30 | 59.01 |
| MR-AGN-20-6:1 | 6:1 | $2\times10^{-3}$ | 7.22 | -0.79 | -3.90 | 4.21 | 58.77 |

[a] AGN feedback efficiency
[b] $l^{\rm BH,eff} \equiv \log(L_{\rm BH}^{\rm eff}/L_{\rm Edd})$ where $L_{\rm BH,opt}^{\rm eff}$ is the BH luminosity in the optical band after absorption, i.e., as it will be seen from infinity. The maximum and minimum Eddington rates are listed in column (5) and (6) respectively.
[c] The fluctuation level of the mass accretion measured following Equation 3.11 after the final coalescence of black hole.
[d] Total black hole feedback energy distributed throughout the total simulation time.
[e] Thermal feedback model with commonly adopted feedback efficiency $\epsilon_{\rm w} = 5\times10^{-3}$ (e.g. Springel et al., 2005b).
[f] Our fiducial model with momentum and radiation AGN feedback with modified black hole mass accretion and feedback efficiency $\epsilon_{\rm w} = 2\times10^{-3}$.

Th-AGN-50 is identical to the black hole accretion and AGN feedback model described in Springel et al. (2005b).

### 3.1 Black hole growth and star formation rate

Figure 3.1 shows the global star formation rate, the net accretion rate onto the black hole, the Eddington ratio of the mass accretion ($\dot{M}_{\rm acc}/\dot{M}_{\rm Edd}$) and the evolution of the black hole mass (summed over both black holes prior to merging) for the three different feedback models: No-AGN (black curve), Th-AGN-50 (e.g., Springel et al., 2005b, blue curves), and MR-AGN-20 (red curves). Note that the thermal feedback model Th-AGN-50 adopts a feedback energy

Table 3.2: The simulated merger sample: Galaxy properties

| Model | Mass Ratio | $\epsilon_{\rm w}$ | $\sigma_{\rm bul,f}$ [a] km s$^{-1}$ | $R_{\rm eff}$ kpc | log $L_{\rm X}$ [b] erg s$^{-1}$ | log $M_{\rm wind}$ [c] $M_\odot$ | log $E_{\rm wind}$ [c] erg | log $L_{\rm kin}$ [d] erg s$^{-1}$ | log $M_*$ [e] $M_\odot$ | log $E_{\rm SN}$ [f] erg |
|---|---|---|---|---|---|---|---|---|---|---|
| (1) | (2) | (3) | (4) | (5) | (6) | (7) | (8) | (9) | (10) | (11) |
| No-AGN | 1:1 | - | 199.9 | 1.14 | 39.16 | 10.03 | 58.55 | 41.34 | 10.30 | 59.57 |
| Th-AGN-50 | 1:1 | $5\times10^{-3}$ | 187.6 | 1.32 | 39.75 | 9.53 | 57.99 | 40.67 | 10.23 | 59.50 |
| Th-AGN-20 | 1:1 | $2\times10^{-3}$ | 180.7 | 1.37 | 38.80 | 9.42 | 57.99 | 40.65 | 10.22 | 59.49 |
| Th-AGN-05 | 1:1 | $5\times10^{-4}$ | 172.7 | 1.51 | 38.39 | 9.40 | 58.10 | 38.97 | 10.18 | 59.45 |
| MR-AGN-50 | 1:1 | $5\times10^{-3}$ | 182.4 | 1.30 | 39.30 | 9.48 | 58.67 | 41.56 | 10.18 | 59.44 |
| MR-AGN-20 | 1:1 | $2\times10^{-3}$ | 171.8 | 1.55 | 38.24 | 9.42 | 58.54 | 38.37 | 10.09 | 59.36 |
| MR-AGN-05 | 1:1 | $5\times10^{-4}$ | 155.7 | 1.97 | 36.66 | 9.54 | 58.65 | 40.10 | 10.06 | 59.33 |
| Th-AGN-50-2:1 | 2:1 | $5\times10^{-3}$ | 139.9 | 1.48 | 41.07 | 9.60 | 57.82 | 40.02 | 9.97 | 59.24 |
| Th-AGN-50-3:1 | 3:1 | $5\times10^{-3}$ | 126.4 | 1.54 | 40.84 | 9.51 | 57.83 | 39.04 | 9.85 | 59.12 |
| Th-AGN-50-6:1 | 6:1 | $5\times10^{-3}$ | 120.3 | 1.52 | 40.50 | 9.26 | 57.56 | 39.40 | 9.73 | 59.00 |
| MR-AGN-20-2:1 | 2:1 | $2\times10^{-3}$ | 132.5 | 1.80 | 36.63 | 9.51 | 58.36 | 41.21 | 9.79 | 59.06 |
| MR-AGN-20-3:1 | 3:1 | $2\times10^{-3}$ | 123.6 | 1.76 | 37.48 | 9.05 | 58.14 | 41.12 | 9.70 | 58.97 |
| MR-AGN-20-6:1 | 6:1 | $2\times10^{-3}$ | 119.5 | 1.58 | 37.50 | 8.70 | 57.81 | 41.05 | 9.67 | 58.94 |

[a] Initial value of pre-merger primary galaxy $\sigma_{\rm ini}\sim 105$ km s$^{-1}$.
[b] X-ray luminosity measured in 0.3-8 KeV band.
[c] Total amount of ISM mass lost and wind kinetic energy measured at r =5 kpc from the galactic centre after the final black hole coalescence.
[d] Mechanical luminosity $L_{\rm wind}\equiv\dot{M}_{\rm wind}v^2_{\rm wind}/2$ averaged over 0.2 Gyr by the end of the model evolution.
[e] Total amount of star formed during the model evolution.
[f] Total supernova feedback energy distributed during the model evolution.

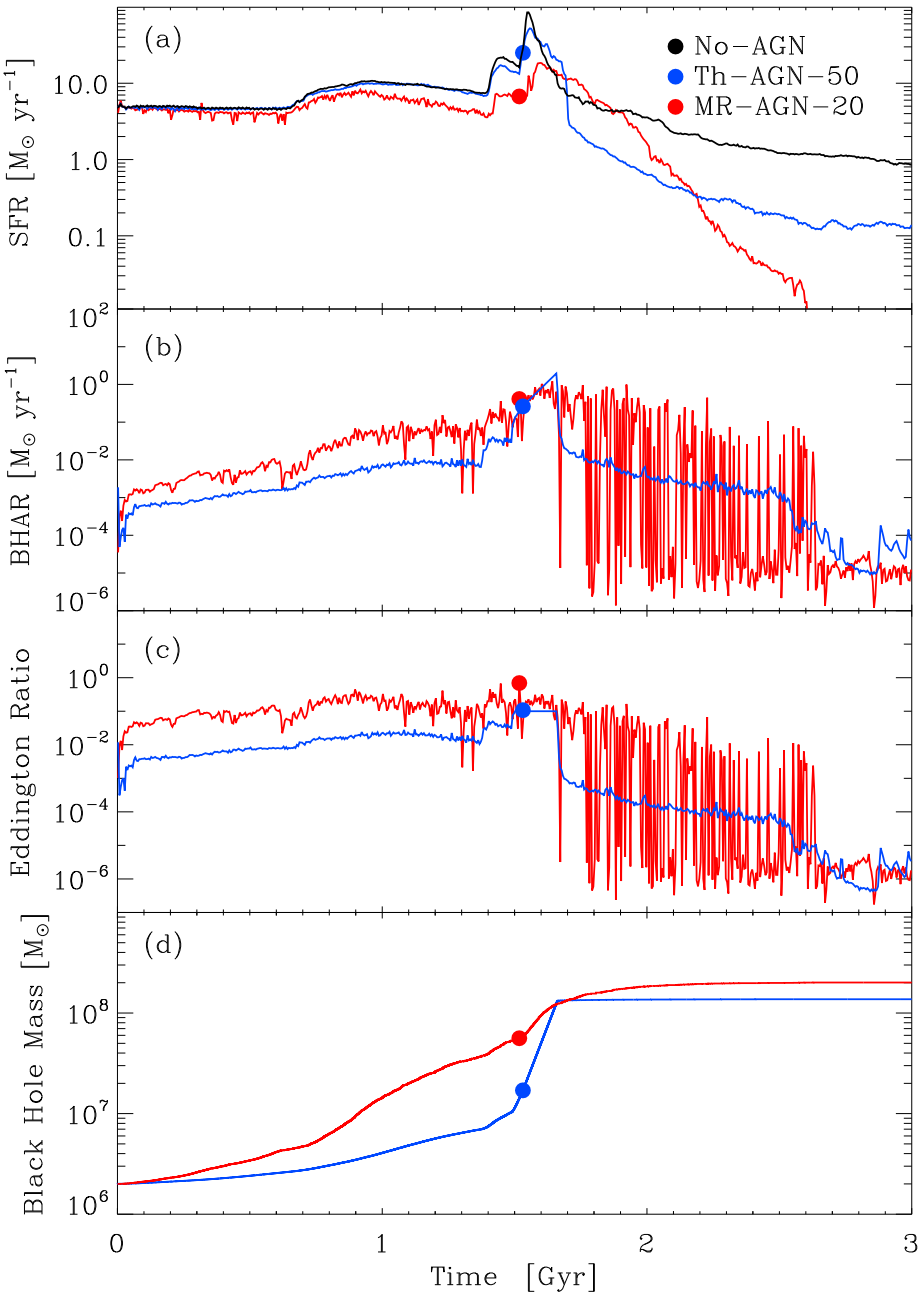



Figure 3.1: Comparison of the feedback models with a major merger of two galaxies: no AGN (black), thermal feedback (blue), and momentum and radiation feedback (red). (a) Evolution of the total star formation rate, (b) the total accretion rate onto the black hole, (c) the Eddington ratio of the mass accretion ($\dot{M}_{\rm BH}/\dot{M}_{\rm Edd}$), and (d) the evolution of the black hole mass are shown as a function of time. The filled circles indicate the time of black hole merger. Note that the model outputs are smoothed identically to have equal time bin $\Delta t = 5$ Myr.

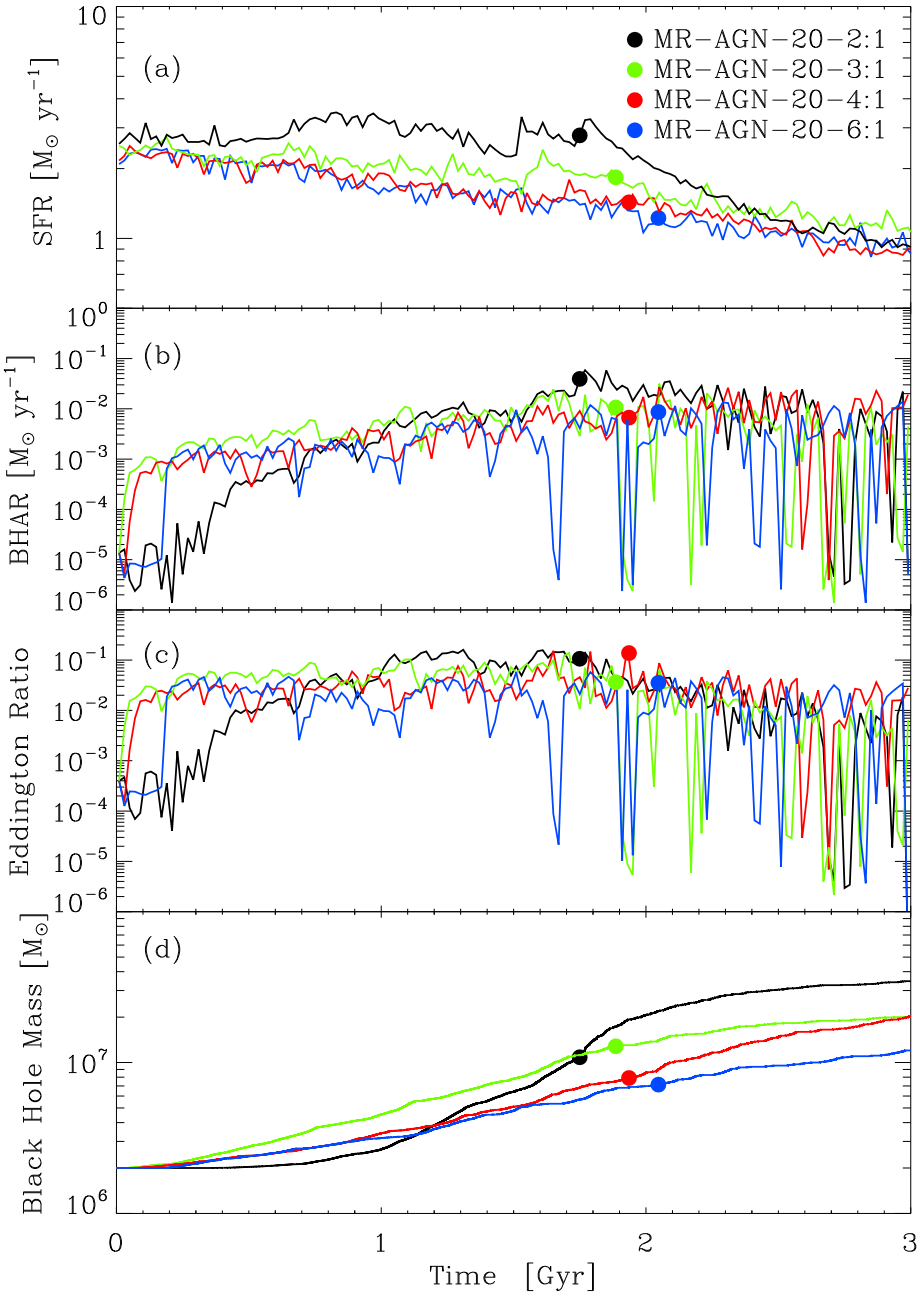



Figure 3.2: (a) The total star formation rate, (b) the total accretion rate onto the black hole, (c) the Eddington ratio of the mass accretion ($\dot{M}_{\rm BH}/\dot{M}_{\rm Edd}$), and (d) the evolution of the black hole mass as a function of time for 2:1 (black), 3:1 (green), 4:1 (red), and 6:1 (blue) mergers with the mechanical and radiation AGN feedback. The filled circles indicate the time of black hole merger. The model outputs are smoothed identically to have equal time bin $\Delta t = 20$ Myr.

coupling efficiency of $\epsilon_{\rm w} = 5 \times 10^{-3}$, the value adopted in Springel et al. (2005b) and the MR-AGN-20 adopts $\epsilon_{\rm w} = 2 \times 10^{-3}$. We decided to compare these two models as they result in merger remnants with comparable final black hole mass (see Fig. 3.1).

Figure 3.1(a) shows that the inclusion of the AGN feedback in mechanical form reduces the star formation rate before and at the coalescence of the two galaxies at $t \sim 1.5$ Gyr. After the encounter, both AGN feedback models have lower star formation rate compared to the no black hole model (Springel et al., 2005b). The star formation is more efficiently terminated by the MR-AGN feedback. Total amount of stars formed and the total supernova feedback energy distributed during the model evolution for all models are listed in Column (10) and (11) of Table 3.2. The total amount of stars formed and the corresponding supernovae feedback energy are reduced by 40% in MR-AGN-20 compared to No-AGN.

Figures 3.1(b) and (c) show the total black hole accretion rates and the Eddington ratios, respectively. In the Th-AGN-50 model, the black hole mass accretion rate increases rapidly during the encounter and final coalescence. In a short time the black hole grows by an order of magnitude reaches its final mass to within a factor of a few (Figure 3.1(d)). Afterwards, the accretion rates are low with Eddington ratios slowly decreasing from $\dot{M}_{\rm BH}/\dot{M}_{\rm Edd} \sim 10^{-4}$ to $10^{-5}$. For the MR-AGN-20 model, accretion rates are much more variable with short episodes of efficient accretion even after the black hole coalescence reaching $\dot{M}_{\rm BH}/\dot{M}_{\rm Edd} \geq 0.1$ (Figure 3.1(c)). In order to quantify the fluctuation level of black hole mass accretion for each model, we define a fluctuation parameter $\sigma_{\rm fluc}$ as,

$$\sigma^2_{\rm fluc} \equiv \left\langle (l_{\rm 1Myr} - l_{\rm 50Myr})^2 \right\rangle, \tag{3.11}$$

where $l_{\rm 1Myr}$ denotes the logarithmic Eddington ratio of black hole mass accretion measured in time bins of one Myr, and $l_{\rm 50Myr}$ is the smoothed Eddington ratio measured in 50 Myr time bins as $l_{\rm 50Myr} = \log(\left\langle \dot{M}_{\rm BH} \right\rangle_{\Delta t=50{\rm Myr}} / \dot{M}_{\rm Edd})$. We determine the global fluctuation level in the Eddington ratio by averaging over all one Myr bins after the black hole merger. The calculated fluctuation parameters $\sigma_{\rm fluc}$ are listed in Column (7) in Table **??**. The fluctuation level of mass accretion in MR-AGN-20 is $\sim 4.7$, which is significantly larger than for all Th-AGN models ($\sim 0.2$). Despite

the dramatic differences in the time dependence of the accretion rates (cf. Figure 3.1(b) and (c)), the final black hole masses in the two cases are quite similar (Figure 3.1(d)).

We now proceed to study the star formation histories and the black hole accretion histories for mergers with varying mass ratios. We ran four mergers with mass ratios of 2:1, 3:1, 4:1 and 6:1 on similar orbits (G13) as the equal mass-merger, adopting the MR-AGN feedback model. In Figure 3.2, we show the evolution of (a) the resulting star formation rates, (b) the total black hole accretion rates, (c) the Eddington ratios, and (d) the total black hole mass for the four minor mergers as a function of time. Note that we smooth the model outputs shown in Figure 3.2 with longer time step ($\Delta t = 20$ Myr) than in Figure 3.1 ($\Delta t = 5$ Myr) to give the overall mean evolution. Surprisingly, almost independent of the progenitor mass-ratio the combined star formation rates are only mildly decreasing from 2 $M_{\odot}$/yr to 1 $M_{\odot}$/yr over 3 Gyrs with only a mild peak in the 2:1 case during the coalescence. The dependence of mass the mass-ratio is even weaker here than for thermal feedback models (Johansson et al., 2009b) as we include hot gaseous halos which constantly supply gas (Moster et al., 2011, 2012). A similar weak evolution and weak trend with mass-ratio is found for the the black hole accretion rates and the Eddington ratios (Figure 3.2 (b) and (c)). In all cases, the black hole accretion rates are variable with the Eddington ratios ranging from $10^{-6}$ to 0.1 (Note the maximum ratio for equal-mass mergers is about unity) as shown in Figure 3.2(c). The evolution of the black hole accretion rates are mirrored in the growth of the black hole masses, with the final black hole masses being slightly lower in remnants of higher mass-ratio mergers.

### 3.2 Properties of the post merger gas outflow

In this section we investigate the physical properties of the gas outflow from the central parts of the galaxies produced by the three feedback models. As detailed before, the energy injection conditions near the black hole in the mechanical and the thermal model are quite different. In the MR-AGN model, gas surrounding the black hole is ejected in a wind with an initial velocity of $\sim 10,000$ km s$^{-1}$ (Ostriker et al., 2010, CONJ12). On the other hand the thermal heating from

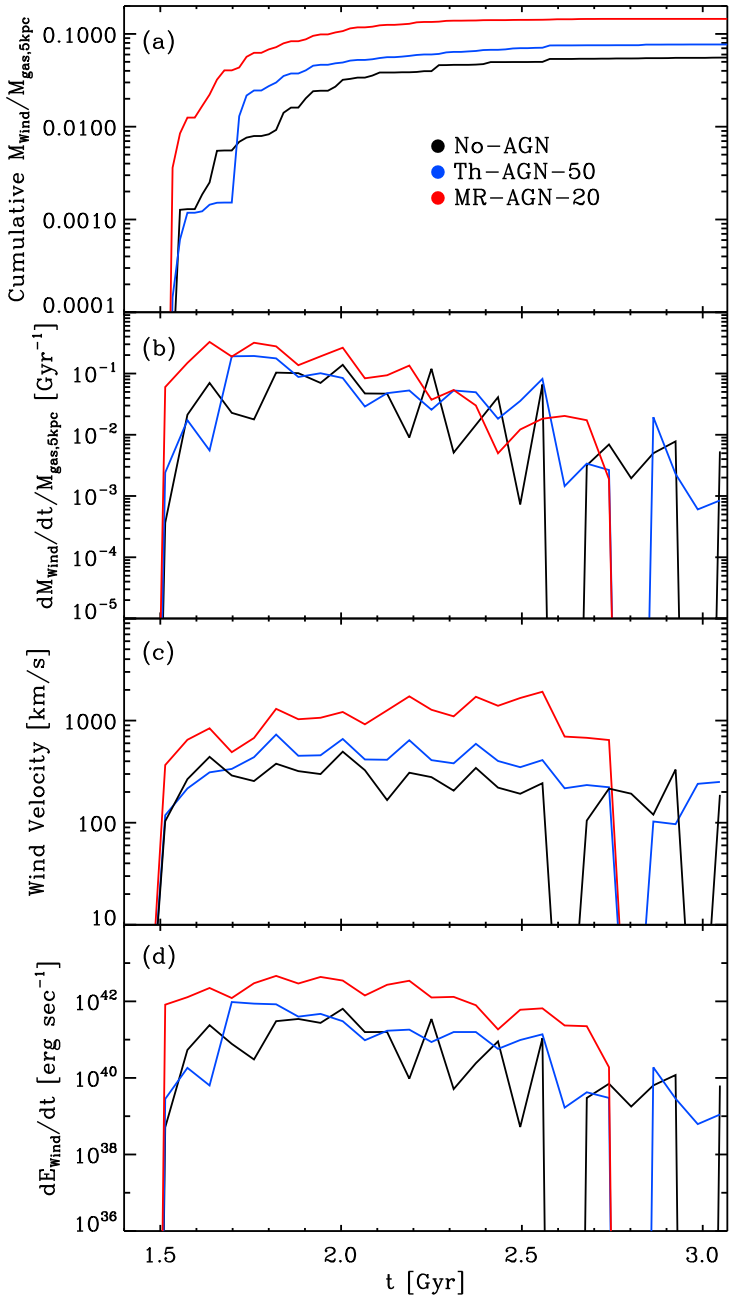



Figure 3.3: The properties of the outflowing gas in three feedback models: No-AGN, Th-AGN-50, and MR-AGN-20. (a) the fraction of mass depleted by wind within a central sphere with a fiducial galactocentric radius of $r = 5$ kpc after the final black hole coalescence, (b) the specific outflowing mass loss rate, i.e., the rate of gas mass loss normalized by the total amount of gas left in the central region of the galaxy at the final black hole coalescence, (c) outflowing gas velocities and (d) the corresponding mechanical luminosities are shown.

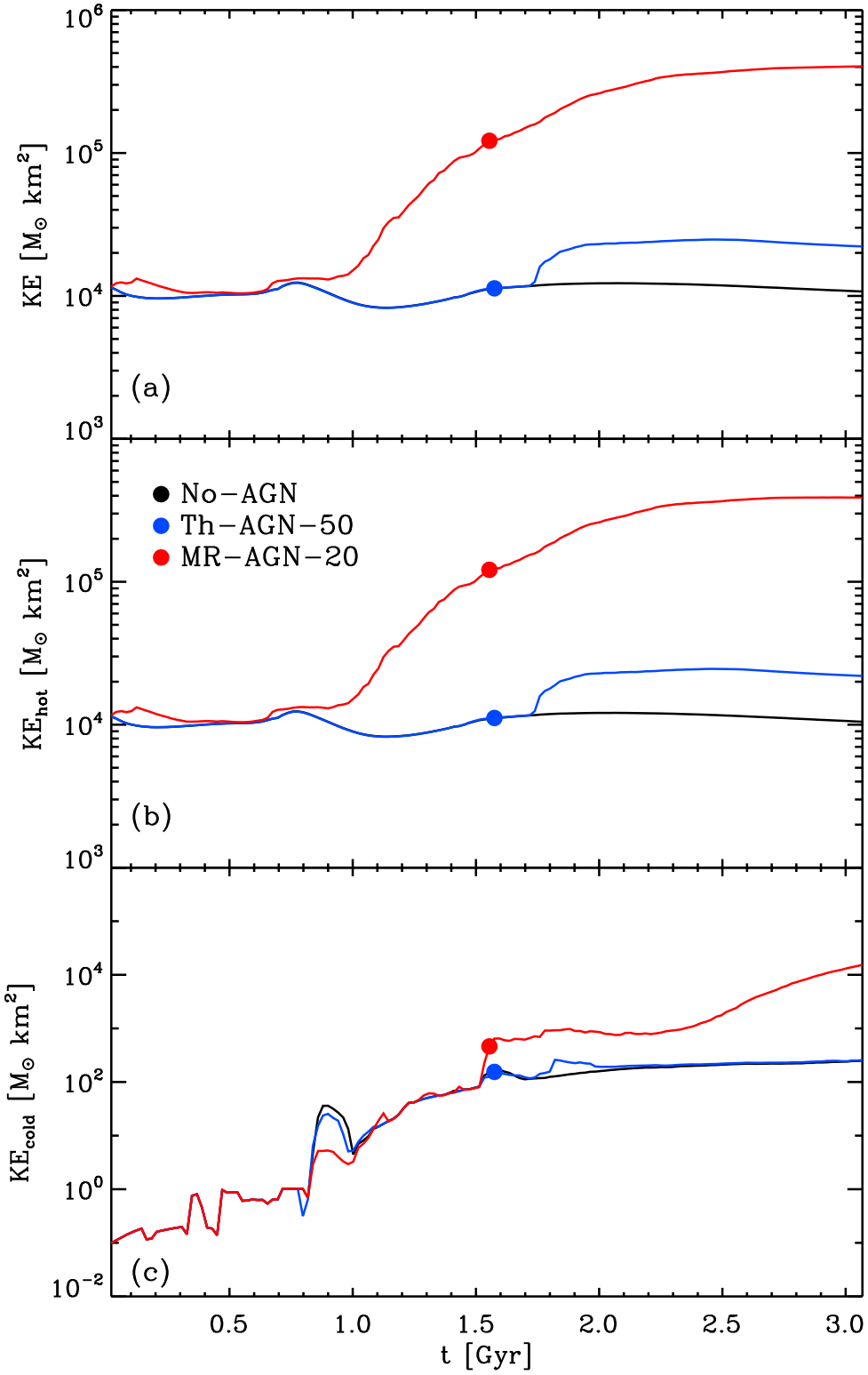



Figure 3.4: (a) Total kinetic energy of the gas, (b) the kinetic energy of the warm gas with $T > 10^{4.5}$ K, and (c) the kinetic energy of the cold gas with $T < 10^{4.5}$ K in the outer region of the galaxy ($r > 20$ kpc) are shown for the three feedback models: No-AGN, Th-AGN-50, and MR-AGN-20.

the accreting black hole in the Th-AGN model drives slow and hot outflows in the vicinity of the black hole as shown in Springel et al. (2005b).

To parametrize the cumulative mass outflow from the central parts of the merger remnants we measure the fraction of gas mass leaving a central sphere with a fiducial galactocentric radius of $r = 5$ kpc after the final black hole coalescence. We also measure the instantaneous outflow rate and the velocity of the outflowing gas. With this we calculate a corresponding mechanical luminosity as $L_{\rm wind} \equiv \dot{M}_{\rm wind} v^2_{\rm wind}/2$, i.e., the kinetic energy carried away by the outflowing gas.

The temporal evolution of the outflowing gas properties (the cumulative outflowing gas mass leaving a central region normalized by the total amount of gas in the central region at the final black hole coalescence, the specific outflow rate, i.e., the rate of gas mass loss normalized by the total amount of gas left at the final black hole coalescence, outflow velocity and mechanical luminosity) after the final black hole coalescence at $t \sim 1.5$ Gyr of the No-AGN model and our fiducial AGN feedback models Th-AGN-50 and MR-AGN-20 are shown in Figure 3.3.

The MR-AGN-20 model depletes the gas in the central region of the galaxy most effectively and loses the largest fraction of gas after the merger, i.e., $\sim 15$ % of gas leaves a central sphere by outflow (Figure 3.3(a)). The model without black hole also loses the large amount of gas after the merger, primarily driven by the merger induced shock and star formation, but the fraction of outflowing gas mass to the total gas mass within a central sphere is smaller compared to the AGN feedback models.

The corresponding specific outflowing mass loss rates are shown in Figure 3.3(b). The MR-AGN-20 model has the highest rate, especially after the merger with the timescale for gas depletion by outflow of $\tau_{\rm depletion} \sim 2.9$ Gyr. At later times the specific outflowing mass loss rate for the mechanical AGN model drops and becomes comparable to other models.

The MR-AGN-20 model also shows the highest outflow velocities of $v_{\rm w} \sim 800 - 1500$ km s$^{-1}$ (Figure 3.3(c)). These values are comparable to recent observations which indicate outflow velocities in the range of 700 km/s to 3000 km/s (Fischer et al., 2011; Pounds & Vaughan, 2011; Sturm et al., 2011; Müller-Sánchez et al., 2011; Rupke & Veilleux, 2013). The velocities in the

thermal AGN model are much lower and do not exceed the $400 - 500$ km s$^{-1}$ which are comparable to the velocity of the shock heated gas in the No-AGN model.

The mechanical luminosities of the outflowing gas for the three models are shown in Figure 3.3(d). Overall, Th-AGN-50 has lower mechanical luminosity $L_{\rm wind} \sim 10^{41}$ erg/s, mainly because of its slow outflow velocity. The MR-AGN-20 with momentum feedback has mechanical luminosities a factor of 5-10 higher than the thermal feedback. The total kinetic energy carried away by the winds, i.e., the mechanical luminosities integrated over the simulation time after the merger for the Th-AGN-50 model is $\Delta E_{\rm wind} \sim 1.94 \times 10^{58}$ ergs, while the MR-AGN-20 model deposits $\Delta E_{\rm wind} \sim 6.89 \times 10^{58}$ ergs (3.6 times larger) into the ISM within 1.5 Gyrs.

The outflowing gas removed from the central region would propagate to the outer region of the galaxy and increase the kinetic energy of the gas component. Figure 3.4(a) shows the total kinetic energy of the gas in the outer region of the galaxy ($r > 20$ kpc). In the MR-AGN-20, the bulk of mass and kinetic energy are dissipated by the strong outflowing gas from the AGN and located in the outer part of the galaxy. The Th-AGN-50 also distributes increased kinetic energy in the outer part, especially right after the final coalescence of the black holes, but the increment is much smaller compared to the MR-AGN model with the strong AGN-induced winds. The total kinetic energy in the outflow, as seen in Figure 3.4(a), is a factor of 20 higher in the MR-AGN then in the Th-AGN case. While the kinetic energy in the outer region of the galaxy is dominated by the warm component with the temperature $T > 10^{4.5}$ K, as shown in Figure 3.4(b), the MR-AGN model also sweeps up and drives out cold gas increasing the kinetic energy of the cold component with $T < 10^{4.5}$ K (see Figure 3.4(c)). The Th-AGN model, however, has almost no effect on the cold gas component.

# 4 Properties of merged galaxies

## 4.1 Distribution of gas during the merger

Figure 3.5 shows a sequence of snapshots of the mass-weighted average gas temperature along the line of sight during a merger of Th-AGN-50 (top) and MR-AGN-20 (bottom). The snapshots

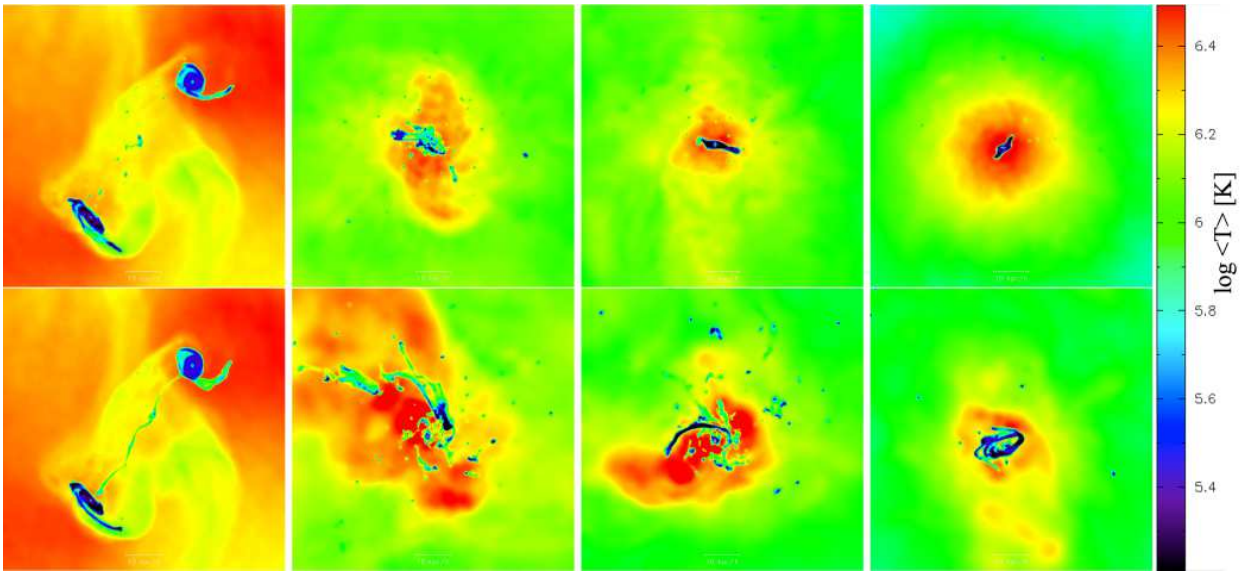



Figure 3.5: A sequence of snapshots of the mass-weighted gas temperature during a major merger of two models: Th-AGN-50 (top panels) and MR-AGN-20 (bottom panels). The snapshots after the first close passage of the two galaxies at $t = 0.92$ Gyr, right after the galaxies and black holes merge at $t = 1.78$ Gyr, and afterwards at $t = 2.0$, 2.64 Gyr are shown from left to right. The images are 80 kpc on a side and redder color indicates a higher temperature.

show the first close passage at $t = 0.92$ Gyr, the time right after the final coalescence at $t = 1.78$ Gyr and afterwards at $t = 2.0$, and 2.64 Gyr from left to right. In the MR-AGN-20 model, gas is dissipated by the AGN-induced outflow while the bulk of hot gas still remains by the end of the simulation in the Th-AGN-50 model.

### 4.2 X-ray properties

We compare the evolution of hot gas and X-ray emission of the No-AGN and two feedback models. Following Cen et al. (1995), we calculate the X-ray luminosity due to bremsstrahlung radiation as well as line emissions of all the species using the computed X-ray emissivity spectra tables, kindly made available to us by R. Cen. The emission rates from H, He and metals are given separately assuming that the gas is in ionization equilibrium and optically thin. We calculate the total emissivity by summing the emission rates of the all components weighted by the relative abundance assuming solar abundance. Then we compute the integrated luminosity

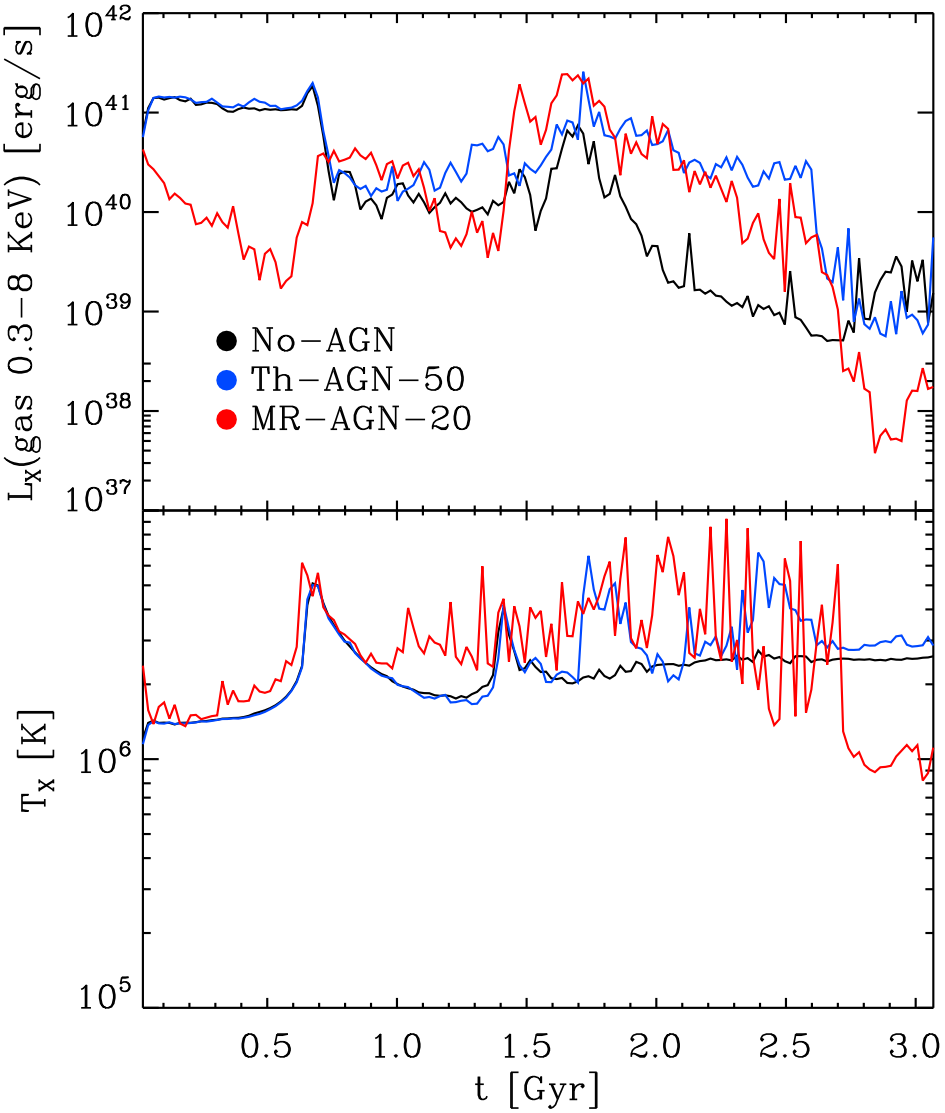



Figure 3.6: Galactic X-ray coronal luminosity $L_X$ (top), and the X-ray luminosity-weighted temperature of the hot and diffuse gas component with a temperature of $T \geq 10^6$ K, and a density $\rho \leq 3.16 \times 10^{-3} M_\odot$ pc$^{-3}$ (bottom).

for 0.3-8 keV band using the computed total emissivity. We assume that the central region of the galaxy remains obscured because of the large column density of intervening gas and dust, therefore we only include the X-ray contribution from hot and diffuse gas particles. Following Cox et al. (2006), we define the 'hot and diffuse gas' with a temperature of $T \geq 10^6$ K, and a density $\rho \leq 3.16 \times 10^{-3} M_{\odot} \mathrm{pc}^{-3}$, which corresponds to the critical density for star formation, so effectively we exclude star forming gas.

Figure 3.6 shows the X-ray luminosities for photons with energies of 0.3-8 keV for No-AGN, Th-AGN-50 and MR-AGN-20 as a function of time. Before the galaxy interaction, the majority of the X-ray emission is produced by pre-existing hot halo gas, but in the MR-AGN-20 model, the high velocity gas outflow by AGN momentum feedback effectively drives out the gaseous halo, lowering the X-ray luminosity. The system begins to emit more X-rays at the first interaction of galaxies at $\sim 0.7$ Gyr, in shocks that lie directly between the two disks. During the galaxy interaction, the majority of the X-ray emission is produced by shock-heated gas, as Th-AGN-50 shows very similar X-ray luminosity compared to No-AGN model. By the time of the final coalescence, $t \sim 1.5$ Gyr, however, the X-ray luminosity increases in both AGN models. In the Th-AGN-50 model, the X-ray luminosity decreases much more slowly as the black hole keeps depositing a significant amount of thermal energy, sustaining a hot X-ray emitting dense gaseous halo (see Figure 3.5 upper-right panel). On the other hand, in the mechanical feedback model, the hot gas in the remnant is driven outwards more effectively and the X-ray luminosity decreases quickly. The final X-ray emission of the Th-AGN-50 is higher ($1.6 \times 10^{39}$ erg s$^{-1}$) compared with the observed luminosity (0.3-8 KeV) of the galaxies with corresponding velocity dispersions. The MR-AGN-20 model, however, results in lower X-ray luminosity ($9.8 \times 10^{37}$ erg s$^{-1}$) that better reproduces observed values.

### 4.3 Galaxy-black hole Scaling relation

We now proceed with a detailed analysis of the effect of the black hole feedback prescription and feedback efficiency on the final mass of black holes and the corresponding stellar velocity

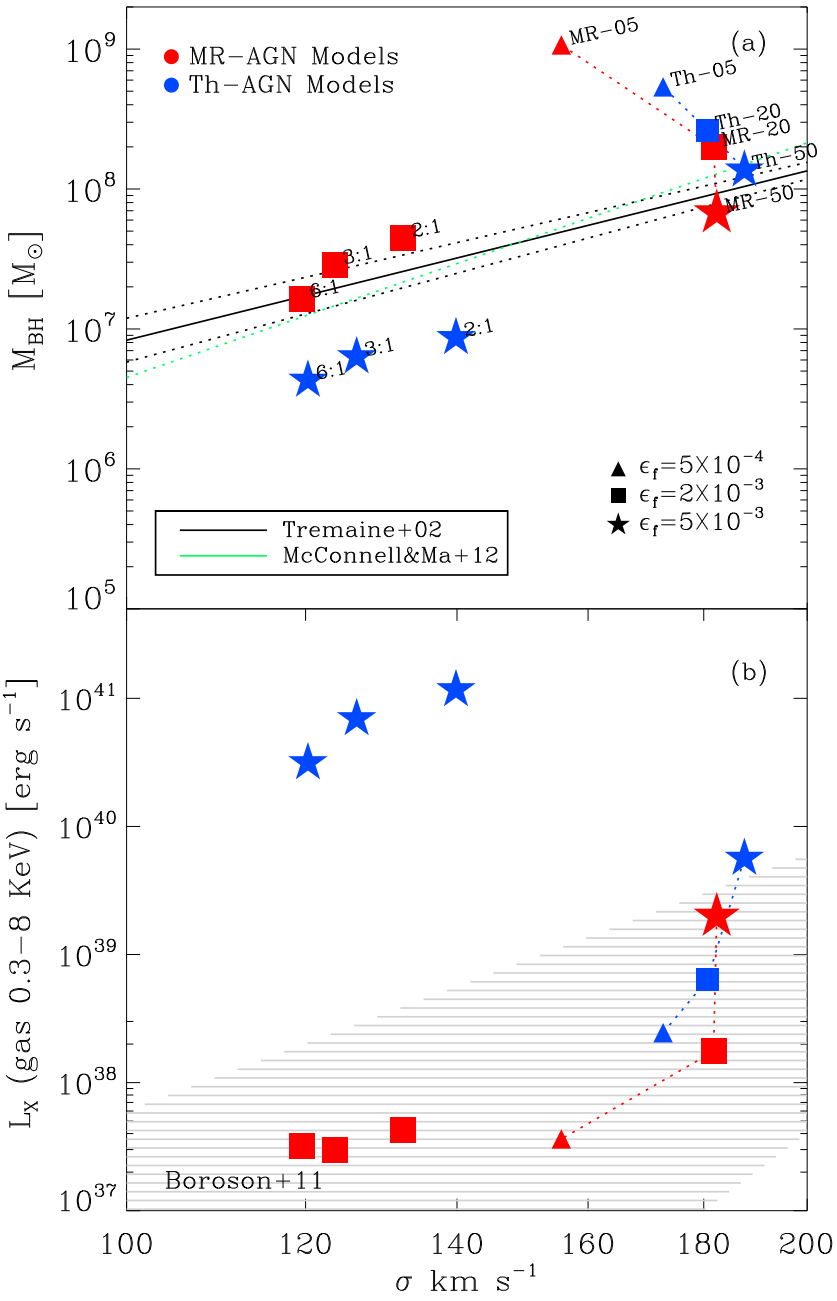



Figure 3.7: (a) $M_{\rm BH} - \sigma$ relation of the two feedback models. The blue symbols show Th-AGN models and red symbols show the MR-AGN models. Different symbols indicate the different feedback efficiencies. The merger progenitor mass ratios are indicated for the minor merger cases. The black and green lines show the observed relation with errors by Tremaine et al. (2002) and by McConnell & Ma (2013). (b) X-ray luminosity of the hot gas is plotted against stellar velocity dispersion $\sigma$. Observed relation (hatched region) is from Boroson et al. (2011).

dispersions in the merger remnants. We simulate equal-mass mergers with different feedback efficiencies and unequal-mass mergers with the adopted fiducial feedback efficiencies ($\epsilon_{\rm w} = 5 \times 10^{-3}$ for Th-AGN and $\epsilon_{\rm w} = 2 \times 10^{-3}$ for MR-AGN) for both feedback models and compare them with the observed $M_{\rm BH} - \sigma$ relation. We calculate the final black hole mass together with the mass-weighted line-of-sight stellar velocity dispersion $\sigma$ measured from all stellar particles within the projected half-mass radius $r_{\rm e}$. The feedback efficiency has a strong effect on the final black hole mass of the merger remnant in both feedback models, with the higher efficiency producing lower black hole masses. For the final stellar velocity dispersion on the other hand, the effect of feedback efficiency is less pronounced. The simulated Th-AGN-50 and MR-AGN-20 results are overplotted on the observed $M_{\rm BH} - \sigma$ by Tremaine et al. (2002) and McConnell & Ma (2013) as shown in Figure 3.7(a). In unequal-mass merger cases, MR-AGN-20 models evolve close to the observed $M_{\rm BH} - \sigma$ relation while Th-AGN-50 models result in lower black hole mass compared to the observed relation.

We show the X-ray luminosity of the hot gas against the stellar velocity dispersion $\sigma$ in Figure 3.7(b). Observationally all galaxies with a shallow potential well with $\sigma < 200$ km s$^{-1}$ seem to have only a small amount of hot gas with $L_X < 10^{40}$ erg s$^{-1}$ (Boroson et al., 2011). Observed $L_X$(gas) is correlated with $\sigma$, although not as strongly as the $M_{\rm BH} - \sigma$ relation. The effect of the black hole feedback prescription and feedback efficiency on the final stellar velocity dispersion is minor resulting in typically $160 < \sigma < 190$ km s$^{-1}$, however the effect on the X-ray luminosity is significant. Adopting higher feedback efficiency produces higher X-ray luminosity. Th-AGN-50 produces X-ray luminosities that are higher for the corresponding velocity dispersions. We show that reducing the feedback efficiency to $\epsilon_{\rm w} = 5 \times 10^{-4}$ produces X-ray luminosity within the observed range, but the resulting final black hole mass is factor of 20 larger than the one for its corresponding $\sigma$ in the thermal feedback cases. On the other hand, MR-AGN models result in lower X-ray luminosity compared to the Th-AGN models, and our proposed model MR-AGN-20 reproduces the observed $L_X - \sigma$ relation and $M_{\rm BH} - \sigma$ relation *simultaneously*. In case of minor mergers, all Th-AGN models show excessive X-ray luminosity compared to the observed range. The physical reason for the different results is easy to

understand. The MR-AGN models tends to expand the gaseous halo more than the Th-AGN, thus reducing the gas density and the thermal X-ray luminosity.

### 4.4 Galaxy Size

Observations have shown that quiescent massive galaxies at high redshift are much more compact than the local galaxies with the comparable mass and they have grown in physical size from $z \sim 1$ to $z \sim 0$. Some physical explanations have been suggested to explain this growth in size while avoiding the overproduction of present-day massive galaxies. Minor mergers involving lower mass galaxies has been proposed as one of the explanations, as they can produce efficient size growth (Naab et al., 2009). Hopkins et al. (2010) considered the various proposed channels for observed size evolution, and concluded that minor dry mergers are the "prime candidate" for explaining the majority of the observed sized growth, though other channels including adiabatic expansion due to mass loss from stellar winds should play a non-negligible role. However, the accretion of satellite stellar systems in minor mergers mainly contribute to the mass growth in the outer parts of elliptical galaxies (Oser et al., 2012; Hilz et al., 2013) and in this picture a factor of two decrease in central densities observed by Abraham et al. (2007); van Dokkum et al. (2008); Szomoru et al. (2010) cannot be fully explained (cf. Hilz et al., 2013). Other candidates include AGN feedback-driven star formation (Ishibashi et al., 2013) and secular processes such as adiabatic expansion driven by the expulsion of a substantial fraction of the gas out of the galaxy by stellar winds and/or strong AGN feedback (Fan et al., 2008, 2010). In the recent studies (Martizzi et al., 2012; Dubois et al., 2013), it is shown that the galaxies simulated with AGN feedback is more extended due to the AGN feedback induced gas expulsion compared to the no-AGN cases.

In this section, we test the possible contribution of the *puffing-up* process by the AGN mechanical feedback prescriptions, which have very different timescales for the AGN-driven winds. We also check whether the size increase by the AGN feedback induced mass loss which can account for the observed evolution is permitted by observational constraints on $M_{\rm BH} - \sigma$.

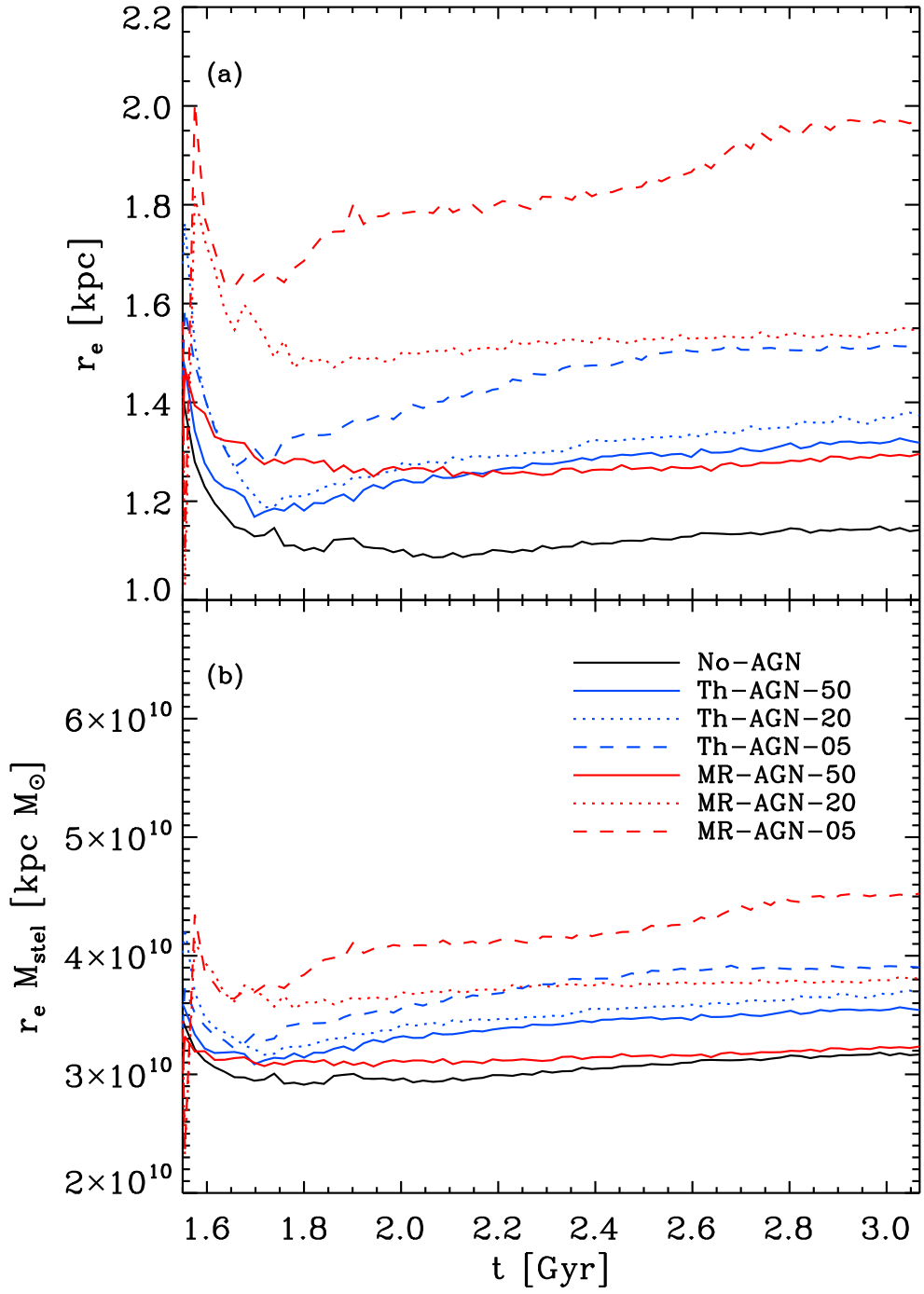



Figure 3.8: (a) Evolution of the effective radius, and (b) the adiabatic invariant for two feedback models.

The effect of the mass loss on the structure and dynamics of a stellar system depends on the amount of mass loss and on the timescale of ejection. The puffing up of a virialized stellar system by rapid mass loss is a well-known phenomenon, extensively studied both analytically and through numerical simulations, with reference to galaxies (Biermann & Shapiro, 1979), and to star clusters (Hills, 1980; Ragone-Figueroa & Granato, 2011). Adiabatic expansion can be also caused by much slower mass loss, for example, by stellar winds. If $\delta_r$ and $\delta_m$ are the fraction of changes in radius and in mass respectively as,

$$\delta_r \equiv \frac{r_1 - r_0}{r_0}, \quad \delta_m \equiv \frac{m_1 - m_0}{m_0} = \frac{\Delta m}{m_0}, \tag{3.12}$$

where $m_0$ and $m_1$ are the initial and final masses and $r_0$ and $r_1$ are the initial and final radii. When we have a rapid mass loss with a shorter ejection timescale than the dynamical timescale, we have

$$\delta_r = -\frac{\delta_m}{2\delta_m + 1}. \tag{3.13}$$

In this rapid mass loss case, when about a half of total mass is lost ($\delta_m \sim -0.5$), the radius expansion can be significantly large. For adiabatic changes, when the mass loss occurs on a timescale longer than the dynamical timescale, it is simply $rm = \text{const.}$ so we obtain

$$r_0 m_0 = r_1 m_1 \quad \Rightarrow \quad \delta_r = -\frac{\delta_m}{\delta_m + 1}. \tag{3.14}$$

In this case, the expansion proceeds at a rate proportional to the mass loss rate.

In the top panel of Figure 3.8, we show the temporal evolution of half-mass radii of the simulated galaxies of No-AGN and two AGN feedback models: Th-AGN and MR-AGN with three feedback efficiencies respectively. After the final galactic nuclei coalesce at $t \sim 1.5$ Gyr, MR-AGN-05 model has a large and continuous increase of the galaxy size, with the half-mass radius increasing by a factor of 1.25. MR-AGN models tend to have larger increment in size compared to the Th-AGN models. As discussed above, the momentum-based mechanical AGN feedback model can more rapidly and impulsively remove a large amount of cold gas from the

baryon-dominated central regions of the galaxies. It can trigger a puffing up of the central region of the stellar component while the dark matter halo extending far beyond the stellar distribution stabilizes the system and prevents its total disruption. However, the MR-AGN-05 model which shows the considerable size increase has much larger black hole mass growth with $M_{\rm BH} > 10^9 M_{\odot}$, which is inconsistent with the observed $M_{\rm BH} - \sigma$ relation. For MR-AGN-20 model consistent with the $M_{\rm BH} - \sigma$ relation, the size increase is negligible. Adiabatic expansion due to mass loss from AGN feedback plays a insignificant role for galaxy size growth as found in Hopkins et al. (2010).

In the bottom panel of Figure 3.8, we show the adiabatic invariant of the stellar component of the system. In most models, the adiabatic invariant shows minor increment, while MR-AGN-05 with the largest size increase shows the largest increase in the adiabatic invariant. The puffing-up process of the mechanical feedback models is non-adiabatic, and more efficient than the thermal feedback models following Equation 3.13.

We compare the effect of two AGN feedback models on the galaxy size as a function of total black hole mass growth in Figure 3.9. We show 3 models with MR-AGN feedback: MR-AGN-50, MR-AGN-20, and MR-AGN-05. In case of Th-AGN feedback models, we show the results with the identical feedback efficiencies, and additionally add one more model with the $\epsilon_{\rm w} = 1 \times 10^{-4}$ which shows the large enough mass growth in black hole comparable to MR-AGN-05. For the same mass growth in black hole, MR-AGN models have bigger effective radius than Th-AGN models as rapid mass loss effectively induces the puffing-up process. As before, the models with the lower AGN feedback efficiency show the considerable size increase but have much higher black hole mass growth, inconsistent with the observed $M_{\rm BH} - \sigma$ relation. Adiabatic expansion requires significant amount of mass loss by outflowing gas, thus requires a large black hole mass growth to be the explanation for the observed size evolution.

### 4.5 Central density

Figure 3.10 shows the evolution of the gas and the stellar masses contained within a fixed radius (1 kpc) in major merger simulations. The amount of gas in the central region of the galaxies

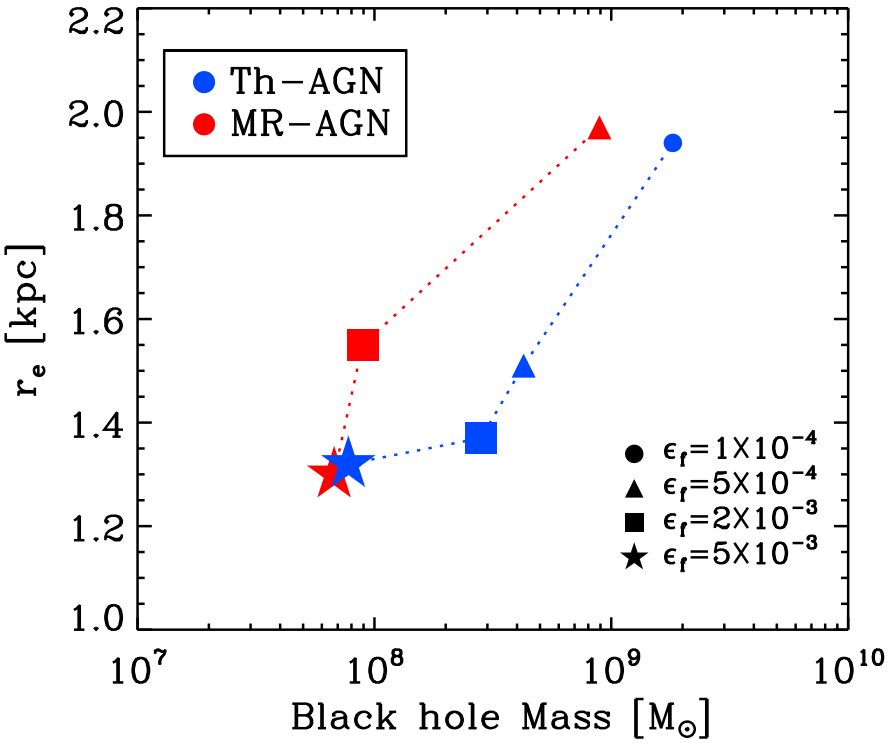



Figure 3.9: Galaxy size evolution of two feedback models, Th-AGN (blue) and MR-AGN (red), as a function of total black hole growth. Three models are shown for MR-AGN, with the feedback efficiency $\epsilon_{\rm w} = 5 \times 10^{-3}$, $2 \times 10^{-3}$ and $5 \times 10^{-4}$, with different symbols for the respective efficiencies. Th-AGN models with the same efficiency are shown along with the additional model of $\epsilon_{\rm w} = 1 \times 10^{-4}$ which has high enough mass growth in black hole comparable to MR-AGN-05.

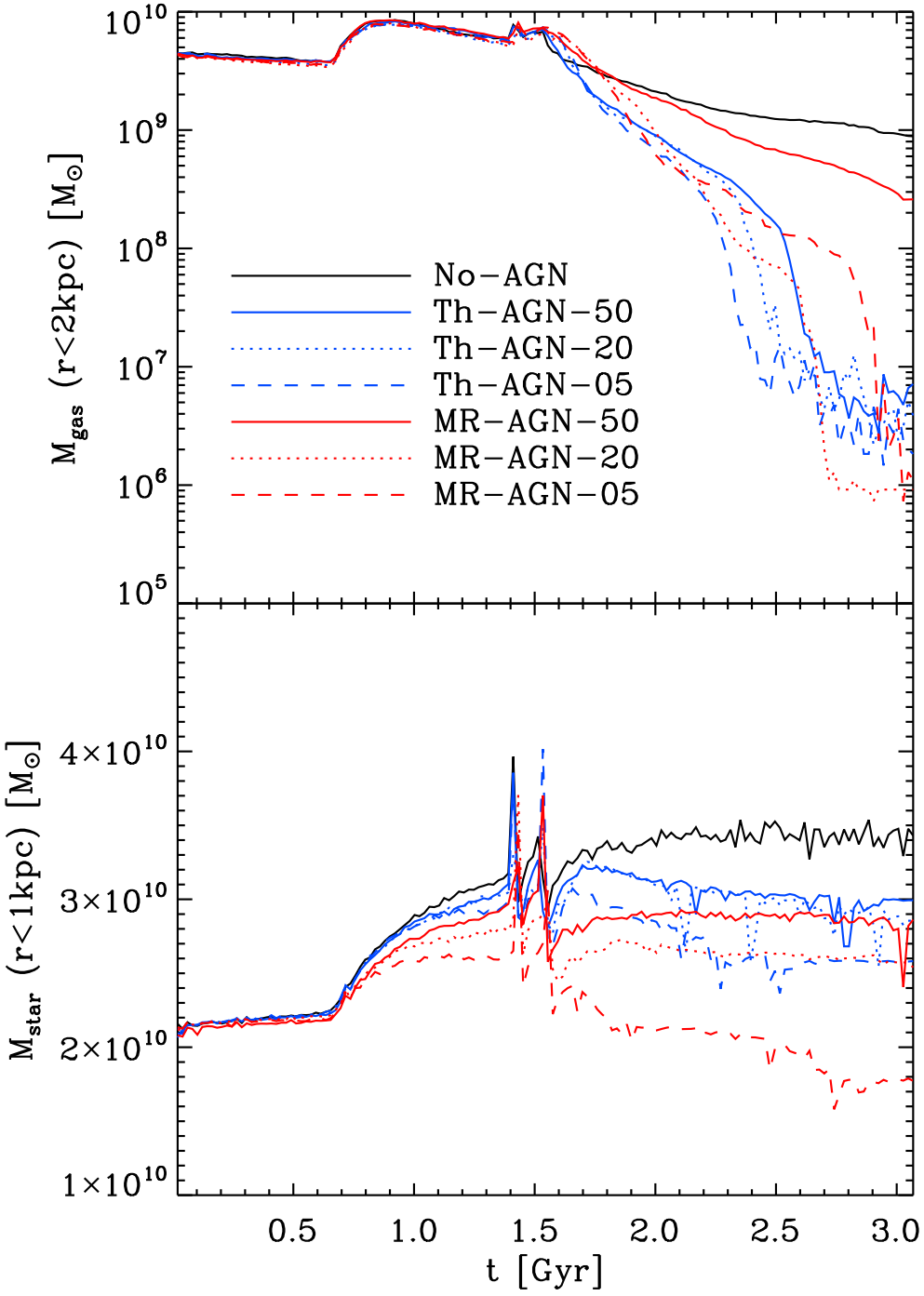



Figure 3.10: Evolution of gas mass enclosed within central 2 kpc radius (top) and stellar mass enclosed within central 1 kpc radius (bottom).

decreases due to the star formation, black hole mass accretion and the outflowing gas by the AGN feedback in both feedback models. The model MR-AGN-50, which has a smallest mass growth in black hole, shows the smallest decrease in gas within 2 kpc radius. In case of the stellar mass, both feedback models have lower central stellar density compared to No-AGN model mainly due to the less gas remaining in the central region of the galaxy, but the difference tends to be larger in MR-AGN models. Compared to the No-AGN model, Th-AGN-50 has 13% less stellar mass and MR-AGN-20 has 25% less stellar mass within 1 kpc radius. The central densities show little decrease after the merger despite the fact that the gas is thrown out by AGN feedback in most models. However, in case of MR-AGN-05 which shows the largest increase in galaxy size, the central density decreases by 30 % after the merger. As before, the quasar activity can lower the central stellar density of the galaxy, but only when it has enough black hole mass growth and a corresponding large amount of outflowing gas. However, the required black hole mass growth to explain the recent observations of the mild decrease of central stellar mass in elliptical galaxies (e.g. Milosavljević & Merritt, 2001; Szomoru et al., 2010; Saracco et al., 2012; van de Sande et al., 2013) is inconsistent with the observed $M_{\rm BH} - \sigma$ relation.

## 5 Discussions and Summary

We have investigated the effects of radiative and momentum-based mechanical AGN feedback on the gas flow in galaxy mergers, with the aid of three-dimensional SPH simulations. Our numerical black hole model incorporates both radiative and mechanical AGN feedback and renders a physically more accurate picture of how a galaxy and its embedded black hole evolve under each others influence, providing a powerful tool in understanding the coevolution of black holes and galaxies. Our main results and new advancements are as follows.

1. *Self-regulated black hole growth.* We show that our new proposed AGN feedback treatment is an effective mechanism for halting further growth of the black hole once it has reached a critical size for the gravitational potential of the bulge. We show the successful treatment of the mechanical and radiation feedback in recovering the observed $M_{\rm BH} - \sigma$ relationship

between the black hole mass and the galaxy velocity dispersion. This was also obtained in the previous thermal feedback treatments (e.g. Di Matteo et al., 2005; Springel et al., 2005b) and remains as a strong argument in helping to understand the observed physical relation between black hole and galactic properties.

2. *Large fluctuation level in black hole mass accretion.* In the mechanical feedback model, the fluctuation level in black hole mass accretion, and therefore also in radiant output, is significantly greater than the thermal feedback prescription. Episodic accretion is the norm with bolometric luminosity fluctuating between $\sim 10^{-1}$ and $10^{-6}$ of $L_{\rm Edd}$ during merger events.

3. *Strong galactic outflow.* We show that the new feedback model can drive large-scale galactic outflows, which unbind a significant fraction of the gas of the host galaxy. The AGN-driven winds found in this study provide a promising explanation for the moderate velocity outflows observed in some post-starburst galaxies and for the narrow-absorption line winds with $v \sim 500 - 1500$ km s$^{-1}$ seen in local quasars. This behaviour is consistent with the recent founding by Debuhr et al. (2012) who also use a momentum based feedback implementation. Outflowing kinetic energy is 20 times larger in the mechanical feedback models and will have a corresponding larger effect on the surrounding intergalactic medium (Fabian et al., 2000).

4. *X-ray luminosity from hot gas consistent with observations.* We show that the thermal feedback model with the feedback efficiency of the standard value $\epsilon_{\rm w} = 5 \times 10^{-3}$ appears to produce X-ray luminosities that are too high for their corresponding velocity dispersions. On the other hand, our fiducial model with mechanical and radiative feedback prescription spreads the halo gas over a larger volume and results in lower X-ray luminosity from the hot gaseous halo compared to the thermal feedback, and our proposed model with $\epsilon_{\rm w} = 2.0 \times 10^{-3}$ reproduces observed $L_X - \sigma$ relation and $M_{\rm BH} - \sigma$ relation simultaneously.

5. *The effects of AGN feedback driven mass loss on the size and central density of the host galaxy.* We show that AGN-driven mass loss can moderately increase the galaxy size and

decrease the central density. However, as noted in Section 4.4, the required black hole mass growth to fully account for the observed galaxy size evolution is much larger than that observed. Given observational constraints on $M_{\rm BH} - \sigma$ relation, the mass loss driven by AGN feedback is expected to play an insignificant role in galaxy size.

# Bibliography

Abraham, R. G., et al. 2007, ApJ, 669, 184

Aller, M. C. & Richstone, D. O. 2007, ApJ, 665, 120

Anderson, M. E. & Bregman, J. N. 2011, ApJ, 737, 22

Anderson, M. E., Bregman, J. N., & Dai, X. 2013, ApJ, 762, 106

Bédorf, J. & Portegies Zwart, S. 2013, MNRAS, 431, 767

Biermann, P. & Shapiro, S. L. 1979, ApJ, 230, L33

Bondi, H. 1952, MNRAS, 112, 195

Bondi, H. & Hoyle, F. 1944, MNRAS, 104, 273

Booth, C. M. & Schaye, J. 2009, MNRAS, 398, 53

Boroson, B., Kim, D.-W., & Fabbiano, G. 2011, ApJ, 729, 12

Broderick, A. E., Chang, P., & Pfrommer, C. 2012, ApJ, 752, 22

Cavaliere, A. & Fusco-Femiano, R. 1976, A&A, 49, 137

Cen, R., Kang, H., Ostriker, J. P., & Ryu, D. 1995, ApJ, 451, 436

Choi, E., Ostriker, J. P., Naab, T., & Johansson, P. H. 2012, ApJ, 754, 125

Cimatti, A., et al. 2008, A&A, 482, 21

Ciotti, L. & Ostriker, J. P. 2007, ApJ, 665, 1038

Ciotti, L., Ostriker, J. P., & Proga, D. 2009, ApJ, 699, 89

—. 2010, ApJ, 717, 708

Cox, T. J., Di Matteo, T., Hernquist, L., Hopkins, P. F., Robertson, B., & Springel, V. 2006, ApJ, 643, 692

Crain, R. A., McCarthy, I. G., Frenk, C. S., Theuns, T., & Schaye, J. 2010, MNRAS, 407, 1403

Crain, R. A., McCarthy, I. G., Schaye, J., Theuns, T., & Frenk, C. S. 2013, MNRAS, 432, 3005

Crenshaw, D. M., Kraemer, S. B., & George, I. M. 2003, ARA&A, 41, 117

Dalla Vecchia, C., Bower, R. G., Theuns, T., Balogh, M. L., Mazzotta, P., & Frenk, C. S. 2004, MNRAS, 355, 995

Damjanov, I., et al. 2009, ApJ, 695, 101

Debuhr, J., Quataert, E., & Ma, C.-P. 2012, MNRAS, 420, 2221

Debuhr, J., Quataert, E., Ma, C.-P., & Hopkins, P. 2010, MNRAS, 406, L55

Dehnen, W. 2001, MNRAS, 324, 273

Di Matteo, T., Springel, V., & Hernquist, L. 2005, Nat, 433, 604

Dressler, A. 1989, in IAU Symposium, Vol. 134, Active Galactic Nuclei, ed. D. E. Osterbrock & J. S. Miller, 217

Dubois, Y., Devriendt, J., Slyz, A., & Teyssier, R. 2012, MNRAS, 420, 2662

Dubois, Y., Gavazzi, R., Peirani, S., & Silk, J. 2013, MNRAS

Dunn, J. P., Bautista, M., Arav, N., Moe, M., Korista, K., Costantini, E., Benn, C., Ellison, S., & Edmonds, D. 2010, ApJ, 709, 611

Eke, V. R., Navarro, J. F., & Frenk, C. S. 1998, ApJ, 503, 569

Fabian, A. C., Sanders, J. S., Ettori, S., Taylor, G. B., Allen, S. W., Crawford, C. S., Iwasawa, K., Johnstone, R. M., & Ogle, P. M. 2000, MNRAS, 318, L65

Fan, L., Lapi, A., Bressan, A., Bernardi, M., De Zotti, G., & Danese, L. 2010, ApJ, 718, 1460

Fan, L., Lapi, A., De Zotti, G., & Danese, L. 2008, ApJ, 689, L101

Ferguson, H. C., et al. 2004, ApJ, 600, L107

Fischer, T. C., Crenshaw, D. M., Kraemer, S. B., Schmitt, H. R., Mushotsky, R. F., & Dunn, J. P. 2011, ApJ, 727, 71

Gaspari, M., Brighenti, F., & Temi, P. 2012, MNRAS, 424, 190

Gebhardt, K., et al. 2000, ApJ, 539, L13

Gültekin, K., et al. 2009, ApJ, 698, 198

Guo, F. & Mathews, W. G. 2010, ApJ, 712, 1311

Haardt, F. & Madau, P. 1996, ApJ, 461, 20

Hernquist, L. 1990, ApJ, 356, 359

Hills, J. G. 1980, ApJ, 235, 986

Hilz, M., Naab, T., & Ostriker, J. P. 2013, MNRAS, 429, 2924

Hilz, M., Naab, T., Ostriker, J. P., Thomas, J., Burkert, A., & Jesseit, R. 2012, MNRAS, 425, 3119

Hopkins, P. F., Bundy, K., Hernquist, L., Wuyts, S., & Cox, T. J. 2010, MNRAS, 401, 1099

Hopkins, P. F., Hernquist, L., Cox, T. J., Di Matteo, T., Martini, P., Robertson, B., & Springel, V. 2005, ApJ, 630, 705

Hoyle, F. & Lyttleton, R. A. 1939, Proceedings of the Cambridge Philosophical Society, 34, 405

Ishibashi, W., Fabian, A. C., & Canning, R. E. A. 2013, MNRAS, 431, 2350

Johansson, P. H., Burkert, A., & Naab, T. 2009a, ApJ, 707, L184

Johansson, P. H., Naab, T., & Burkert, A. 2009b, ApJ, 690, 802

Johansson, P. H., Naab, T., & Ostriker, J. P. 2012, ApJ, 754, 115

Jones, C. & Forman, W. 1984, ApJ, 276, 38

Katz, N., Weinberg, D. H., & Hernquist, L. 1996, ApJS, 105, 19

Kormendy, J. 1993, in The Nearest Active Galaxies, ed. J. Beckman, L. Colina, & H. Netzer, 197–218

Li, J.-T. & Wang, Q. D. 2013, MNRAS, 428, 2085

Longhetti, M., Saracco, P., Severgnini, P., Della Ceca, R., Mannucci, F., Bender, R., Drory, N., Feulner, G., & Hopp, U. 2007, MNRAS, 374, 614

Lynden-Bell, D. 1969, Nat, 223, 690

Magorrian, J., et al. 1998, AJ, 115, 2285

Makino, N., Sasaki, S., & Suto, Y. 1998, ApJ, 497, 555

Marconi, A. & Hunt, L. K. 2003, ApJ, 589, L21

Martizzi, D., Teyssier, R., Moore, B., & Wentz, T. 2012, MNRAS, 422, 3081

McConnell, N. J. & Ma, C.-P. 2013, ApJ, 764, 184

McKee, C. F. & Ostriker, J. P. 1977, ApJ, 218, 148

Milosavljević, M. & Merritt, D. 2001, ApJ, 563, 34

Mo, H. J., Mao, S., & White, S. D. M. 1998, MNRAS, 295, 319

Moe, M., Arav, N., Bautista, M. A., & Korista, K. T. 2009, ApJ, 706, 525

Monaghan, J. J. 1992, ARA&A, 30, 543

Moster, B. P., Macciò, A. V., Somerville, R. S., Naab, T., & Cox, T. J. 2011, MNRAS, 415, 3750

—. 2012, MNRAS, 423, 2045

Müller-Sánchez, F., Prieto, M. A., Hicks, E. K. S., Vives-Arias, H., Davies, R. I., Malkan, M., Tacconi, L. J., & Genzel, R. 2011, ApJ, 739, 69

Naab, T. & Burkert, A. 2003, ApJ, 597, 893

Naab, T., Johansson, P. H., & Ostriker, J. P. 2009, ApJ, 699, L178

Navarro, J. F., Frenk, C. S., & White, S. D. M. 1995, MNRAS, 275, 720

Newman, A. B., Ellis, R. S., Bundy, K., & Treu, T. 2012, ApJ, 746, 162

Newton, R. D. A. & Kay, S. T. 2013, ArXiv e-prints

Nipoti, C., Treu, T., Leauthaud, A., Bundy, K., Newman, A. B., & Auger, M. W. 2012, MNRAS, 422, 1714

Novak, G. S., Ostriker, J. P., & Ciotti, L. 2011, ApJ, 737, 26

Omma, H., Binney, J., Bryan, G., & Slyz, A. 2004, MNRAS, 348, 1105

Oogi, T. & Habe, A. 2013, MNRAS, 428, 641

Oser, L., Naab, T., Ostriker, J. P., & Johansson, P. H. 2012, ApJ, 744, 63

Ostriker, J. P., Choi, E., Ciotti, L., Novak, G. S., & Proga, D. 2010, ApJ, 722, 642

Pfrommer, C., Chang, P., & Broderick, A. E. 2012, ApJ, 752, 24

Pounds, K. A. & Vaughan, S. 2011, MNRAS, 413, 1251

Proga, D. & Kallman, T. R. 2004, ApJ, 616, 688

Puchwein, E. & Springel, V. 2013, MNRAS, 428, 2966

Ragone-Figueroa, C. & Granato, G. L. 2011, MNRAS, 414, 3690

Rees, M. J. 1984, ARA&A, 22, 471

Rupke, D. S. N. & Veilleux, S. 2013, ApJ, 768, 75

Saracco, P., Gargiulo, A., & Longhetti, M. 2012, MNRAS, 422, 3107

Sazonov, S. Y., Ostriker, J. P., Ciotti, L., & Sunyaev, R. A. 2005, MNRAS, 358, 168

Shakura, N. I. & Sunyaev, R. A. 1973, A&A, 24, 337

Sijacki, D., Pfrommer, C., Springel, V., & Enßlin, T. A. 2008, MNRAS, 387, 1403

Sijacki, D., Springel, V., Di Matteo, T., & Hernquist, L. 2007, MNRAS, 380, 877

Sijacki, D., Springel, V., & Haehnelt, M. G. 2009, MNRAS, 400, 100

Springel, V. 2005, MNRAS, 364, 1105

Springel, V., Di Matteo, T., & Hernquist, L. 2005a, ApJ, 620, L79

—. 2005b, MNRAS, 361, 776

Springel, V. & Hernquist, L. 2003, MNRAS, 339, 289

Sturm, E., et al. 2011, ApJ, 733, L16

Szomoru, D., Franx, M., van Dokkum, P. G., Trenti, M., Illingworth, G. D., Labbé, I., Bouwens, R. J., Oesch, P. A., & Carollo, C. M. 2010, ApJ, 714, L244

Teyssier, R., Moore, B., Martizzi, D., Dubois, Y., & Mayer, L. 2011, MNRAS, 414, 195

Toft, S., Rasmussen, J., Sommer-Larsen, J., & Pedersen, K. 2002, MNRAS, 335, 799

Toft, S., et al. 2007, ApJ, 671, 285

Tremaine, S., et al. 2002, ApJ, 574, 740

Trujillo, I., Conselice, C. J., Bundy, K., Cooper, M. C., Eisenhardt, P., & Ellis, R. S. 2007, MNRAS, 382, 109

Trujillo, I., et al. 2004, ApJ, 604, 521

van de Sande, J., Kriek, M., Franx, M., van Dokkum, P. G., Bezanson, R., Bouwens, R. J., Quadri, R. F., Rix, H.-W., & Skelton, R. E. 2013, ApJ, 771, 85

van Dokkum, P. G., Franx, M., Kriek, M., Holden, B., Illingworth, G. D., Magee, D., Bouwens, R., Marchesini, D., Quadri, R., Rudnick, G., Taylor, E. N., & Toft, S. 2008, ApJ, 677, L5

# Chapter 4

# The Impact of Mechanical AGN feedback on the Formation of Massive Early-type Galaxies


**ABSTRACT**

We employ cosmological hydrodynamical simulations to investigate the effects of AGN feedback on the formation of massive early-type galaxies with present-day stellar masses of $M_* > 8.9 \times 10^{10}\,\mathrm{M}_\odot$. Using smoothed particle hydrodynamics simulations with a pressure-entropy formulation that allows an improved treatment of contact discontinuities and fluid mixing, we run three sets of simulations of 20 halos with different AGN feedback models: (1) no feedback, (2) thermal feedback, and (3) mechanical and radiation feedback. We assume that seed black holes are present at early cosmic epochs at the center of emerging dark matter halos and trace their mass growth via gas accretion and mergers with other black holes. Both feedback models successfully recover the observed $M_{\rm BH} - \sigma_*$ relation and black hole-to-stellar mass ratio for simulated central early-type galaxies, and the baryonic conversion efficiencies are reduced by a factor of two compared to models without any AGN feedback at all halo masses. However, elliptical galaxies simulated with thermal AGN feedback show a factor of $\sim 10^2$-$10^3$ higher X-ray luminosities and higher in-situ star formation rates than observed. The mechanical feedback model reproduces the observed correlation between X-ray luminosities and velocity dispersion of galaxies and efficiently suppresses star formation. It also results in galaxy size in agreement with the observed size relation.

# 1 Introduction

There is solid observational evidence that most massive galaxies harbor massive black holes in their centers (Kormendy & Richstone, 1995), the masses of which are correlated with many properties of their host galaxies (Magorrian et al., 1998; Ferrarese & Merritt, 2000; Gebhardt et al., 2000; Tremaine et al., 2002; Marconi & Hunt, 2003; Aller & Richstone, 2007; Burkert & Tremaine, 2010, and also refer to Kormendy & Ho, 2013). It was proposed that the energy released by the accretion mechanism onto black holes is sufficient enough to unbind galactic interstellar medium and trigger strong outflows (Silk & Rees, 1998). This AGN feedback mechanism is confirmed by many observational evidences including the broad absorption lines in the spectra of quasars, the detection of X-ray cavities and radio jets (see Fabian, 2012, and references therein).

Without the inclusion of AGN feedback traditional numerical cosmological simulations of the formation of massive early-type galaxies suffer from the 'overcooling' problem: over a Hubble time too much cold gas is able to cool at the centers of the galaxy halos (Katz & White, 1993; Oser et al., 2010). This leads to overly massive and actively star-forming ellipticals at present, in contradiction with observations (e.g. Kauffmann et al., 2003; Franx et al., 2008) and basic predictions of ΛCDM structure formation (e.g., Guo et al., 2010; Moster et al., 2013). Many semi-analytical models of galaxy formation, extended by various models for AGN feedback, have demonstrated that this process is relevant to successfully reproduce the bright end of the galaxy luminosity function (Bower et al., 2006; Croton et al., 2006; De Lucia & Blaizot, 2007; Somerville et al., 2008; Guo et al., 2011; Hirschmann et al., 2012). Dynamically and spatially better resolved direct hydrodynamical cosmological simulations including AGN feedback confirm that this mechanism is able to self-regulate the stellar baryon content in massive halos resulting in more realistic galaxy masses and colors (e.g., Sijacki et al., 2007; Di Matteo et al., 2008; Sijacki et al., 2009; Booth & Schaye, 2011; Teyssier et al., 2011; Martizzi et al., 2012; Puchwein & Springel, 2013; Vogelsberger et al., 2013; Dubois et al., 2013), and that it can reproduce the relatively tight $M_{\rm BH} - M_{\rm b}$ and $M_{\rm BH} - \sigma_*$ relations.

Many previous AGN feedback models only include a subset of the known and observed feedback processes. Since the importance of AGN-driven mass and momentum outflows in limiting the infall onto the black hole has been emphasized (See Ostriker et al., 2010; Debuhr et al., 2010, 2011), Choi et al. (2012, 2013) proposed a radiative and mechanical AGN feedback together with the detailed treatment of radiative heating, radiation pressure, and the Eddington force from black holes and investigated the effects of the new AGN feedback model. It is shown that the new feedback model can regulate the black hole growth, and successfully reproduce the observed and $M_{\rm BH} - \sigma_*$ relation in a way similar to the successful thermal feedback approach (Springel et al., 2005). But the commonly adopted thermal feedback model where all the feedback energy is distributed as thermal heating produces a factor of $\sim$100 higher thermal X-ray luminosity than expected for given stellar mass of the galaxy while the new approach reproduces the observed $L_X - \sigma_*$. The new feedback model also shows large fluctuations in both radiant and wind outputs, in agreement with observations (see also Debuhr et al., 2012).

In a next step we now aim at characterizing the evolution of galaxies and black holes with mechanical AGN feedback in a full cosmological context. Even though numerical limitations impose inevitable approximations in the form of sub-resolution grid models, cosmological simulations can provide a more complete view on the co-evolution of galaxies and their central black holes. Starting from initial conditions consistent with the early universe as specified by the WMAP (Spergel et al., 2003) and Planck satellites (Planck Collaboration et al., 2013). In order to statistically confront observations, we need a cosmological sample of massive galaxies and black holes that covers a wide range of environments and redshifts.

In this paper, we investigate the effects of mechanical and radiation AGN feedback on the cosmological formation of individual galaxies with three sets of cosmological, hydrodynamical zoom simulations of 20 halos in the mass range $1.1 \times 10^{12}\,{\rm M}_\odot \lesssim M_{\rm vir} \lesssim 1.0 \times 10^{13}\,{\rm M}_\odot$. This extends the recent studies by Oser et al. (2010, 2012), which our initial conditions are based on, but did not contain AGN feedback. In the three simulation sets, we add the commonly adopted thermal AGN feedback and our radiative and mechanical AGN feedback separately to investigate

their impact on the conversion of gas into stars, star formation, black hole growth, and thermal X-ray luminosity of hot gas.

The paper is organized as follows. Section 2 provides an introduction into our simulation and adopted AGN feedback model. In section 3, we discuss the effect of AGN feedback on black hole growth, black hole and galaxy scaling relations, X-ray luminosity of hot gas, star formation rates, and galaxy size. A final summary and discussion of this work is given in section 4.

# 2 Simulations

## 2.1 Numerical code

The simulations presented in this paper were performed with a modified version of the parallel smoothed particle hydrodynamics (SPH) code GADGET-3 (Springel, 2005). To further improve over its predecessor, the modified GADGET-3 includes an artificial viscosity implementation (Cullen & Dehnen, 2010) that uses a shock indicator based on the time derivate of the velocity divergence so as to improve shock treatment. It also includes an energy diffusion implementation based on Read & Hayfield (2012) to correct for mixing instabilities. We use a pressure-entropy formulation that allows contact in discontinuities and improved fluid mixing as described in Ritchie & Thomas (2001); Hopkins (2013); Saitoh & Makino (2013).

For the star formation and feedback prescription we use the self-regulated supernova feedback model of Springel & Hernquist (2003). This models treats the interstellar medium (ISM) as a two-phase medium (McKee & Ostriker, 1977) where clouds of cold gas are embedded in the hot gas phase at pressure equilibrium. Stars are allowed to form out of the cold gas phase if the local density exceeds a threshold value ($n > n_{th} = 0.205\,\mathrm{cm}^{-3}$) which is calculated self-consistently in a way that the equation of state is continuous at the onset of star formation. Additionally, the simulations include a cooling prescription for a primordial composition of hydrogen and helium and a redshift-dependent UV background radiation field with a modified Haardt & Madau (1996) spectrum.

### 2.2 Simulation setup

We use the cosmological 'zoom-in' initial conditions which are described in detail in Oser et al. (2010). The halos are picked from a dark matter only simulation using a flat cosmology with parameters obtained from WMAP3 (Spergel et al., 2007):
$h = 0.72,\ \Omega_{\rm b} = 0.044,\ \Omega_{\rm dm} = 0.216,\ \Omega_{\Lambda} = 0.74,\ \sigma_8 = 0.77$ and an initial slope of the power spectrum of $\rm n_s = 0.95$. From redshift zero we trace back in time all particles close to the halos of interest at any given snapshot. Those particles are then replaced with high-resolution gas and dark matter particles. The original dark matter particles are merged to reduce the particle count and the simulation time depending on their distance to the re-simulated halo. The new high mass resolution initial conditions are evolved from redshift z=43 to the present day.

The simulated halo masses cover the range $1.1 \times 10^{12}\,\rm M_{\odot} \lesssim M_{vir} \lesssim 1.0 \times 10^{13}\,\rm M_{\odot}$. and the central galaxy masses are between $8.9 \times 10^{10}\,\rm M_{\odot} \lesssim M_{*} \lesssim 1.0 \times 10^{12}\,\rm M_{\odot}$ at $z = 0$. The masses for the gas and star particles are $m_{*,gas} = 4.2 \times 10^{6}\,h^{-1}\,\rm M_{\odot}$ (Note that we spawn one star particle per gas particle), whereas the dark matter particles have a mass of $m_{\rm dm} = 2.5 \times 10^{7}\,h^{-1}\,\rm M_{\odot}$. The comoving gravitational softening lengths used are $\epsilon_{\rm gas,star} = 400\,\rm pc\,h^{-1}$ for the gas and star particles and $\epsilon_{\rm halo} = 890\,\rm pc\,h^{-1}$ for the dark matter. At $z \approx 2$ the corresponding physical softening length for stars is $\epsilon_{\rm gas,star} = 133\,\rm pc\,h^{-1}$ scaled with the square root of the mass ratio (Dehnen, 2001). In the following we present the results for 20 galaxies with masses larger than $M_{*} \approx 8.9 \times 10^{10}\,\rm M_{\odot}$ for direct comparison with observations. These galaxies are well resolved with $\approx 2.0 \times 10^{5} - 1.7 \times 10^{6}$ particles within the virial radius ($R_{\rm vir} \equiv R_{200}$, the radius where the spherical overdensity drops below 200 times the critical density of the universe at a given redshift). Using the above simulation parameters for zoom simulations has been shown to result in galaxies with reasonable present-day properties (Naab et al., 2007; Johansson et al., 2009; Naab et al., 2009; Oser et al., 2010). However, Oser et al. (2010) shows that the fraction of available baryons converted into stars, $f_{*}$, for galaxies in this mass range is typically 2 times higher than estimates from models that are constructed by matching observed luminosity

functions to simulated halo mass functions (Guo et al., 2010; Moster et al., 2010; Behroozi et al., 2010; Moster et al., 2013, and references therein).

### 2.3 Black hole formation and growth

In our cosmological simulations of structure formation black holes are modeled as collisionless sink particles which form in newly emerging dark matter halos. We assume that black holes are seeded such that any halo above a certain threshold mass contains one black hole at its center. We identify haloes on the fly during a simulation by calling a friends-of-friends (FOF) algorithm at regular intervals. All halos with a mass larger than $10^{11}\,h^{-1}\,\mathrm{M}_{\odot}$ are provided one black hole with mass of $10^{6}\,h^{-1}\,\mathrm{M}_{\odot}$ if they do not contain any black hole already. The black hole seed mass and halo threshold mass are chosen to roughly follow the Magorrian et al. (1998) relation and the chosen seed mass is small enough that it only makes a negligible contribution to the mass of the final black hole. Growth of supermassive black holes has been previously modeled with full cosmological hydrodynamical simulations with the chosen black hole seed mass ranges from $10^{5}\,h^{-1}\,\mathrm{M}_{\odot}$ to $10^{6}\,h^{-1}\,\mathrm{M}_{\odot}$, and a threshold mass for halo from $10^{9}\,h^{-1}\,\mathrm{M}_{\odot}$ to $10^{11}\,h^{-1}\,\mathrm{M}_{\odot}$, and it is shown that these seeds evolve into a population of supermassive black holes with masses and accretion luminosities in line with observational estimates by $z \sim 6$ (Sijacki et al., 2009; Di Matteo et al., 2012; Khandai et al., 2012; DeGraf et al., 2012). It has also been shown that the AGN behavior is not particularly sensitive to the seed mass (Hopkins et al., 2006).

The mass of black holes is assumed to grow via two channels: mergers with other black holes and accretion of gas. Two black hole particles are allowed to merge if they fall within their local SPH smoothing lengths and if their relative velocities are smaller than the local sound speed. The rate of the gas infall onto the black hole is estimated with a Bondi-Hoyle-Lyttleton parameterization (Hoyle & Lyttleton, 1939; Bondi & Hoyle, 1944; Bondi, 1952) with an alternative averaging method introduced in Choi et al. (2012). For gas with the density $\rho$, a sound speed $c_{\mathrm{s}}$

and the velocity relative to the black hole $v$, the mass accretion rate onto the central region is:

$$\dot{M}_{\rm inf} = \left\langle \frac{4\pi\alpha G^2 M_{\rm BH}^2 \rho}{(c_{\rm s}^2 + v^2)^{3/2}} \right\rangle, \tag{4.1}$$

where angle brackets denote the averaging over the SPH kernel. This method for the calculation of the black hole mass does the calculation in both time and space on an individual particle basis and then averages the results over the neighboring 64 particles in order to reduce the dependency on the number of SPH particles.

To avoid the unphysical accretion of unbound gas from outside the Bondi radius we statistically limit the accretion of mass to the gas within the Bondi radius. Since the mass distribution of each gas particle is smoothed with the kernel size, we allow for the full accretion rate only if the total volume of a gas particle resides within the Bondi radius. Otherwise, we reduce the probability of being absorbed by the black hole (soft Bondi radius criterion, see Choi et al. (2012)). To account for the time that it takes a particle at radius $r_j$ to be accreted, we include the free-fall modification to the accretion probability with an extra factor of

$$p_{j,\rm ff} = \frac{\frac{1}{\tau_j}}{\frac{1}{N_{\rm sph}} \sum_{j=1}^{N_{\rm sph}} \frac{1}{\tau_j}}, \tag{4.2}$$

where $\tau_j = r_j/(c_{{\rm s},j}^2 + v_j^2)^{1/2}$ is the free fall time and $N_{\rm sph}$ denotes the typical number of smoothing neighboring gas particles of the black hole. For a full description of the soft Bondi radius criterion and the free-fall modification, see Figure 1 and section 2.4 of Choi et al. (2012).

### 2.4 Radiative and mechanical black hole feedback

Motivated by observations of broad absorption line winds, which convey energy, mass and momentum into the surrounding gas with velocity $\sim 10,000$ km s$^{-1}$ outflows corresponding to a typical broad line wind velocity (Crenshaw et al., 2003; Moe et al., 2009; Dunn et al., 2010), we included these observed AGN winds in our numerical treatment following Ostriker et al. (2010).

In our model, the AGN winds carry a mass given by:

$$\dot{M}_{\rm outf} = \dot{M}_{\rm inf} - \dot{M}_{\rm acc}, \tag{4.3}$$

where $\dot{M}_{\rm outf}$, $\dot{M}_{\rm inf}$ and $\dot{M}_{\rm acc}$ respectively denote the outflowing/inflowing mass rate and the mass rate actually accreted onto the black hole. For simplicity we assume that the wind is launched at a fixed speed $v_{\rm w} = 10,000$ km s$^{-1}$. Then a momentum flux carried by the wind is given as,

$$\dot{p} = \dot{M}_{\rm outf} v_{\rm w}, \tag{4.4}$$

and the kinetic energy rate of the outflow is given as,

$$\dot{E}_{\rm w} \equiv \epsilon_{\rm f} \dot{M}_{\rm acc} c^2, \tag{4.5a}$$

$$= \frac{1}{2} \dot{M}_{\rm outf} v_{\rm w}^2, \tag{4.5b}$$

where $\epsilon_{\rm f}$ denotes the feedback efficiency. We can define the dimensionless quantity $\psi$, the ratio of the mass outflow rate to the accreted rate as,

$$\psi \equiv 2\epsilon_{\rm f} c^2 / v_{\rm w}^2 = \dot{M}_{\rm outf} / \dot{M}_{\rm acc}, \tag{4.6}$$

and we can rewrite the equation for the black hole accretion rate as,

$$\dot{M}_{\rm acc} = \dot{M}_{\rm inf} \frac{1}{1+\psi}. \tag{4.7}$$

As discussed in Ostriker et al. (2010); Choi et al. (2012) in the presence of significant AGN winds, not all of the mass entering the central region $\dot{M}_{\rm inf}$ actually reaches the black hole. For example, with the feedback efficiency typically adopted in the literature, $\epsilon_{\rm f} = 0.005$, and with the fixed wind velocity $v_{\rm w} = 10,000$ km s$^{-1}$, equation (6) and (7) indicate that only 10 percent of the inflowing mass is actually accreted onto the black hole while 90 percent is ejected in a wind.

We calculate the dimensionless quantity $\psi$ for the given feedback efficiency $\epsilon_{\rm f}$ and wind velocity $v_{\rm w}$, and stochastically select the wind particles from all gas particle attracted into the central zone by the black hole keeping the fraction of wind particles to the total inflowing particles as $\psi/(1+\psi)$. To deposit the wind mass and momentum, we give kicks to the gas particles selected following the stochastic approach. We set the direction of the wind to be parallel or anti-parallel to the direction of angular momentum of each gas particle, if the central black holes are surrounded by a gas disk this procedure results in a wind perpendicular to the disk plane (Proga & Kallman, 2004). The emitted wind particles share their momentum with two other nearby gas particles to reproduce the shock heated momentum-driven flows. We deposit the residual energy into these three particles in thermal form so that the total energy is conserved. This prescription gives a ratio of kinetic to thermal energy in the outflowing in the outflowing four particles, similar to that in the standard Sedov-Taylor self-similar blast wave.

In addition to the mechanical feedback described above, X-ray radiation from the accreting black hole can be coupled to the surrounding gas according to an approximation described in Sazonov et al. (2005), as in Ciotti et al. (2010); Novak et al. (2011); Choi et al. (2012, 2013); The luminosity flux from the two black holes is calculated at the position of each gas particle, and the flux is converted to the net volume heating rate $\dot{E}$ by adopting the Sazonov et al. (2005) formulae that include Compton heating and photoionization heating. Note that Equation 4.7, not Equation 4.1, determines the AGN luminosity flux and thus the magnitude of the radiation feedback. We also include the electromagnetic momentum, the radiation pressure from the X-ray flux from the black hole by adding a momentum per unit time of $\dot{p} = \dot{E}/c$. The added force is directed radially away from the black holes.

Finally, instead of limiting the maximum accretion rate to the Eddington rate, we compute the Eddington force acting on the surrounding gas particles, directed radially away from the black hole as described in Choi et al. (2012) and allow this force to act on the gas flow through the hydrodynamic equations. Naturally it reduces the inflow and increases the outflow but accretion exceeding the Eddington rates can occasionally occur.

In order to study the effects of different AGN feedback models, we investigate the influence on galaxy separately by running the full set of simulations with three different model:

**(1) NoAGN:** No black hole and no AGN feedback. This model is comparable to the results of Oser et al. (2010, 2012), but note that we use an alternative formulation of SPH designed to treat contact discontinuities more accurately, and include an artificial viscosity and an energy diffusion implementation.

**(2) ThAGN:** with black hole and the classical thermal AGN feedback. Note that we use the standard mass accretion prescription and parameters adopted and studied in the previous works of Sijacki et al. (2007, 2009), i.e., $10^5\,h^{-1}\,\mathrm{M}_\odot$ for black hole seed mass, $5\times10^{10}\,h^{-1}\,\mathrm{M}_\odot$ for threshold halo mass of the black hole seeding, and $\epsilon_\mathrm{f}=0.005$ for AGN feedback efficiency which produce a broad agreement with observational constraints.

**(3) MrAGN:** with black hole and mechanical and radiation AGN feedback. This model includes the modified black hole mass accretion described in Section 2.3.

We only consider the central galaxies within the simulated halos and their black holes in this study. Detailed analysis for the satellite galaxies and their black holes within the virial radius of the parent halo will be addressed in a forthcoming paper.

# 3 Cosmological simulations of AGN feedback in individual galaxy halos

## 3.1 Black hole growth

In order to show how individual black holes grow in our simulations, we show in Figure 4.1 an example of the mass assembly history of black holes in a representative halo with a mass of $\sim 5\times10^{12}\,h^{-1}\,\mathrm{M}_\odot$ with MrAGN model. Each line represents a black hole and the thickness of the lines is scaled by the mass of the black hole. Mass accretion on to the black hole is color-coded in Eddington units, as black hole mass accretion with Eddington ratio $m_\mathrm{Edd}<10^{-5}$ shown in red, $10^{-5}<m_\mathrm{Edd}<10^{-3}$ in yellow, $10^{-3}<m_\mathrm{Edd}<10^{-1}$ in green, and $10^{-1}<m_\mathrm{Edd}$ in blue. In total

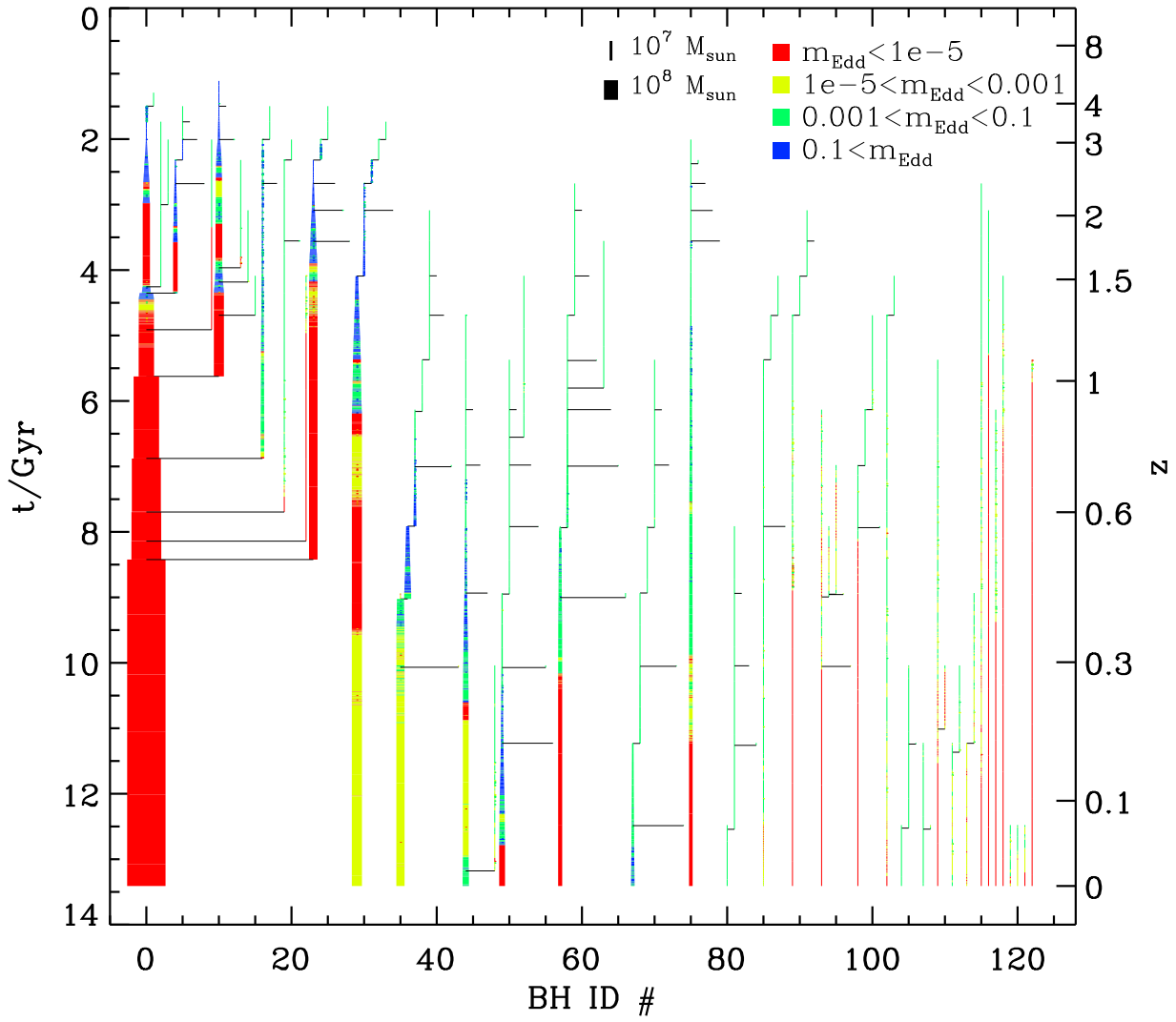



Figure 4.1: A mass assembly tree of black holes in a halo of mass $\sim 5 \times 10^{12}\, h^{-1}\, \mathrm{M}_{\odot}$ for a hydrodynamical zoom-in simulation with radiative and mechanical AGN feedback. Each line represents a black hole and the thickness of the lines is scaled by the mass of the black hole. Mass accretion on to the black hole is color-coded in Eddington units, as black hole mass accretion with Eddington ratio $m_{\mathrm{Edd}} < 10^{-5}$ shown in red, $10^{-5} < m_{\mathrm{Edd}} < 10^{-3}$ in yellow, $10^{-3} < m_{\mathrm{Edd}} < 10^{-1}$ in green, and $10^{-1} < m_{\mathrm{Edd}}$ in blue. In total 123 black holes are seeded, after black hole mergers only 27 black holes survive to $z = 0$. The leftmost branch of the merger tree shows the central black hole with a final mass of $\sim 3 \times 10^{8}\, h^{-1}\, \mathrm{M}_{\odot}$. The left-right positioning of the progenitors is schematic, and has no relevance to spatial positions of galaxies within the dark matter halo.

123 black holes are seeded, after black hole mergers only 27 black holes survive to $z = 0$. The left–right positioning of the progenitors is schematic, and has no relevance to spatial positions of galaxies within the dark matter halo. The leftmost branch of the merger tree shows the central black hole with a final mass of $\sim 3 \times 10^8\, h^{-1}\, \mathrm{M}_\odot$. At $z = 0$, the most massive black hole is growing less rapidly than less massive black holes. At higher redshift, this trend is greatly diminished, and at z = 2 it is reversed so that the most massive black holes have the highest fractional accretion rate. This phenomenon broadly agrees with the observed 'cosmic downsizing' of AGN, i.e., the most massive and luminous AGN were most numerous at redshift $z \sim 2 - 2.5$, less luminous AGN peaked at successively lower redshifts with the least luminous peaking at around $z \sim 1$ in X-rays (e.g., Ueda et al., 2003), and in optical and other bands (e.g., Rigby et al., 2011). Detailed analysis of the characteristic time of black hole growth with the simulated central and satellite black holes of different masses will be addressed in the future works.

We now study how the black hole masses relate to their host galaxies. For this purpose, we determine the central galaxy properties using a spherical over-density criterion at $z = 0$. Following previous studies (e.g., Oser et al., 2012), we obtain a radius where the spherical over-density drops below 200 times the critical density of the universe for a virial radius of the halo, $r_{\rm vir}$, and the virial mass $M_{\rm vir}$ is defined by the dark matter mass therein. We then determine the effective radius of the galaxy $r_{\rm eff}$ by getting the mean values of the half-mass radii of all stars within 10% of the virial radius $r_{10} = 0.1 \times r_{\rm vir}$ projected along the three principal axes of the main stellar body. The line-of-sight velocity dispersions $\sigma_*$ have been calculated within $0.5 \times r_{\rm eff}$ along the three principal axes and then averaged.

In Figure 4.2, we show the relation between black hole mass and stellar velocity dispersion $\sigma_*$ for the two feedback models. Blue circle symbols are for the simulations with the classical thermal AGN feedback, ThAGN, while red circle symbols are for the simulations with the mechanical and radiation AGN feedback, MrAGN. Note that two feedback models are simulated for the same set of 20 halos. We overplot the observed $M_{\rm BH} - \sigma_*$ relations as determined by recent works by McConnell & Ma (2013) (black) and Kormendy & Ho (2013) (blue) respectively. We find a good agreement with the observations for both AGN feedback models as found in our previous study

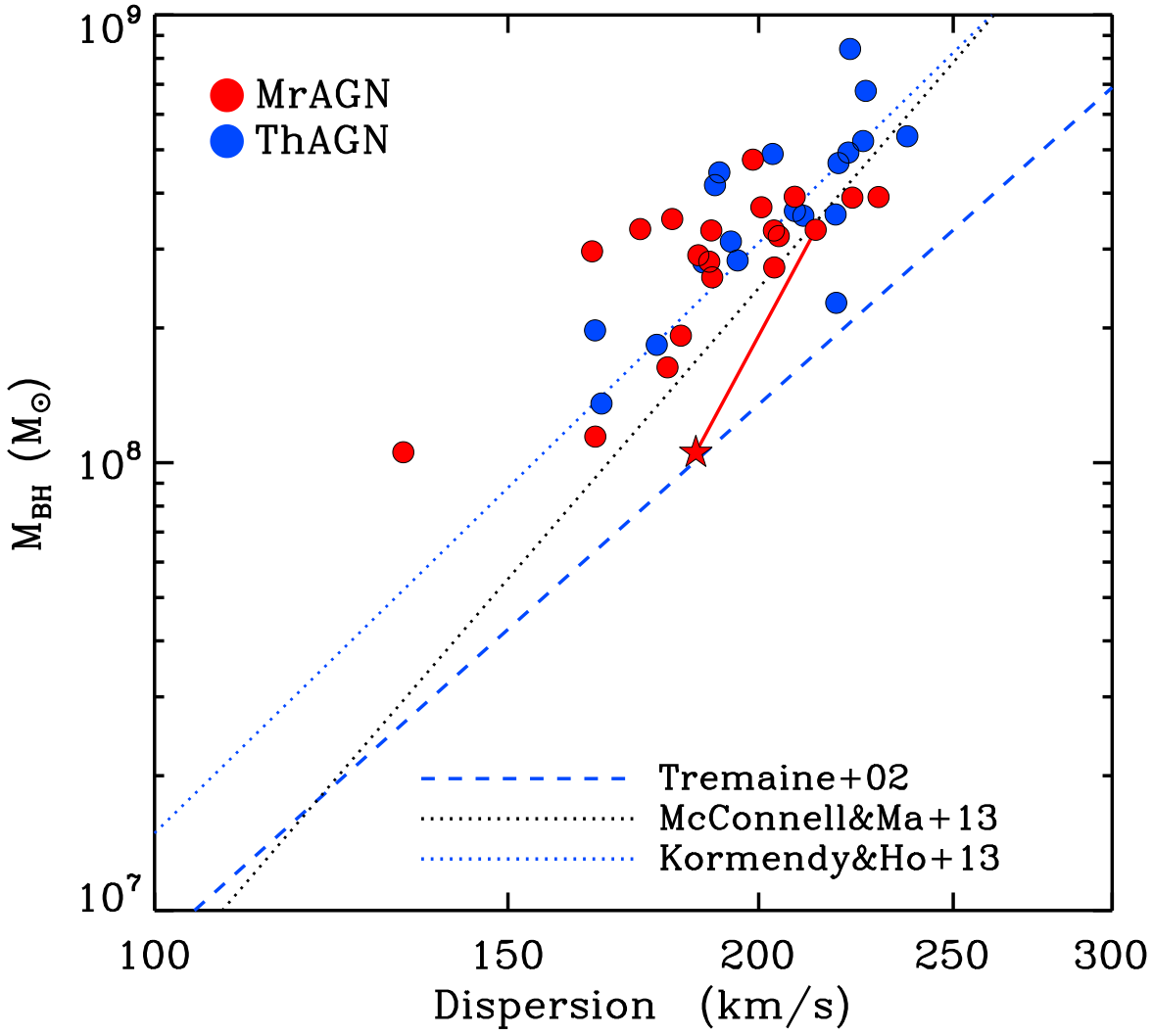



Figure 4.2: $M_{\rm BH} - \sigma_*$ relation of the two feedback models: ThAGN (blue) and MrAGN (red). The black/blue dotted lines show the observed relation of the early type galaxies from McConnell & Ma (2013) and Kormendy & Ho (2013) respectively.

on the bulge dominated merger remnants of the two disk galaxies (Choi et al., 2013). In previous works on the black hole growth with the classical thermal AGN feedback (e.g., Sijacki et al., 2007; Di Matteo et al., 2008), a measurement of the $M_{\rm BH} - \sigma_*$ relation for the simulated galaxies was also found to successfully produce the observed black hole - bulge relations. Note that we use the parameters adopted in Sijacki et al. (2007), but we use the modified version of GADGET-3 code with an alternative formulation of SPH, an artificial viscosity and an energy diffusion implementation. Modification of the code we include in this study does not change their main findings on the black hole mass and bulge relation in general.

Figure 4.3 shows the black hole–to–stellar mass ratio as a function of galaxy stellar mass for the simulated two feedback models: blue circle symbols are for ThAGN models and red circle symbols are for MrAGN models. The observed relations with an intrinsic dispersion from Marconi & Hunt (2003) and Kormendy & Ho (2013) are shown in blue lines and black lines respectively. The simulated relations at $z = 0$ for both AGN feedback models match the locally observed canonical black hole–to–bulge mass ratio 0.23% from Marconi & Hunt (2003) well, but the simulated ratios are $\sim 2$ times lower than the most recent relation found by Kormendy & Ho (2013) who strictly limit their samples and omit all pseudo bulges and merging galaxies. Since we have not made such a restriction for measuring stellar mass in sour simulated galaxies, our result would be more comparable to the previously found values of the canonical black hole–to–bulge mass ratios.

### 3.2 Impact of AGN feedback on X-ray luminosity

The thermal AGN feedback prescription adopted in many previous AGN feedback studies hides the small-scale physics such as radiation-driven winds and shocks under a simple parameterization, and only treats the resulting effects of feedback. As a result, the gas is simply heated near the black hole and produces a very large thermal X-ray luminosity. In the mechanical AGN feedback model, however, the X-ray luminosity is lower, because the outflowing gas carries off significant kinetic energy, which tends to drive gas away from the galaxy, reduce its density and significantly reduce its thermal X-ray output. Hence comparing our simulations with the

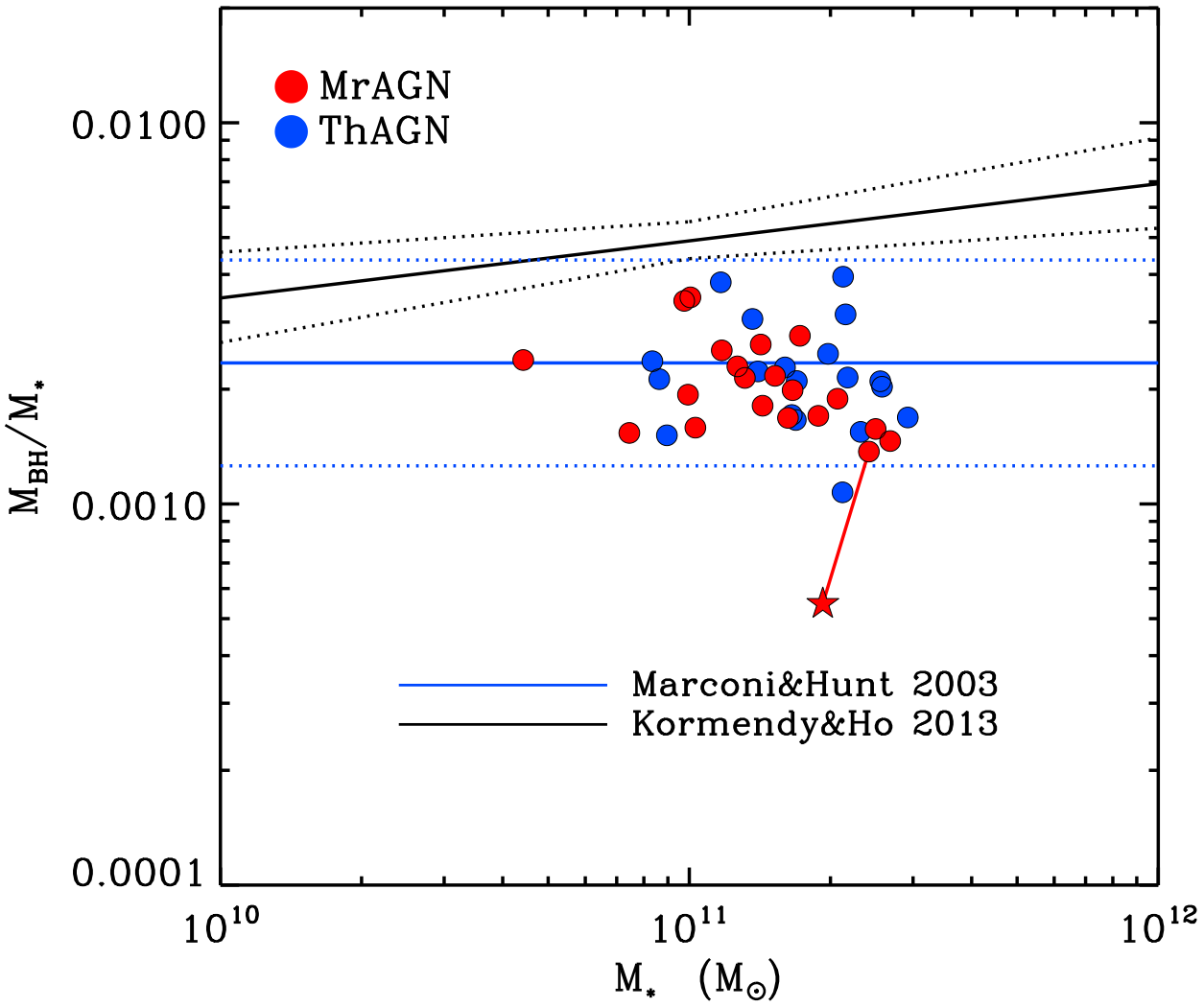



Figure 4.3: $M_{\rm BH}$-to-stellar mass ratio is plotted against stellar mass for two feedback models: ThAGN (blue) and MrAGN (red). The blue solid line shows the observed relation from Marconi & Hunt (2003) with an intrinsic dispersion shown in blue dotted lines and black lines are from Kormendy & Ho (2013).

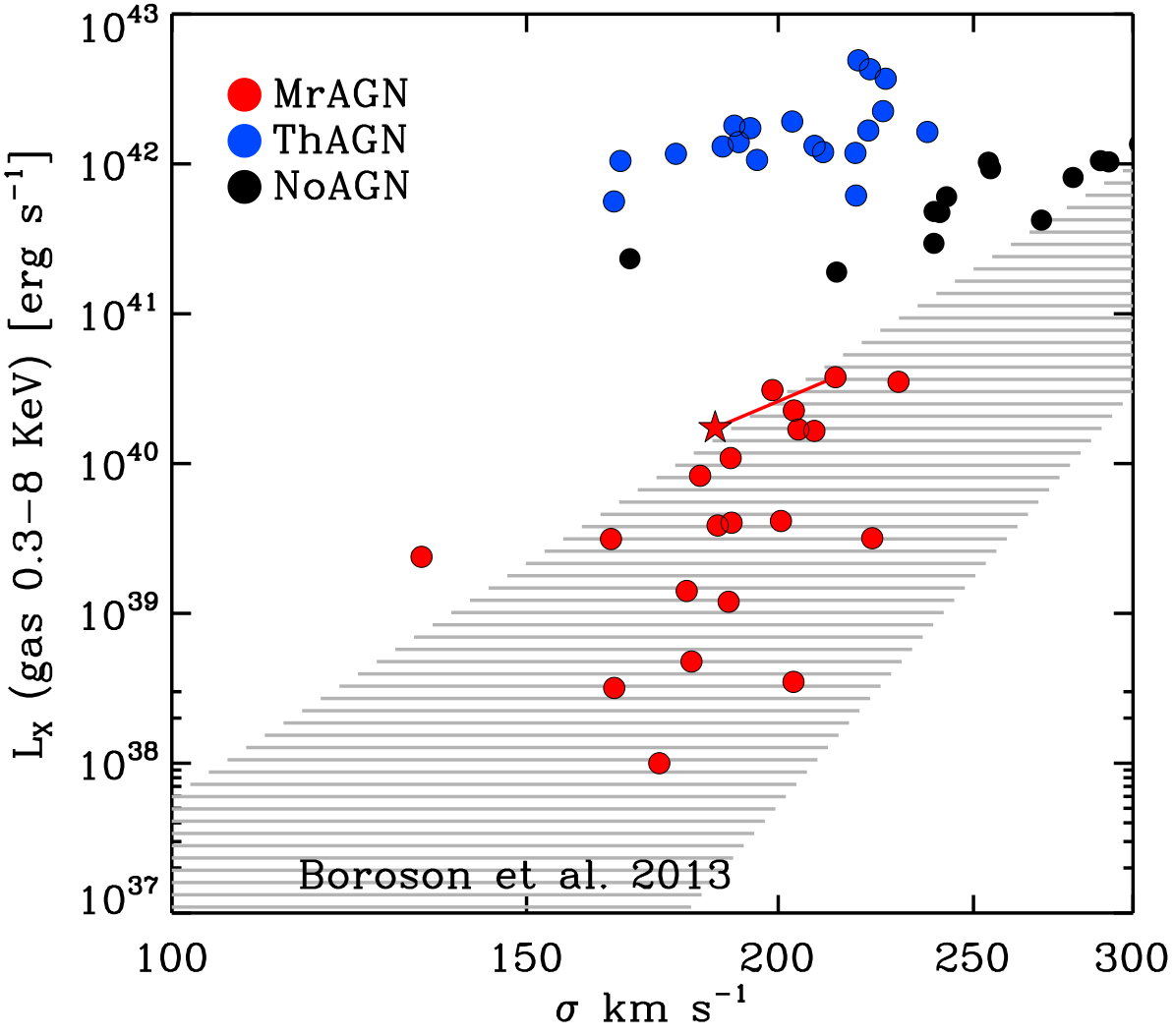



Figure 4.4: X-ray luminosity of the hot gas is plotted against stellar velocity dispersion $\sigma$ for the simulated galaxies with the two AGN feedback models: ThAGN (blue) and MrAGN(red). Observed relation for the normal early-type galaxies from Boroson et al. (2011) is shown with the hatched region.

observations of X-ray emission from nearby ellipticals should give us a clean discriminant between the AGN feedback models. We calculate the X-ray luminosity due to bremsstrahlung radiation as well as line emission from all relevant species in *Chandra* bands (0.3-8 keV) for the simulated central elliptical galaxies using the tools developed in Choi et al. (2013). In order to exclude the star forming gas in the obscured central region of the galaxy, we only include the hot and diffuse gas within the virial radius with a temperature and density cut of $T \geq 10^6$ K, and $\rho \leq 3.16 \times 10^{-3}\,\mathrm{M_\odot pc^{-3}}$, which corresponds to the critical density for star formation.

In Figure 4.4, we show the X-ray luminosity of the hot gas against the stellar velocity dispersion $\sigma$ for the simulated central galaxies with three feedback models. The observed relation for normal early-type galaxies from Boroson et al. (2011) is shown with the hatched region. Observationally all galaxies with a shallow potential well with $\sigma < 200$ km s$^{-1}$ seem to have only a small amount of hot gas with $L_X < 10^{40}$ erg s$^{-1}$ (Boroson et al., 2011), however, ThAGN models show much higher X-ray luminosity for up to $\sim$ 2-3 orders of magnitude higher. On the other hand, MrAGN models produce X-ray luminosity within the observed range, with the two orders of magnitude spread in $L_X$.

### 3.3 Baryonic mass budget

Fig. 4.5 shows the conversion efficiency of the simulated galaxies at redshift zero $f_* = m_*/(f_b * m_{vir,dark})$ where $m_*$ is the stellar mass within 10 % of the virial radius $r_{10}$, $f_b = \Omega_b/\Omega_{dm} = 0.20$ is the cosmic baryon fraction and $m_{vir,dark}$ is the dark matter mass within the virial radius of the galaxy. Therefore $f_b * m_{vir,dark}$ is the amount of total baryonic matter available in each halo and $f_*$ the fraction thereof that is converted into stars in the central galaxy. For simulated galaxies with NoAGN model, the fraction declines in a roughly linear fashion with the logarithm of the halo mass from $f_* \approx 0.6$ for the smallest halos ($\approx 10^{12} M_\odot$) to $f_* \approx 0.2$ for high mass halos ($\gtrsim 10^{13} M_\odot$), over-predicting by a factor of $\sim 2-3$ as shown in Oser et al. (2012). Note that the conversion efficiency of NoAGN models we obtain in this study is slightly higher than the value from Oser et al. (2012). We use the modified version of GADGET-3 code with an

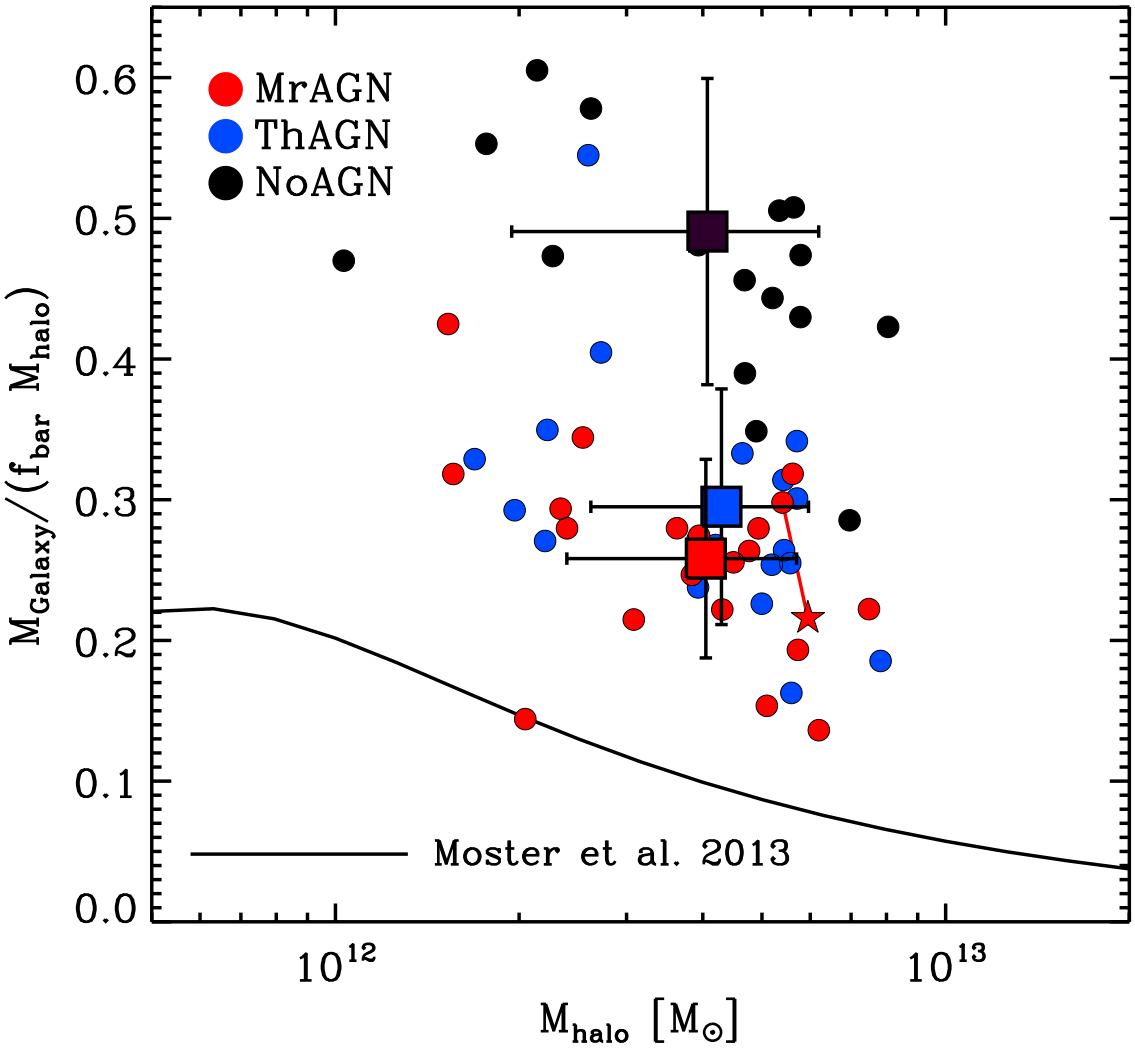



Figure 4.5: Fraction of baryons that is converted into stars at $z = 0$ for NoAGN model (black), thermal feedback models (blue), and momentum feedback models (red). The solid black line shows the results of Moster et al. (2013).

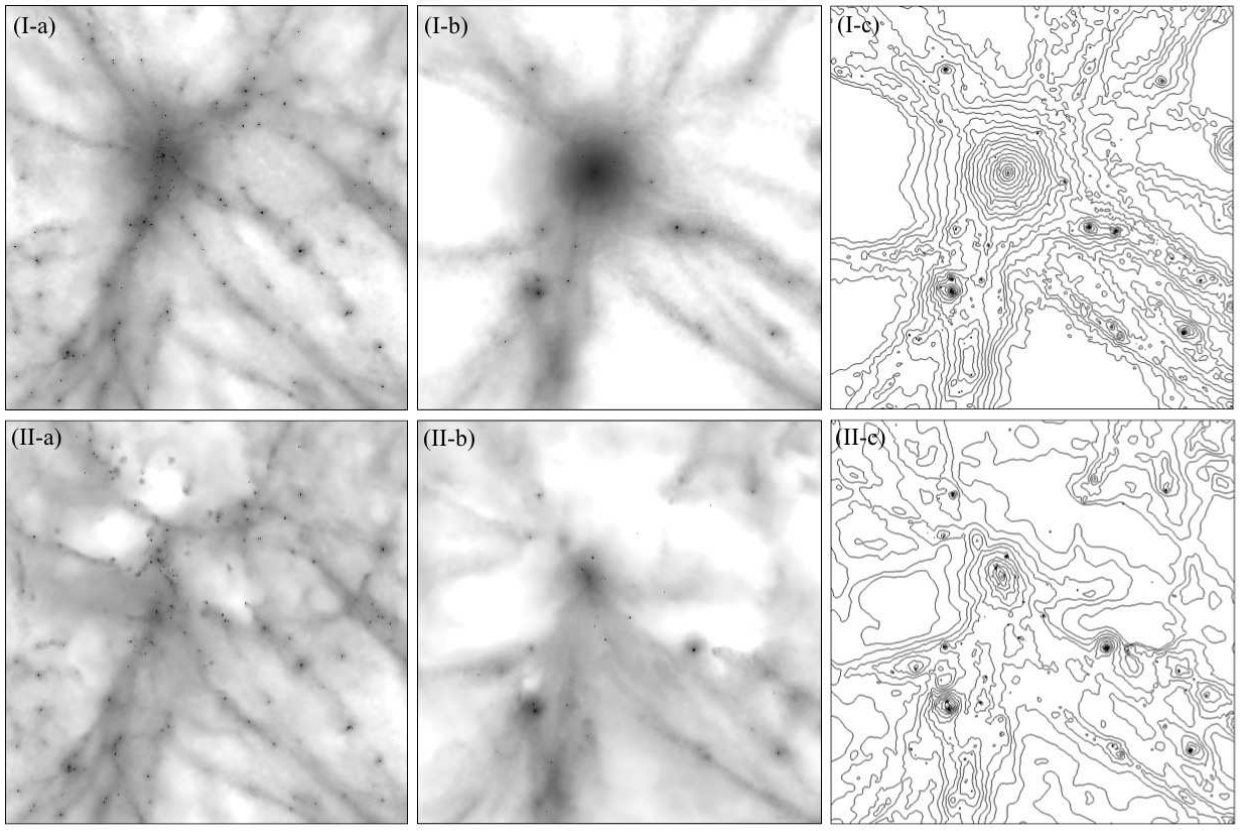



Figure 4.6: Projected gas density maps of the central galaxy in a zoom-in simulation of a $5 \times 10^{12}\, h^{-1}\, \mathrm{M}_{\odot}$ dark matter halo – with traditional ThAGN feedback in the top panels, and with MrAGN feedback in the bottom panels. The projected gas density maps at $z = 1.4$ are shown in the left-most panels (I-a, II-a), and maps at $z = 0$ are shown in the middle panels (I-b, II-b). Coutours of projected gas density at $z = 0$ are shown in right-most panels (I-c, II-c). The images are 4 Mpc on a side and brighter color indicates a lower density. While the ThAGN model does not generate any high velocity outflows and bubbles as shown in upper panels, in the MrAGN model the high velocity winds with $v_{\mathrm{w}} \sim 10,000$ km s$^{-1}$ effectively shock the ambient gas and generate cavities around the central massive galaxies in panel (II-a). Bubbles further expand and effectively lower the gas density around the central elliptical galaxy in panels (II-b) and (II-c).

alternative formulation of SPH, an artificial viscosity and an energy diffusion implementation, therefore in our simulations more gas cools resulting higher conversion efficiency. In case of AGN feedback models, both ThAGN and MrAGN models show lower conversion efficiency compared to NoAGN models, but they still over-predict by a factor of $\sim 1.5 - 2$ than the estimation from recent estimates of the conversion efficiency based on the matching technique. This seems to be due to the absence of the ejective supernova wind feedback, which is especially important for low-mass systems. Our simulations do not generate significant winds in the low-mass systems which do not have massive black holes, and thus overestimate the condensed baryon fraction of low-mass galaxies that can accrete onto high mass galaxies at late stages of evolution. This may produce a factor of 1.5 discrepancy for high-mass galaxies because of over-predicted accreted stars from the low-mass galaxies The discrepancy can be effectively reduced by including wind stellar feedback as shown in Hirschmann et al. (2013).

### 3.4 Star formation

One of the most important findings in the MrAGN feedback models is the effective AGN-driven quenching of star formation in central galaxies. As shown in Figure 4.6, the high velocity outflowing winds shock the ambient gas and generate cavities around the central massive galaxies, significantly suppressing star formation. In Figure 4.7 we show the star formation rate over time for the central galaxy in a representative halo with a mass of $\sim 5 \times 10^{12}\, h^{-1}\, \mathrm{M}_{\odot}$ with the various feedback models, considering stars within the virial radius $\sim 150$ kpc (solid lines) and within the effective radius $\sim 4$ kpc (dashed lines) of the galaxy center at z = 0. In MrAGN model (red), the AGN feedback drives a large-scale wind that removes nearly all of the residual gas from the galaxy, effectively and rapidly quenching star formation. It produces massive red and dead galaxies and reduces the final stellar mass by a factor of two compared to the previous studies without AGN feedback (e.g., Oser et al., 2010). The MrAGN model will be further tested by comparing the star formation activities of the larger sample of simulated galaxies to observations in a forthcoming paper.

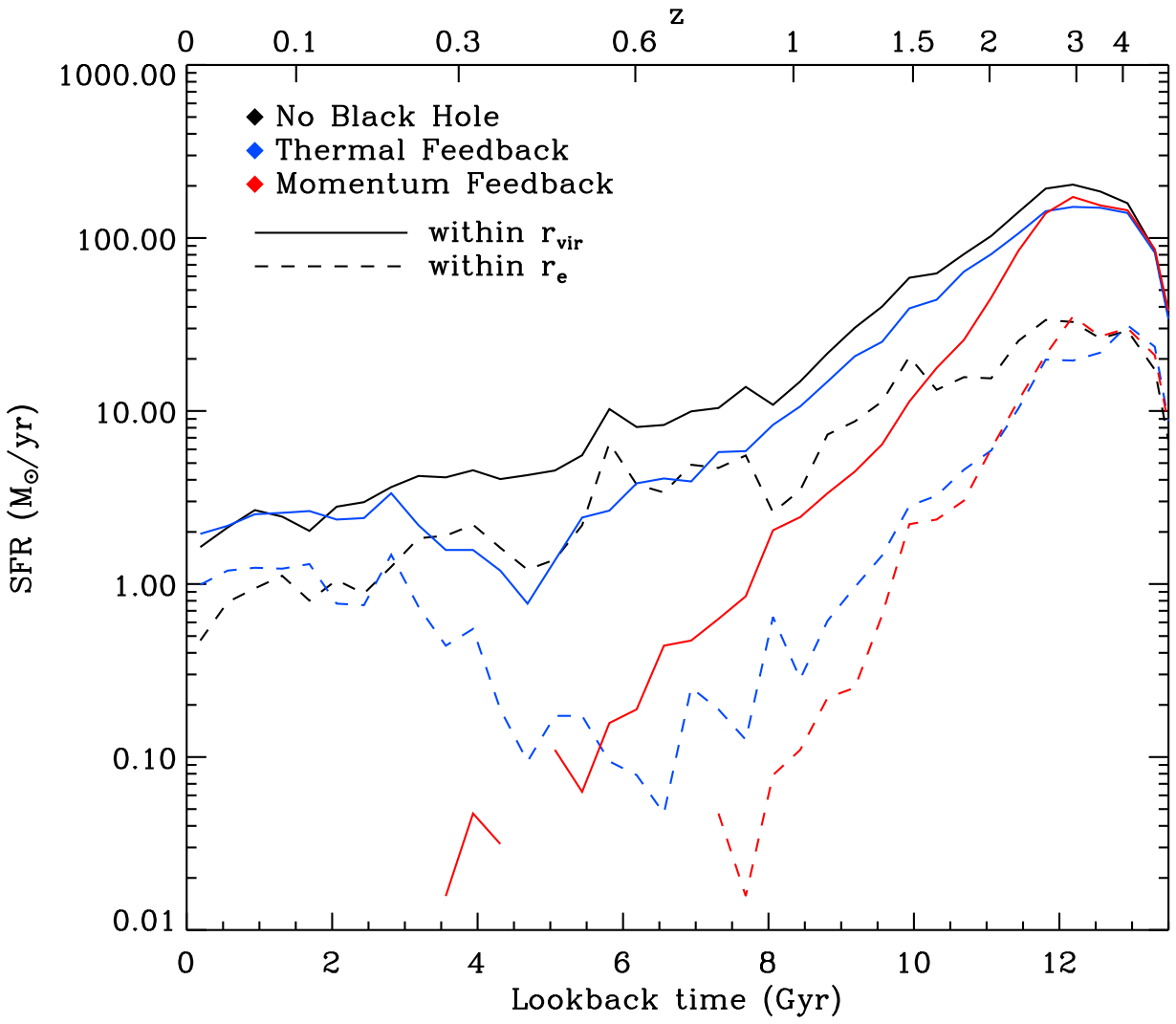



Figure 4.7: The star formation rate over time for the central galaxy in a representative halo with a mass of $\sim 5 \times 10^{12}\, h^{-1}\, \mathrm{M}_\odot$ with the various feedback models, considering stars within the virial radius $\sim 150$ kpc (solid lines) and the effective radius $\sim 4$ kpc (dashed lines) of the galaxy center at z = 0. In the MrAGN feedback model (red), the AGN feedback drives a large-scale wind effectively and rapidly quenches star formation and makes the galaxy red and dead.

### 3.5 Galaxy size

In Figure 4.8, we show the projected half-mass radii of simulated galaxies with MrAGN as a function of their stellar mass at $z = 0$. We determine the effective radius of the galaxy $r_{\rm eff}$ by determining the mean values of the half-mass radii of all stars within 10% of the virial radius $r_{10} = 0.1 \times r_{\rm vir}$ projected along the three principal axes of the main stellar body. The dashed black line shows the observed relation from Nipoti et al. (2009), which is a linear fit to the SLACS sample of local early-type galaxies at $z = 0$ with the observed scatter given by the dotted lines. Compared to the observation, MrAGN model predicts reasonable sizes in agreement with Oser et al. (2012).

## 4 Summary

In this paper, we have run three sets of cosmological hydrodynamic simulations of 20 halos with masses between $8.2 \times 10^{11}\,h^{-1}\,{\rm M}_\odot \lesssim M_{\rm vir} \lesssim 7.3 \times 10^{12}\,h^{-1}\,{\rm M}_\odot$ using a modified GADGET-3 SPH code with different AGN feedback models: (1) No black hole and AGN feedback (NoAGN), (2) the standard thermal AGN feedback (ThAGN) (e.g., Di Matteo et al., 2005; Springel et al., 2005; Sijacki et al., 2007; Di Matteo et al., 2008) and (3) mechanical/radiation AGN feedback (MrAGN) (Choi et al., 2012, 2013). We study the effects of AGN feedback on the black-hole scaling relation ($M_{\rm BH} - \sigma_*$ and $M_{\rm BH}/M_{\rm stel}$), X-ray luminosity, baryonic conversion efficiency, star formation, and size of the elliptical galaxies.

We show that massive, non-relativistic outflows and X-ray heating in mechanical and radiation AGN feedback model are indeed a viable mechanism to regulate the black hole growth. The observed $M_{\rm BH} - \sigma$ relationship between the black hole mass and the galaxy velocity dispersion are successfully recovered with MrAGN model. This was also obtained in the previous ThAGN feedback treatments (e.g. Di Matteo et al., 2005; Springel et al., 2005), and we confirm their results on the observed physical relation between black hole and galactic properties, with our modified SPH code and cosmological simulations. Most importantly, however, the MrAGN model shows much lower X-ray luminosity compared to the commonly adopted ThAGN model where all

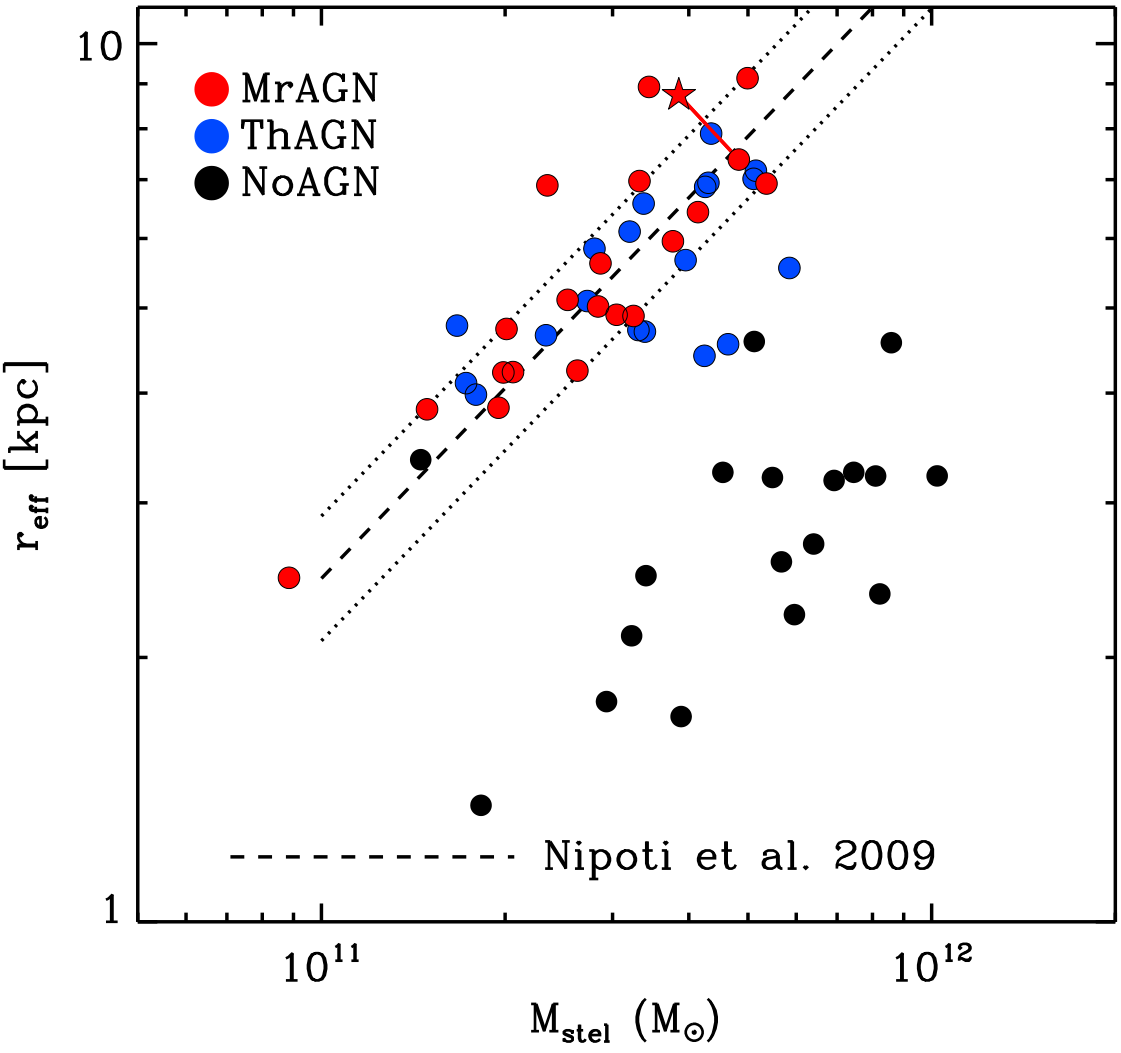



Figure 4.8: Projected stellar half-mass radii of the simulated galaxies versus stellar masses for redshifts z=0 for MrAGN model. The black dashed line indicates the observed size–mass relation for early-type galaxies of Nipoti et al. (2009) with the $1\sigma$ scatter indicated by the dotted lines.

the feedback energy is distributed as thermal heating. While the thermal feedback model produces ∼2-3 orders of magnitude higher thermal X-ray luminosity than expected for given stellar mass of the galaxy, the MrAGN model can successfully reproduce both the observed $L_X - \sigma_*$ and $M_{\rm BH} - \sigma_*$ relations.

We show that mechanical and radiation feedback can effectively suppress in-situ star formation in high mass galaxies as the gas is effectively expelled by AGN-driven outflows. The MrAGN model produces massive red and dead galaxies, reducing final stellar mass by a factor of two compared to the previous works without AGN feedback (Oser et al., 2010, 2012). Therefore, our simulated galaxies with AGN feedback show lower baryonic conversion efficiency than the ones without AGN feedback, but our samples are still overly efficient in transforming gas into stars. The baryonic conversion efficiency at $z = 0$ in our simulated galaxies with MrAGN feedback is still overestimated by roughly a factor of $\sim 1.5$ compared to recent predictions (Guo et al., 2010; Moster et al., 2013). One or more missing further mechanisms is needed (e.g., supernova wind feedback) to suppress star formation in low-mass systems (Hirschmann et al., 2013).

# Bibliography

Aller, M. C. & Richstone, D. O. 2007, ApJ, 665, 120

Behroozi, P. S., Conroy, C., & Wechsler, R. H. 2010, ApJ, 717, 379

Bondi, H. 1952, MNRAS, 112, 195

Bondi, H. & Hoyle, F. 1944, MNRAS, 104, 273

Booth, C. M. & Schaye, J. 2011, MNRAS, 413, 1158

Boroson, B., Kim, D.-W., & Fabbiano, G. 2011, ApJ, 729, 12

Bower, R. G., Benson, A. J., Malbon, R., Helly, J. C., Frenk, C. S., Baugh, C. M., Cole, S., & Lacey, C. G. 2006, MNRAS, 370, 645

Burkert, A. & Tremaine, S. 2010, ApJ, 720, 516

Choi, E., Naab, T., Ostriker, J. P., Johansson, P. H., & Moster, B. P. 2013, ArXiv e-prints

Choi, E., Ostriker, J. P., Naab, T., & Johansson, P. H. 2012, ApJ, 754, 125

Ciotti, L., Ostriker, J. P., & Proga, D. 2010, ApJ, 717, 708

Crenshaw, D. M., Kraemer, S. B., & George, I. M. 2003, ARA&A, 41, 117

Croton, D. J., et al. 2006, MNRAS, 365, 11

Cullen, L. & Dehnen, W. 2010, MNRAS, 408, 669

De Lucia, G. & Blaizot, J. 2007, MNRAS, 375, 2

Debuhr, J., Quataert, E., & Ma, C.-P. 2011, MNRAS, 412, 1341

—. 2012, MNRAS, 420, 2221

Debuhr, J., Quataert, E., Ma, C.-P., & Hopkins, P. 2010, MNRAS, 406, L55

DeGraf, C., Di Matteo, T., Khandai, N., Croft, R., Lopez, J., & Springel, V. 2012, MNRAS, 424, 1892

Dehnen, W. 2001, MNRAS, 324, 273

Di Matteo, T., Colberg, J., Springel, V., Hernquist, L., & Sijacki, D. 2008, ApJ, 676, 33

Di Matteo, T., Khandai, N., DeGraf, C., Feng, Y., Croft, R. A. C., Lopez, J., & Springel, V. 2012, ApJ, 745, L29

Di Matteo, T., Springel, V., & Hernquist, L. 2005, Nat, 433, 604

Dubois, Y., Gavazzi, R., Peirani, S., & Silk, J. 2013, MNRAS, 433, 3297

Dunn, J. P., Bautista, M., Arav, N., Moe, M., Korista, K., Costantini, E., Benn, C., Ellison, S., & Edmonds, D. 2010, ApJ, 709, 611

Fabian, A. C. 2012, ARA&A, 50, 455

Ferrarese, L. & Merritt, D. 2000, ApJ, 539, L9

Franx, M., van Dokkum, P. G., Schreiber, N. M. F., Wuyts, S., Labbé, I., & Toft, S. 2008, ApJ, 688, 770

Gebhardt, K., et al. 2000, ApJ, 539, L13

Guo, Q., White, S., Boylan-Kolchin, M., De Lucia, G., Kauffmann, G., Lemson, G., Li, C., Springel, V., & Weinmann, S. 2011, MNRAS, 413, 101

Guo, Q., White, S., Li, C., & Boylan-Kolchin, M. 2010, MNRAS, 404, 1111

Haardt, F. & Madau, P. 1996, ApJ, 461, 20

Hirschmann, M., et al. 2013, ArXiv e-prints

Hirschmann, M., Somerville, R. S., Naab, T., & Burkert, A. 2012, MNRAS, 426, 237

Hopkins, P. F. 2013, MNRAS, 428, 2840

Hopkins, P. F., Hernquist, L., Cox, T. J., Robertson, B., Di Matteo, T., & Springel, V. 2006, ApJ, 639, 700

Hoyle, F. & Lyttleton, R. A. 1939, Proceedings of the Cambridge Philosophical Society, 34, 405

Johansson, P. H., Naab, T., & Ostriker, J. P. 2009, ApJ, 697, L38

Katz, N. & White, S. D. M. 1993, ApJ, 412, 455

Kauffmann, G., et al. 2003, MNRAS, 341, 33

Khandai, N., Feng, Y., DeGraf, C., Di Matteo, T., & Croft, R. A. C. 2012, MNRAS, 423, 2397

Kormendy, J. & Ho, L. C. 2013, ARA&A, 51, 511

Kormendy, J. & Richstone, D. 1995, ARA&A, 33, 581

Magorrian, J., et al. 1998, AJ, 115, 2285

Marconi, A. & Hunt, L. K. 2003, ApJ, 589, L21

Martizzi, D., Teyssier, R., Moore, B., & Wentz, T. 2012, MNRAS, 422, 3081

McConnell, N. J. & Ma, C.-P. 2013, ApJ, 764, 184

McKee, C. F. & Ostriker, J. P. 1977, ApJ, 218, 148

Moe, M., Arav, N., Bautista, M. A., & Korista, K. T. 2009, ApJ, 706, 525

Moster, B. P., Naab, T., & White, S. D. M. 2013, MNRAS, 428, 3121

Moster, B. P., Somerville, R. S., Maulbetsch, C., van den Bosch, F. C., Macciò, A. V., Naab, T., & Oser, L. 2010, ApJ, 710, 903

Naab, T., Johansson, P. H., & Ostriker, J. P. 2009, ApJ, 699, L178

Naab, T., Johansson, P. H., Ostriker, J. P., & Efstathiou, G. 2007, ApJ, 658, 710

Nipoti, C., Treu, T., Auger, M. W., & Bolton, A. S. 2009, ApJ, 706, L86

Novak, G. S., Ostriker, J. P., & Ciotti, L. 2011, ApJ, 737, 26

Oser, L., Naab, T., Ostriker, J. P., & Johansson, P. H. 2012, ApJ, 744, 63

Oser, L., Ostriker, J. P., Naab, T., Johansson, P. H., & Burkert, A. 2010, ApJ, 725, 2312

Ostriker, J. P., Choi, E., Ciotti, L., Novak, G. S., & Proga, D. 2010, ApJ, 722, 642

Planck Collaboration, Ade, et al. 2013, ArXiv e-prints

Proga, D. & Kallman, T. R. 2004, ApJ, 616, 688

Puchwein, E. & Springel, V. 2013, MNRAS, 428, 2966

Read, J. I. & Hayfield, T. 2012, MNRAS, 422, 3037

Rigby, E. E., Best, P. N., Brookes, M. H., Peacock, J. A., Dunlop, J. S., Röttgering, H. J. A., Wall, J. V., & Ker, L. 2011, MNRAS, 416, 1900

Ritchie, B. W. & Thomas, P. A. 2001, MNRAS, 323, 743

Saitoh, T. R. & Makino, J. 2013, ApJ, 768, 44

Sazonov, S. Y., Ostriker, J. P., Ciotti, L., & Sunyaev, R. A. 2005, MNRAS, 358, 168

Sijacki, D., Springel, V., Di Matteo, T., & Hernquist, L. 2007, MNRAS, 380, 877

Sijacki, D., Springel, V., & Haehnelt, M. G. 2009, MNRAS, 400, 100

Silk, J. & Rees, M. J. 1998, A&A, 331, L1

Somerville, R. S., Hopkins, P. F., Cox, T. J., Robertson, B. E., & Hernquist, L. 2008, MNRAS, 391, 481

Spergel, D. N., et al. 2007, ApJS, 170, 377

Spergel, D. N., et al. 2003, ApJS, 148, 175

Springel, V. 2005, MNRAS, 364, 1105

Springel, V., Di Matteo, T., & Hernquist, L. 2005, MNRAS, 361, 776

Springel, V. & Hernquist, L. 2003, MNRAS, 339, 289

Teyssier, R., Moore, B., Martizzi, D., Dubois, Y., & Mayer, L. 2011, MNRAS, 414, 195

Tremaine, S., et al. 2002, ApJ, 574, 740

Ueda, Y., Akiyama, M., Ohta, K., & Miyaji, T. 2003, ApJ, 598, 886

Vogelsberger, M., Genel, S., Sijacki, D., Torrey, P., Springel, V., & Hernquist, L. 2013, ArXiv e-prints